Imaging of magnetization dynamics in temperature gradients

Dissertation

zur Erlangung des Doktorgrades
der Naturwissenschaften (Dr. rer. nat.)
der Fakultät für Physik
der Universität Regensburg

vorgelegt von

Michael Vogel

aus Kaiserslautern

im Jahr 2018

Promotionsgesuch eingereicht am: 1. Februar 2017
Die Arbeit wurde angeleitet von: Prof. Dr. Christian H. Back

Contents

Acknowledgements

First of all I am grateful to my supervisor Prof. Dr. Christian H. Back for the support during the experimental and theoretical challenges in the making of this thesis and the opportunity to carry out my PhD degree in his group. I have greatly benefitted from the collaboration with him and all the members of his group and from his inputs and encouragements. I extend my gratitude to Prof. Dr. Josef Zweck for enabling the TEM measurements carried out during the making of the thesis and for sharing his knowledge on microscopy and optics.

My sincere thanks also goes to the members of the dissertation committee, Prof. Dr. G. Bali, Prof. Dr. J. Repp and Prof. Dr. D. Bougeard for their time and patience.

In my work on the theoretical modelling of the experiments presented here I have received a lot of input from Prof. Dr. Claudia Mewes and Prof. Dr. Tim Mewes, especially on the micromagnetic simulations, using the micromagnetics code M^3 developed by them. Further their input on developing the analytic framework using an Extended Thiele equation model was of invaluable importance.

Special thanks goes to Dr. Hermann Stoll, Dr. Markus Weigand and Michael Bechtel from the MPI Stuttgart for technical support during the measurements at BESSY II around the clock.

I would like to offer my special thanks to Prof. Dr. Stuart Parkin for allowing me to visit his labs at IBM Almanden.

I am grateful to Prof. Dr. Guenther Reiss and Prof. Dr. Andy Thomas for providing sputtered thin films.

I am especially thankful to Prof. Dr. Dieter Weiss and his entire group for providing infrastructure in the clean-room for sample preparation and characterization.

I thank Dr. Jean-Yves Chauleau, Dr. Matthias Kronseder and Dr. Lin Chen for fruitful discussions and the collaboration on different projects not presented here.

Further my thank goes to my colleagues from my department that contributed in the making of this thesis. Here I want to emphasize the help of Johannes Wild and Felix Schwarzhuber who spent a lot of measurement time with me at the TEM.

I have also had support from Bernhard Zimmermann who helped charaterizing temperature gradients in small nanostructures in the making of his bachelor thesis. I also enjoyed working with him on FMR measurements on coupled magnetic bilayer system in out of plane temperature gradients (not shown here) and spending time with him at BESSY. I thank Ajay Gangwar for valuable insights on preparing samples on SiN-membranes.

I also want to thank my coauthors and callaborators on different projects not shown in this thesis. Martin Decker (spin orbit induced switching), Johannes Stigloher (TR-MOKE measurements on the manipulation of spin waves by an applied temperature gradient), Maximilian Schmid (Transverse Spin Seebeck Effect measurements that turned out to be Planar Nernst Effect measurements) and Sasmita Srichandan (Electrical and thermal transport coefficients of CoFe thin films). Many thanks go to the Master students I had the opportunity to work with, namely Michael Mueller and Susanne Brunner. Apart from those already mentioned I want to thank all the other members from the department who let me enjoy my time in Regensburg, especially Robert Islinger and Tobias Weindler.

I can not thank enough our secretaries Magdalena Pfleger, Doris Meier, Sylvia Hrdina, Claudia Zange and our technician Markus Hollnberger.

Last but not least, I thank my niece Marie for mental support. My deepest gratitude goes to my wife Alexandra for all the support during my time as a PhD student in Regensburg and proof-reading this thesis with her special powers. I am forever thankful to my mother Maria for granting me such freedom to choose my path and always encouraging me.

Part of this work was supported by the DFG SPP 1548.

1 Overview

Neuromorphic computing describes the use of very-large scale integrated logic (VLSI) systems to mimic neurobiological architectures [1] promising advances in computation density and energy efficiency [2] in the post Moore's law age of computing [2, 3]. In nature neurons behave as nonlinear oscillators developing rhythmic activity and interact to process information [4]. Hence, oscillatory neural networks (ONNs) are promising building blocks for VLSIs, harnessing either the frequency or phase as state variable for logic operations [5–7]. Recently, a novel approach using nanoscale spintronic-oscillators in the form of magnetic tunnel junctions [8, 9] has been experimentally demonstrated to realize such VLSIs [10]. Two key requirements for oscillators used in VLSIs are high stability to process information reliable and the possibility to stack the oscillators in high density arrays. In order to stack the total number of neurons in the human brain $\approx 10^{11}$[11] in an ONN on a 10 cm by 10 cm chip, the size of the single elements have to be of the order of 100 nm. A possible spintronic building block for such networks are magnetic vortex oscillators as investigated in this thesis. The magnetic vortex structure [12, 13] is characterized by an in plane curling magnetization, the sense of rotation defining the chirality $c = \pm 1$, and a perpendicular magnetized core at the center who's direction defines the polarity $p = \pm 1$. For disk shaped magnetic elements this magnetization structure causes flux closure of the in plane magnetization with the out of plane core with a size of 10 nm to 30 nm generating a small stray field [14]. The flux closure configuration causes a highly stable ground state configuration and allows for closed stacked arrays due to almost no interaction. Their lateral size is scalable from nm size to a few µm and is accompanied by dynamics from the kHz to the GHz regime [15]. In the low frequency excitation

state, called the gyration mode [12, 14], surface magnetic charges appear, which allow dynamic dipolar interaction in a pair of vortices next to each other [16, 17].

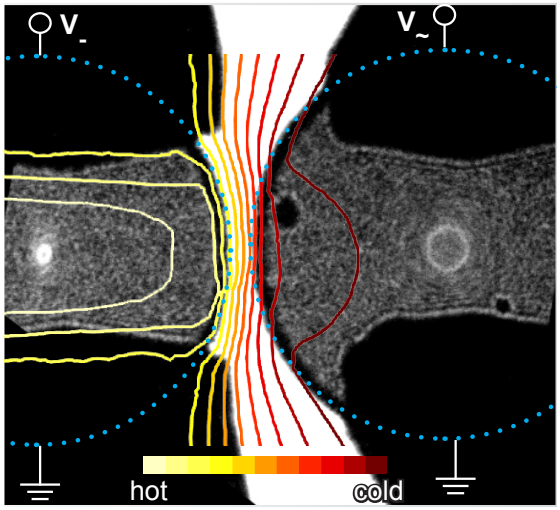

Figure 1.1: Sketch of Experiment 1: In a pair of stray field coupled magnetic vortex oscillators the disk on the right is excited by an ac charge current via STT, the disk on the left is heated to control the resonance frequency via a change of the saturation magnetization. This allows the control of the phase relation between the two excitations (white ellipses).

In the first experiment presented in this thesis a pair of stray field coupled magnetic vortex oscillators (see fig. 1.1) is investigated by Lorentz Transmission Electron Microscopy (L-TEM) and Scanning Transmission X-ray Microscopy (STXM). One of the oscillators is excited by an ac current via the Spin Transfer Torque (STT) effect. The second oscillator is heated via Joule heating, thereby reducing the saturation magnetization and causing a shift of the relative phase relation of the two oscillators to arbitrary values between the in phase and out of phase state (fine-grain phase control). Phase manipulation in a controlled manner is critical in ONNs and promises a wide range of applications from mimicking rhythmic motive patterns in robotics [18, 19] to neuromorphic image recognition [20].

The second experiment investigates the manipulation of the vortex core position by pure thermomagnonic torques. Traditionally the manipulation of topological solitons such as magnetic vortices and skyrmions is achieved by spin polarized electric charge currents due to the application of an electrical potential [21]. As recently proposed by theory, thermally excited magnons created by temperature gradients can also be used to manipulate magnetic structures [22, 23]. Here the theoretically well understood dynamics of magnetic vortex cores, when subject to thermal gradients, is investigated. Transmission Electron Microscopy measurements on magnetic vortices in temperature gradients created by local static Joule

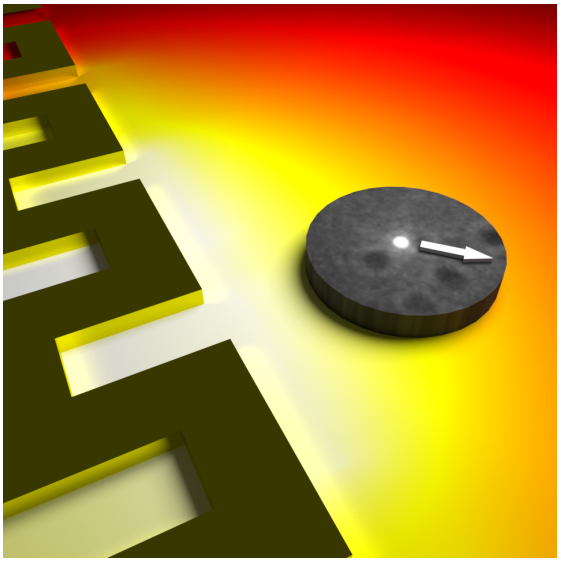

Figure 1.2: Sketch of Experiment 2: A magnetic vortex core inside a Py disk is placed next to a meander type heater. The temperature of the heater is increased by Joule heating. The Py disk sits on the edge of a SiN-membrane. The frame of the membrane doubles as heatsink. The movement of the core is investigated by L-TEM measurements.

heating (see fig. 1.2) were performed. A large deflection compared to electric spin transfer torque excitation of the magnetic vortex core is observed. It is shown that the magnitude of the deflection depends on the applied heating power and the polarization of the core. To analyze the experimental results, a generalized Thiele equation [24] model, including the different forces acting on the vortex core due to the applied temperature gradient, was developed. This analysis allows the estimation of the magnitude of the core motion for the involved force terms and therefore the differentiation of the origin of the experimental observed vortex movement.

Part I

Theoretical and Experimental Background

2
Theoretical Background

2.1 Magnetic Vortex Core

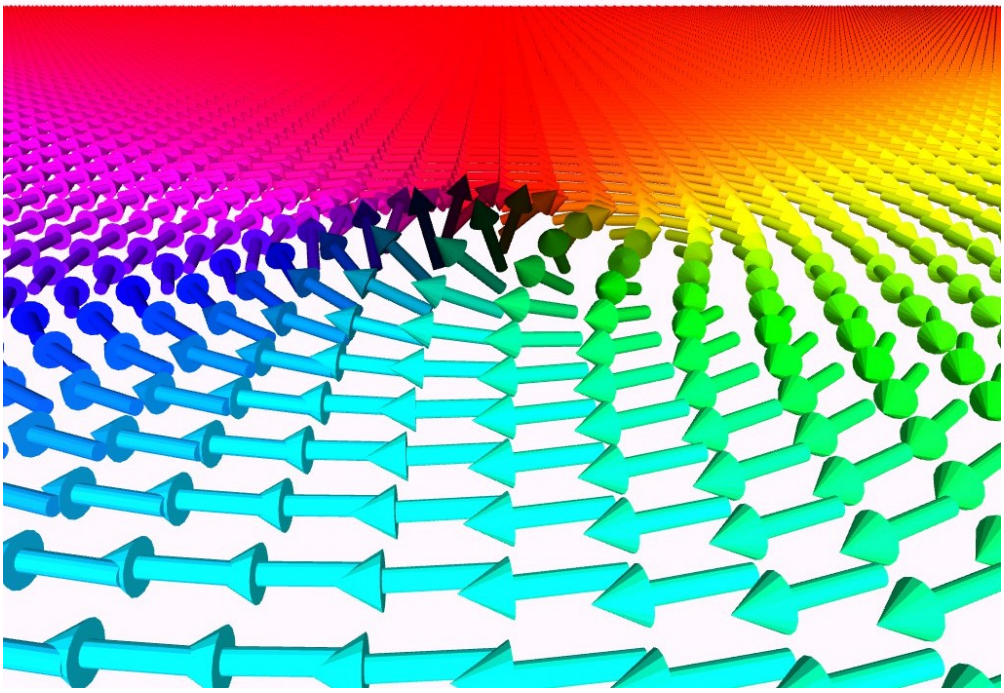

Figure 2.1: Micromagnetic simulation of relaxed magnetic vortex core. Color indicating the direction of the curling in plane magnetization. The out of plane core in the center points in upward direction.

Vortices are topological solitons [25] occurring in many classical field theories. They are stable topologically protected quasi-particles with finite mass and smooth structures [25]. In physical dynamic systems vortex like structures exist across a

wide range of length scales from quantized vortices in superconductors [25] at inter atomic length-scales to galactic structures with dimensions of several kpc ($1\,\mathrm{kpc} \approx 3 \times 10^{19}\mathrm{m}$)[26]. Their dynamic is often governed by similar non linear differential equations. The magnetic vortex structure fig. 2.1 is characterized by an in-plane curling magnetization and a perpendicularly magnetized core at the center [12, 13]. The sense of rotation determines the chirality $c = \pm 1$. The direction of the perpendicular core defines the polarity $p = \pm 1$ which is one of a total of two topological charges of a magnetic vortex core, the other one being the vorticity $v = 1$, which all vortex structures have in common.

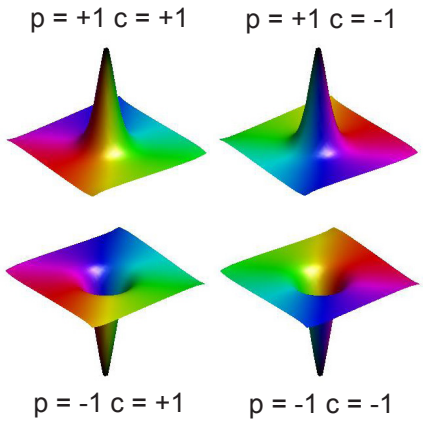

Figure 2.2: Possible combinations of c and p, M_Z: height information M_x,M_y: color coded.

The possible combination of p and c allow for a total of four logical states (see section 2.1) for information processing. The magnetic vortex is one of the elementary magnetic ground states found in lateral confined magnetic thin films [27]. Due to it's topological protection [28] and low stray fields the magnetic vortex state is magnetically very stable. For disk shaped magnetic elements this configuration causes flux closure in the in-plane magnetization, with only the out of plane core with a typical size of 10 nm to 30 nm [29] generating a small stray field. The vortex ground state has a complex spin excitation spectrum, with a low-frequency mode of displacement of the vortex as a whole called the gyration mode [13, 14]. Magnetization dynamics in this case can be well described within the framework of micro-magnetic simulations and an analytic solution based on the Thiele equation (section 2.2). The resonance frequency f_r of the gyration mode scales with the lateral size of the magnetic disk and the thickness (see fig. 2.9) allowing scalable dynamics in the kHz to GHz regime [15]. The vortex gyration can be excited by different means. Traditionally the excitation is done non-locally by low ($\approx$ mT) in plane magnetic field pulses [30]. It is also possible to locally excite the core by application of a spin polarized current [31]. This manipulation of the magnetization dynamics at the nanoscale by the means of electric currents has become one of the most attractive subjects in the field of magnetic vortex core dynamics from both the fundamental and the application viewpoints [31, 32].

In the low frequency excitation state surface magnetic charges appear due to the core displacement [13]. In case of a pair of vortices next to each other (see fig. 2.4), this brings about dynamic dipolar interaction between them [16, 17]

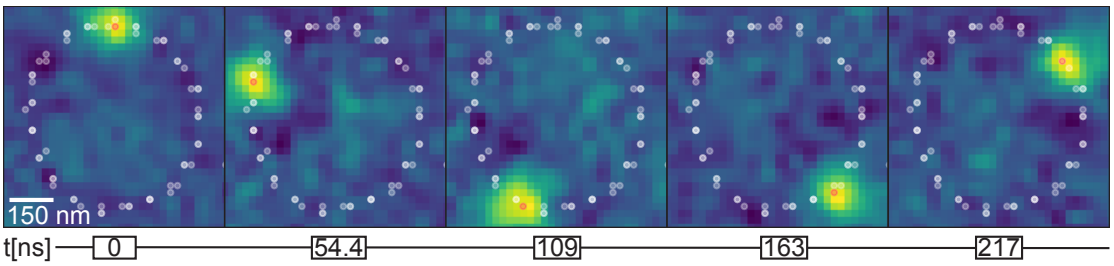

Figure 2.3: Time resolved STXM measurement of a excited vortex core in the gyration mode. The vortex core is excited by short current pulses at a resonance frequency of $f = 240\,\mathrm{MHz}$. The time-resolution of the measurement is 66 ps. The spot is tracked via image recognition and the positions are shown in white. 5 frames at equidistant time-steps are shown here.

(see section 2.4). This opens a manifold of possibilities. Due to their coupling magnetic vortex oscillators can be used as building blocks for oscillatory networks. So far many implementations of this have been proposed. The signal transfer across a chain of such oscillators has been studied [33, 34] oberserving wave modes travelling through such artificial crystals. Basic building blocks for computation and logic manipulation have been realised, such as XOR and OR operators [35] as well as transistors [36]. In chapter 6 a new method to realise fine-grain phase control in such networks is demonstrated.

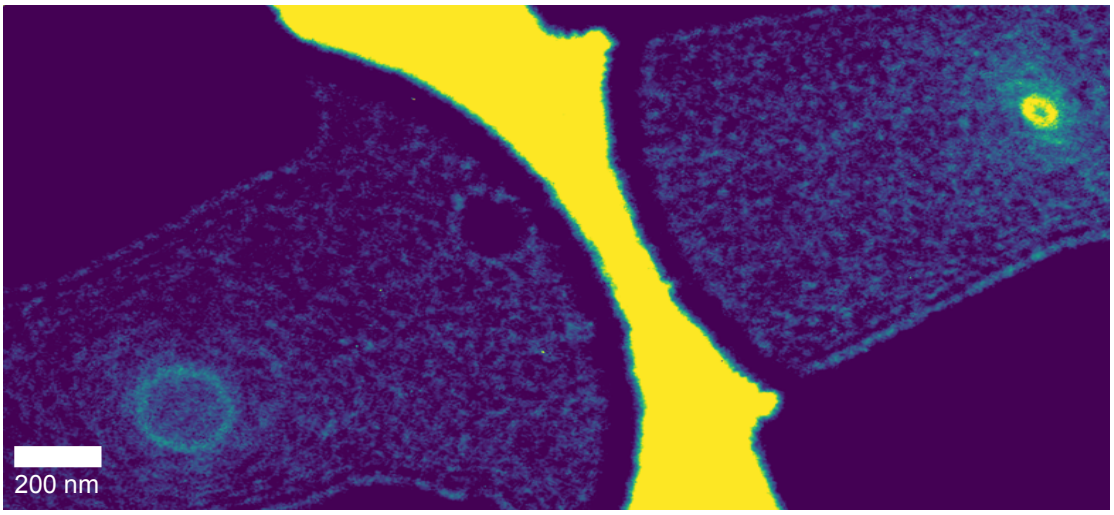

Figure 2.4: L-TEM image of the pair of magnetic vortex oscillators with a radius of $r = 0.9\,\mu\mathrm{m}$. The gyration mode is driven by a cw excitation at 240 MHz applied on the left disk. The gyration mode can be seen at the middle of both disks in form of ellipses.

These oscillatory applications harness resonant excitation of the vortex core easily increasing the static elongation of the vortex core by a factor of 1000. So far the only means to image the elongated vortex core by static excitation have been large external magnetic fields [37] (see fig. 2.5). Even though STT by spin polarized currents is a very effective way to manipulate magnetization dynamics [38] with

many applications from racetrack memory [38] to STT-MRAM predicted to outperform current memory technologies in the near future [38], the required current densities for Py would be magnitudes of order larger than the destruction threshold to experimentally observe a movement of the vortex core (see section 2.3). In this work a new way to manipulate the magnetic vortex core structure by the Magnon Spin Seebeck Effect (see section 2.3 and chapter 7) is presented resulting in movement 5 order of magnitude larger than possible via spin polarized electric currents.

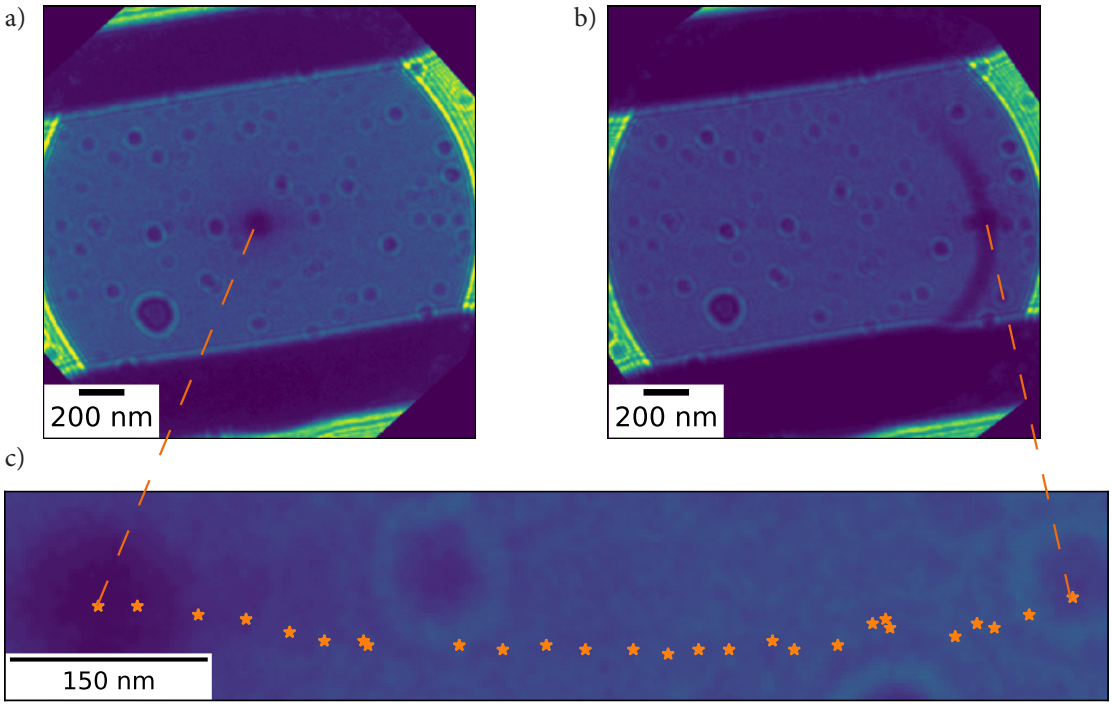

Figure 2.5: L-TEM measurement of 20 nm thick Py disks with a radius of 1 µm a) In a zero in-plane magnetic field the vortex core is at the center of the Py disk. b) After a field sweep up to 30 000 A/m the vortex core is pushed to the edge of the Py disk. c) The path traveled by the vortex core differs from a straight line and indicates the influence of the local energy landscape created by defects in the SiN-membrane (see section 4.1.1).

2.2 Micromagnetic Simulations and Thiele Equation

The magnetization dynamics of the spin core motion driven by a spin polarized current is phenomenological well described by the extended Landau-Lifshitz-Gilbert equation [39]:

$$\begin{aligned}\frac{d\overrightarrow{M}}{dt} =& -\gamma\overrightarrow{M}\times\overrightarrow{H}_{eff}+\frac{\alpha}{M_s}\overrightarrow{M}\times\frac{d\overrightarrow{M}}{dt}\\ &-\frac{1}{M_s^2}\vec{M}\times(\vec{M}\times(b_j\vec{j}\cdot\overrightarrow{\nabla})\vec{M})-\frac{\xi}{M_s}\vec{M}\times(b_j\vec{j}\cdot\overrightarrow{\nabla})\vec{M},\end{aligned} \tag{2.1}$$

with the magnetization vector $\vec{M}$, the gyromagnetic ratio γ, the Gilbert damping parameter α, and the saturation magnetization M_s. The effective magnetic field $\vec{H}_{eff}$ includes all internal and external fields. The constant $b_j = (\wp\mu_B)/[eM_s(1+\xi^2)]$ describes the coupling between the magnetization and the electric current density $\vec{j}$. $\wp$ is the current polarization, μ_B is the Bohr magneton, e is the elementary charge, and ξ is the degree of nonadiabaticity [40]. A spin polarized current density $\wp\vec{j}$ can be created by an electric potential gradient, by a gradient in the chemical potential as well as a temperature gradient. The spin polarized current density can be derived within a three current model [41–43]. Neglecting spin mixing the Onsager relations for the entropy current density $\vec{j}_s$, the electric current densities, $\vec{j}_\uparrow$ and $\vec{j}_\downarrow$, for the spin-up and spin-down charge carriers are given by

$$\begin{pmatrix}\vec{j}_s\\ \vec{j}\\ \vec{j}_p\end{pmatrix} = -\begin{pmatrix}\kappa & q\sigma\varepsilon & q\sigma_p\varepsilon_p\\ \sigma\varepsilon & \sigma & \sigma_p\\ \sigma_p\varepsilon_p & \sigma_p & \sigma\end{pmatrix}\begin{pmatrix}\overrightarrow{\nabla}T\\ \overrightarrow{\nabla}V\\ \overrightarrow{\nabla}(\triangle\mu)/q\end{pmatrix}. \tag{2.2}$$

Here $\overrightarrow{j} = \vec{j}_\uparrow + \vec{j}_\downarrow$ is the electric charge current density, and $\overrightarrow{j}_p = \vec{j}_\uparrow - \vec{j}_\downarrow$ is the spin polarized current density. q is the charge of the charge carrier, and κ is the thermal conductivity. The effective conductivity σ, and the spin-dependent polarization conductivity σ_p are defined by $\sigma = \sigma_\uparrow + \sigma_\downarrow$, and $\sigma_p = \sigma_\uparrow - \sigma_\downarrow$, where $\sigma_\uparrow$ and $\sigma_\downarrow$ are the spin dependent electric conductivities. ε and ε_p are the effective and polarization spin Seebeck coefficients. The electrochemical potentials for the charge carriers, $\mu_\uparrow$ and $\mu_\downarrow$, have been expressed with the mean chemical potential μ_0 via $\mu_{\uparrow(\downarrow)} = \mu_0 \pm \triangle\mu + qV$ [44]. V and T are the potential and the temperature respectively. Using the conventional definition of the current polarization $\wp_c = \frac{\sigma_\uparrow-\sigma_\downarrow}{\sigma_\uparrow+\sigma_\downarrow}$ and the spin polarization of the Seebeck coefficient $\wp_s = \frac{\varepsilon_\uparrow-\varepsilon_\downarrow}{\varepsilon_\uparrow+\varepsilon_\downarrow}$, where $\varepsilon_\uparrow$ and $\varepsilon_\downarrow$ are the spin depend Seebeck coefficients, the spin polarized current density, entering the Landau Lifshitz Gibert (eq. (2.1)) equation is given by

$$\vec{j}_p = -\wp\sigma\varepsilon\vec{\nabla}T \tag{2.3}$$

with the polarization coefficient given by

$$\wp = \wp_c + \frac{\wp_s(1-\wp_c^2)}{1+\wp_s\wp_c}, \tag{2.4}$$

which can be rewritten, using a power expansion of the denominator, as [45, 46]

$$\wp \approx \wp_c + \wp_s(1-\wp_c^2). \tag{2.5}$$

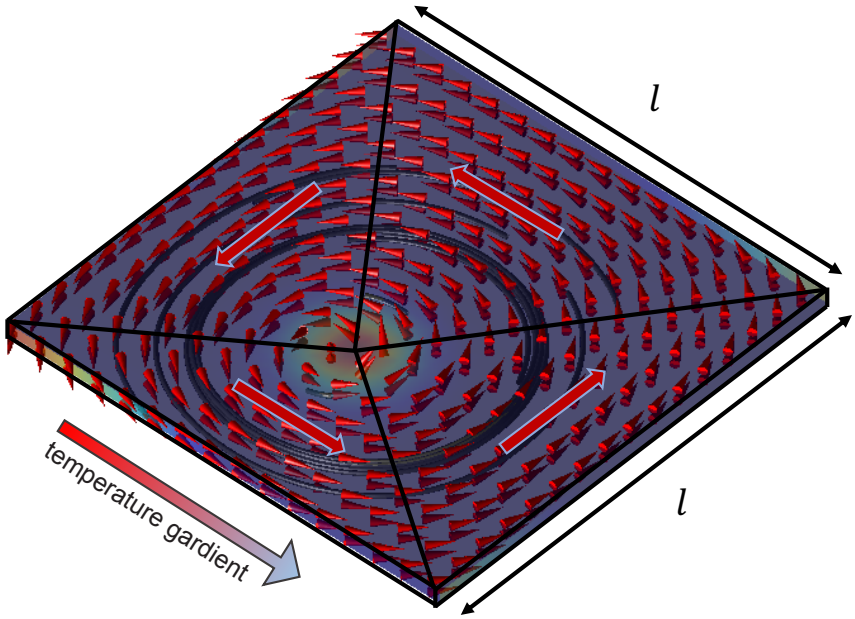

Figure 2.6: Sample geometry used in fully micromagnetic simulations. The black lines and the overlaid red arrows indicate the scheme of the magnetization used in the analytic model.

In the following we will consider a thin square film of permalloy with lateral dimension l and film thickness t [47]. The sample geometry is shown in fig. 2.6. The saturation magnetization is given by $M_s = 8 \times 10^5$ A/m and the exchange constant is set to $A = 13 \times 10^{-12}$ J/m [48], which corresponds to an exchange length of $l_{ex} = 5.7$ nm. For the micromagnetic simulations we have used the finite element code M^3 [49] with a spatial resolution of 2.5 nm $\times$2.5 nm $\times$5 nm to avoid discretization errors and allow for large scale simulations for lateral dimensions of up to 0.5 µm. The spin polarized electric current density entering the Landau-Lifshitz-Gilbert equation is calculated using equations (eq. (2.3)) and (eq. (2.4)). Using experimental measured values for the involved material constants [50], the polarization coefficient $\wp_Q$ given by equation (eq. (2.4)) is 46%, and the effective spin Seebeck coefficient is $-18\,\mu$V/K. To study the behavior of the vortex motion, different temperature gradients, different sample dimensions, and different Gilbert damping parameters are considered. In each micromagnetic simulation a vortex

pattern is initialized by $\vec{M}(\vec{r}) = M_s(l-y, x-l, a)^T/|(l-y, x-l, a)^T|$, where a is of the order of the magnitude of the vortex core radius [51]. In the absence of a spin polarized current density the structure is relaxed into its equilibrium position in the middle of the square sample. The effective field in the Landau-Lifshitz-Gilbert equation is determined by the exchange and demagnetization field of the permalloy sample. After this initialisation step a constant or time dependent temperature gradient is applied along the x direction, which leads to a constant or time dependent spin polarized current density along the x axis. Figure 2.7(a) shows the initial relaxed vortex state right before a constant temperature gradient of 1.24×10^4 mK/nm, which corresponds to a spin polarized current density of 5×10^{11} A/m^2, is applied.

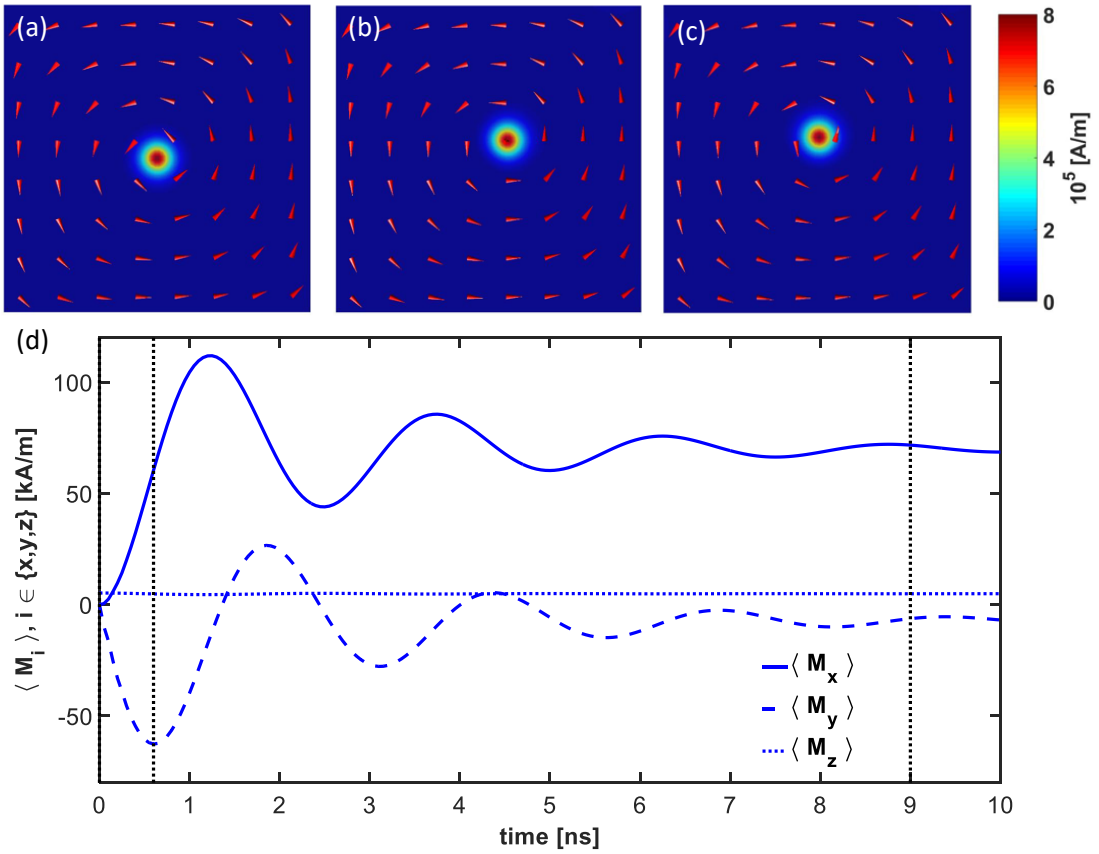

Figure 2.7: (a) to (c) show the vortex structure for a 200 nm × 200 nm × 10 nm permalloy sample at times 0 ns, 0.6 ns, and 9 ns with a constant current density of 5×10^{11} A/m^2 is applied in x direction. The Gilbert damping parameter is set to $\alpha = 0.1$. The color coding corresponds to the magnitude of the out of plane component of the magnetization. The red arrows show the direction of the magnetization as a guide for the eye. (d) The average magnetization components are shown as a function of time. The solid line shows $\langle M_x \rangle$, the dashed line shows $\langle M_y \rangle$, and the dotted line $\langle M_x \rangle$.

When a constant spin polarized current density is applied, the vortex structure performs a spiral movement until it reaches its new equilibrium position. Figure 2.7 (b) and (c) show snapshots of the vortex structure for the times 0.6 ns and

9 ns. The color coding indicates the magnitude of the out of plane magnetization component. Figure 2.7(d) shows the averaged magnetization components $\langle M_x \rangle$ (solid line), $\langle M_y \rangle$ (dashed line), and $\langle M_z \rangle$ (dotted line) as a function of time. The times corresponding to the snapshots are indicated as vertical black dotted lines. For a large Gilbert damping constant of 0.1 it can be seen easily that the vortex structure has almost reached its new equilibrium position after 10 ns.

To further analyze our numerical results of the gyrotropic motion of temperature driven vortices in small thin film elements we use an analytic solution of the Thiele equation [24], which has been expanded by Thiaville et al. [52] to include a spin polarized current density. By describing the vortex by four triangles, as shown in fig. 2.6, it is possible to establish a direct correspondence between the vortex-core position and the spatially averaged magnetization [51]. In this model it is assumed that the magnetization in each triangle is homogeneous, as indicated by the red arrows in fig. 2.6. Following the derivations of Krüger at al. [51] and neglecting any Oersted field driven magnetization dynamics by assuming a spatially homogeneous current in x direction, the two dimensional equation of motion for the vortex core position described by the vector $(x(t), y(t))^T$ is given by

$$\frac{d}{dt}\begin{pmatrix} x \\ y \end{pmatrix} = \begin{pmatrix} -\Gamma & -p\omega \\ p\omega & -\Gamma \end{pmatrix}\begin{pmatrix} x \\ y \end{pmatrix} + \begin{pmatrix} -(1+\frac{\Gamma^2}{\omega^2+\Gamma^2}\frac{\xi-\alpha}{\alpha}) \\ \frac{p\omega\Gamma}{\omega^2+\Gamma^2}\frac{\xi-\alpha}{\alpha} \end{pmatrix} b_j j. \tag{2.6}$$

Here $p = \pm 1$ is the polarization of the vortex core and refers to the magnetization direction of the vortex core, either parallel or antiparallel to the z axis. In the absence of external currents the excited vortex undergoes an exponentially damped spiral rotation until it reaches its equilibrium position. ω is the eigenfrequency of the free vortex motion and Γ is the corresponding damping constant. Assuming a small displacement of the vortex center from equilibrium, the energy of the vortex shifted from its equilibrium position at the dot center can be modeled as a parabolic potential $E = \tilde{\kappa}(x^2 + y^2)$, with stiffness coefficient $\tilde{\kappa}$ [13], which for a circular disk can be approximated by $\tilde{\kappa} = mu_0 M_s^2[F_1(g) - l_{ex}/l)^2]$ with $g = t/l$ and the exchange length l_{ex} [53]. $F_1(g)$ is given by $F_1(g) = \int_0^\infty f(kg)J_1^2(k)/kdk$ with $f(x) = 1 - (1 - e^{-x})/x$ and $J_1(x)$ the Bessel function of first order. Within this approximation ω and Γ can be expressed as

$$\omega = -\frac{pG_0\tilde{\kappa}}{G_0^2 + D_0^2\alpha^2} \text{ and } \Gamma = -\frac{D_0\alpha\tilde{\kappa}}{G_0^2 + D_0^2\alpha^2}. \tag{2.7}$$

The gyrovector $\vec{G} = G_0\hat{e}_z$ indicates the axis of precession and is perpendicular to the film plane. It can be represented with the components of the antisymmetric gyrotensor and is given by $G_0 = 2\pi ptM_s/\Gamma$ [13]. D_0 is the non-zero diagonal element ($D_0 = D_{xx} = D_{yy}, D_{zz} = 0$) of the dissipation tensor and can be estimated

by $D_0 \approx -\pi M_s \mu_0 \ln(l/a)/\gamma$. Assuming that the damping constant of the vortex motion is small compared to its frequency, i.e. $\Gamma^2 \ll \omega^2$, one can solve this equation [51] and in case of a constant spin polarized electric current density the final core deflection is given by [47]:

$$\begin{pmatrix} \Delta x_{end} \\ \Delta y_{end} \end{pmatrix} = - \begin{pmatrix} \frac{\Gamma \xi}{\alpha(\Gamma^2+\omega^2)} \\ \frac{\omega}{(\Gamma^2+\omega^2)} \end{pmatrix} b_j j. \tag{2.8}$$

It is important to note that Γ and ω are itself functions of the Gilbert damping constant α, see equation (eq. (2.7)). However, assuming that the Gilbert damping constant is small, one can use a Taylor series expansion to show that ω, Δx_{end}, and Δy_{end} only depend on α in second and higher orders. Whereas Γ in leading order is proportional to α. This will become important for the later discussion of the periodically driven vortex motion.

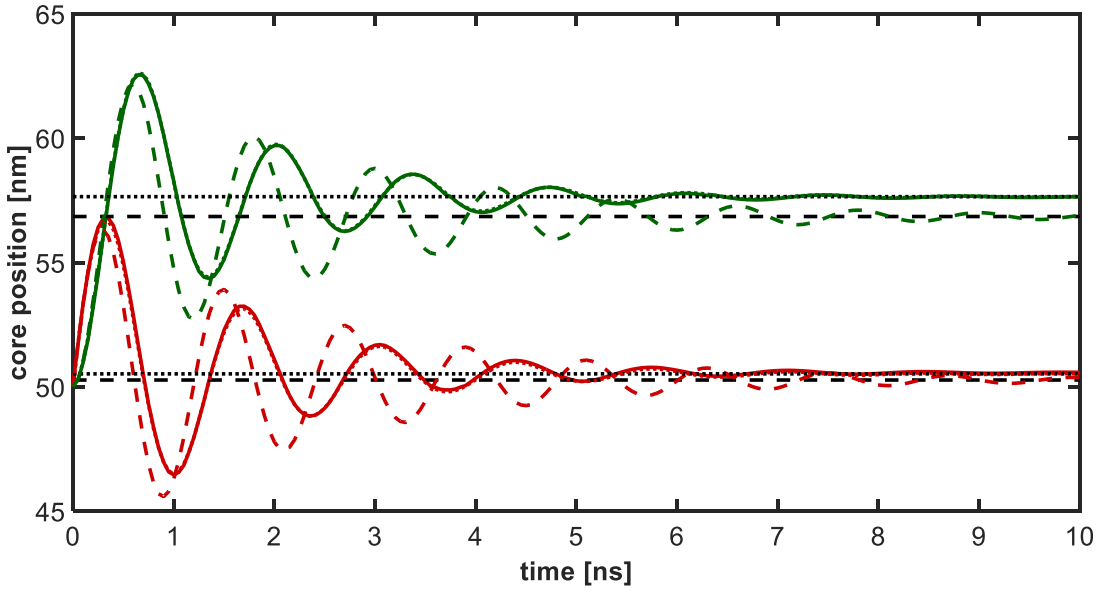

Figure 2.8: Vortex core position (red: x coordinate, green: y coordinate) as a function of time for a 100 nm × 100 nm Py sample of thickness 10 nm. The Gilbert damping constant has been set to $\alpha = 0.1$ and a linear temperature gradient of 1.24×10^4 mK/nm has been assumed. The solid lines are the core positions determined from the fully micromagnetic simulation, the dashed green and red lines are obtained within the analytic model, and the dotted red and green lines are obtained by fitting to the micromagnetic simulations. The black dashed and dotted lines correspond to the final stationary core position using an analytic model using the analytic calculated eigenfrequency of the vortex core motion and the eigenfrequency derived from the fitted solution.

Figure 2.8 shows the vortex core position as a function of time for a 100 nm × 100 nm permalloy sample of thickness 10 nm (red: $x(t)$, and green: $y(t)$). The solid line has been determined from the numerical simulations by calculating the core position. The dashed black lines are the final core positions determined within

the analytic model (see equation (2.8)). The red and green dotted lines have been obtained by a fitting algorithm of the numerical data to the analytical model with ω and Γ as free fitting variables. As starting values for the complex fitting procedure estimates from a Fast Fourier Analysis of the data have been chosen. The fitted analytic model is in good agreement with the numerical simulations. To test the scaling behavior full micromagnetic simulations have been performed for lateral dimensions of $l \in \{100, 200, 300, 400, 500\}$ nm and two different linear temperature gradients of 1.24×10^3 mK/nm and 1.24×10^4 mK/nm corresponding to a spin polarized current density of 5×10^{10} A/m^2 and 5×10^{11} A/m^2.

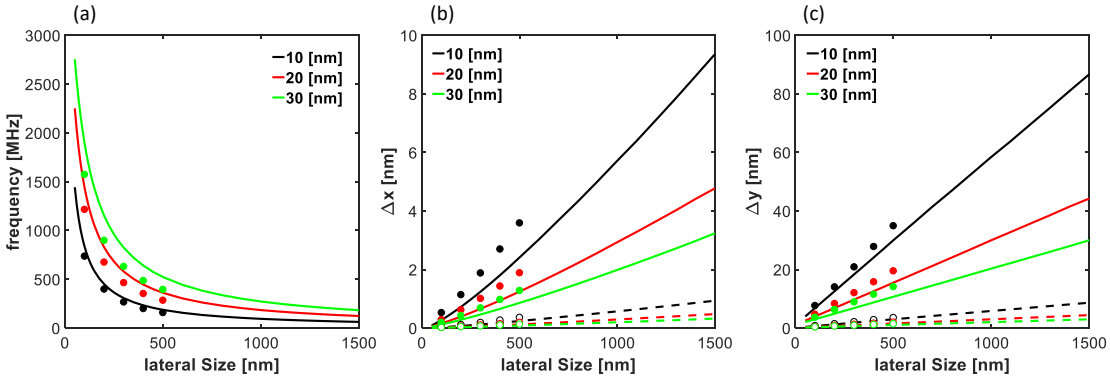

Figure 2.9: (a) Eigenfrequency $f = \omega/(2\pi)$ of the system for different lateral dimensions and thicknesses (10 nm, 20 nm, and 30 nm). (b) Final core position Δx_{end} and (c) final core position Δy_{end} for different lateral dimensions and thicknesses. The lines are calculated within the analytic model (solid lines for a temperature gradient of 1.24×10^4 mK/nm and dashed lines for a temperature gradient of 1.24×10^3 mK/nm and the dots are determined from the fully micromagnetic simulations.

Figure 2.9(a) shows the eigenfrequency of the system as a function of the lateral dimension of the square. The lines are calculated within the analytic model (see equation (2.7)) and the dots show the values determined from the numerical simulations. Although the analytical model overestimates the frequency, it is in good agreement with the numerical findings, especially for larger sample sizes, the agreement between analytical and numerical results becomes very small, which is especially important when estimating values for larger sized samples which would be computational time consuming. The different colors indicate different sample thicknesses. The subfigures fig. 2.9 (b) and (c) show the final vortex core position as a function of the lateral dimension and sample thickness. In addition two sets of data are shown corresponding to two different spin polarized current densities (solid and dotted lines). As expected the magnitude of the final core position scales with the applied spin polarized current density (see equation (2.8)). Due to the symmetry of the system, i.e. spin polarized current along the x direction, the core deflection is much smaller along the x direction than along the y direction,

since this direction is proportional to the non-adiabacity parameter ξ, which is typically relatively small. Another interesting observation is that the analytical model seems to underestimate the final core position. Overall it becomes apparent that the largest movement for the vortex core can be achieved for thin but large samples. This becomes especially important for an experiment using thermal spin transfer torque. So far we have used relatively large temperature gradients, which might be difficult to achieve and maintain in an experimental set up. To overcome this experimental challenge, in the following the vortex motion driven by periodic heat pulses will be considered with the goal to achieve maximal lateral movement and to minimize the involved temperature gradients. For the case that the vortex motion is driven by a series of heat pulses we decouple the equation of motion for the core position and obtain the following second order differential equations:

$$\begin{aligned} &\frac{d^2}{dt^2}\begin{pmatrix} x \\ y \end{pmatrix} + 2\Gamma \frac{d}{dt}\begin{pmatrix} x \\ y \end{pmatrix} + (\omega^2 + \Gamma^2)\begin{pmatrix} x \\ y \end{pmatrix} \\ &\qquad = \begin{pmatrix} -p\omega b_j j + \frac{p\omega\Gamma}{\omega^2+\Gamma^2}\frac{\xi-\alpha}{\alpha} b_j \frac{dj}{dt} \\ -\Gamma(1+\frac{\xi-\alpha}{\alpha})b_j j - (1+\frac{\Gamma^2}{\omega^2+\Gamma^2}\frac{\xi-\alpha}{\alpha})b_j \frac{dj}{dt} \end{pmatrix}. \end{aligned} \tag{2.9}$$

Here the current density is time dependent. Each equation has the form of the differential equation for a damped harmonic oscillator, where the friction is given by 2Γ. In the following we assume that the current varies like $j = j_0 e^{i\Omega t}$, with constant current density j_0 and driving frequency Ω. The maximum of the displacement amplitude is found by solving

$$\frac{d|A_x(\Omega)|}{dt} = 0 \text{ and } \frac{d|A_y(\Omega)|}{dt} = 0. \tag{2.10}$$

This gives a resonance frequency of $\Omega_{max} = \omega^2 - \Gamma^2$. To simplify the following discussion, we assume in addition that the degree of nonadiabaticity is of the same order as the Gilbert damping constant $\xi \approx \alpha$. In this case, we can neglect to first order all terms proportional to $(\xi - \alpha)^2$ in the expression of the displacement amplitude and the maximum of the displacement amplitude is given by:

$$|A_x(\Omega_{max})| = |A_y(\Omega_{max})| = \frac{1}{2}|\frac{b_j j_0}{\Gamma}| \propto \frac{1}{\alpha}. \tag{2.11}$$

It is obvious that the vortex core motion precesses in the considered case on a circular path with the given amplitude which is proportional to the spin polarized current density. Assuming that the Gilbert damping constant α is small, one can use a Taylor series expansion of Γ and one can show directly that the amplitude is inversely proportional to the Gilbert damping parameter α. The proportionality relation follows directly from equation (2.7). Therefore materials with a low Gilbert damping parameter will lead to a larger amplitude of the movement of

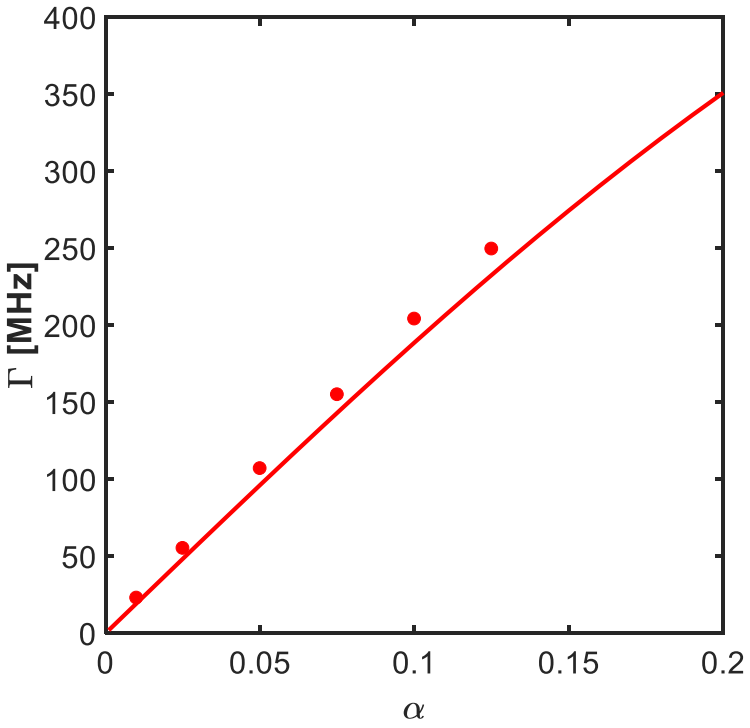

Figure 2.10: Damping constant Γ of the gyrotropic motion of the vortex core as a function of the Gilbert damping constant α. The solid line is determined with the analytic model and the dots are the results from micromagnetic simulations for a 500 nm $\times$ 500 nm $\times$ 10 nm sample. Γ scales approximately linear for small α.

the vortex core in case one utilizes heat pulses or pulsed currents to generate spin torque driven vortex core motion. The dependence of Γ on the Gilbert damping constant α is shown in fig. 2.10 for a sample size of 500 nm $\times$ 500 nm $\times$ 10 nm. The solid line corresponds to the analytical model and the dots are determined from fully micromagnetic simulations. It becomes obvious that in the case of a periodically driven vortex motion, the amplitude of the resulting stationary motion increases in case a material with low Gilbert damping is used, which helps in the experimental realization to use thermal spin transfer torque to drive and detect the magnetic vortex core motion. However, from equation (2.11) it becomes obvious that the maximal amplitude of the driven vortex motion is proportional to the spin polarized current density which, when created through a temperature gradient in a permalloy sample, is relatively small and the expected movements of the vortex core are below 100 nm, which is experimentally very difficult to resolve.

2.3 Extended Thiele Equation for Vortex Core Motion

Based on the good agreement between fully micromagnetic simulations and the analytic solutions from the Thiele equation, an extended form of the Thiele equation is derived in the following section to include, in addition to the conventional spin transfer torque term driven by the inclusion of an electric current density, as discussed in the previous section, terms capturing the thermomagnonic torque, also often referred to as magnon spin transfer torque, as well as thermal fluctuations. The discussion of pure thermomagnonic torque has recently become the focus of studies in insulating ferrimagnets, such as yttrium iron garnet (YIG) [54], and magnetic insulators, such as Cu_2OSeO_3 [55], $BaFe_{1-x-0.05}Sc_xMg_0.05O_19$ [56], and $Y_3Fe_5O_{12}$ [57]. Here special emphasis has been on the study of domain wall driven motion [58, 59] and the manipulation of skyrmions [59, 60]. But also in conducting materials, as in the considered permalloy sample, pure thermomagnonic spin torques can couple the magnetic moments to the temperature gradient even in the absence of electric charge flows [45, 61]. The generalized Thiele equation, which describes the vortex core motion as discussed in the previous section, has the following form:

$$\vec{F} + \vec{G} \times \vec{V} + \alpha \hat{D} \vec{V} = 0. \tag{2.12}$$

Here $\vec{V} = d\vec{R}/dt$ is the velocity of the vortex core and $\vec{R} = (x(t), y(t))$ is the vortex core position. As introduced in the previous section $\vec{G}$ is the gyrovector and $\hat{D}$ the dissipation tensor. The force vector $\vec{F}$ includes now the force due to the stray field ($\vec{F}_{st}$), spin transfer torques via electric currents $\vec{F}_{ch}$, pure thermomagnonic torques ($\vec{F}_m$), and thermal fluctuations ($\vec{F}_{fl}$). Using the superposition principle the force can therefore be written as

$$\vec{F} = \vec{F}_{st} + \vec{F}_{ch} + \vec{F}_m + \vec{F}_{fl}. \tag{2.13}$$

The force due to the stray field can be again derived by assuming a parabolic potential with stiffness constant $\tilde{\kappa}$ as discussed in the previous section:

$$\vec{F}_{st} = -m\omega_r^2 x \hat{e}_x - m\omega_r^2 y \hat{e}_y \text{ with } \tilde{\kappa} = \frac{1}{2} m\omega_r^2. \tag{2.14}$$

The force due to electric charge currents has been discussed in detail in the previous section and is given by:

$$\vec{F}_{ch} = b_j \vec{G} \times \vec{j} + \xi b_j \hat{D} \vec{j}, \tag{2.15}$$

where b_j describes again the coupling between the magnetization and the electric charge carriers. Since the parameter ξ, which describes the degree of nonadiabaticity, is often very small, the force is often approximated by $\vec{F}_{ch} \approx b_j \vec{G} \times \vec{j}$.

To include a pure thermomagnonic torque, we follow the approach chosen by Tatara [59]. In the case of transport phenomena attributed to charge carriers, Luttinger introduced a fictitious scalar field, also called gravitational potential, which couples to the local energy density by an interaction Hamiltonian [62]. Several approaches have been attempted to apply a similar formalism to pure thermal case. However, those approaches often led to wrong thermal coefficients [63, 64] or nonphysical divergences arose from an unmodified approach [65]. Those difficulties can be prevented by replacing the scalar potential formalism by a vector potential formalism [66, 67]. The vector potential form of the interaction Hamiltonian describing the thermal effect is given by

$$H_m \equiv -\int \vec{j}_E(\vec{r},t)\cdot\vec{A}_m(\vec{r},t)d^3r, \tag{2.16}$$

where $\vec{A}_m(\vec{r},t) = \vec{\nabla}T/T$ is the thermal vector potential and $\vec{j}_E(\vec{r},t)$ the energy current density. Following the approach by Tatara [59], one can now calculate the thermally driven dynamics of a spin structure as a linear response to the interaction Hamiltonian (2.16) and the force in the extended Thiele equation takes the following form

$$\vec{F}_m = \frac{2Ja^2}{\hbar}\vec{G}\times\vec{j}_m^{(2d)}. \tag{2.17}$$

In the equation above one has already made the assumption that the magnon current density is an effective $2d$ current density within a thin film plane, i.e. $\vec{j}_m^{(2d)} = \vec{j}_m t$. As defined in the previous section, t is the thickness of the permalloy sample, J the exchange constant, and a the lattice parameter. Applying a semiclassical approach with the relaxation time approximation [68] the magnon current can be expressed as

$$|\vec{j}_m^{(2d)}| = \frac{a^2}{(2\pi)^2}\int k_x(\hat{a})_k^\dagger(\hat{a})_k d^2k \tag{2.18}$$

where $(\hat{a})_k^\dagger$ and $(\hat{a})_k$ are the magnon creation and annihilation operator. Neglecting higher order processes, such as magnon-magnon interactions, one can show that the relaxation time is determined only by the Gilbert damping parameter α and the magnon current, here assumed to be parallel to the x axis, is given by [23]

$$j_m = \frac{\pi}{26}a^2\left(\frac{k_B}{\hbar v_m}\right)^2\frac{T}{\alpha}\frac{dT}{dx}, \tag{2.19}$$

where v_m is the effective velocity of the magnon, and k_B the Boltzmann constant. The effective magnon velocity can be estimated via $v_m = \frac{2A}{(l_{ex}\mu_0 M_s/\gamma)}$, which gives for permalloy a value of approximately 1010 m/s, which is two orders of magnitude larger compared to the antiferromagnet Cr_2O_3 [69].

To introduce a force describing thermal fluctuation, one has to introduce stochastic fields whose time correlations satisfy the fluctuations-dissipation theorem [70, 71]. This approach is similar to fully micromagnetic simulation including a random stochastic field $\nu\vec{H}_\nu$ with stochastic parameter ν to mimic temperature fluctuations. However, since we are only interested in the overall magnitude of the resulting motion, we chose a simplified approach by introducing a direct force as done by Tatara [59]. Here the direct force arises from the annihilation of vortices contributing to the entropy production. The direct thermal force can be expressed as

$$\vec{F}_{fl} = \frac{\gamma_\nu}{T}\vec{\nabla}T. \tag{2.20}$$

Since the annihilation of vortices requires a finite excitation energy, the parameter γ_ν vanishes fast as the temperature approaches zero. Therefore the force vanishes at $T = 0$. The parameter γ_ν can be estimated using the fluctuation dissipation theorem [72], where the stochastic parameter ν^2 is given by the ratio of the thermal energy to the magnetic energy:

$$\nu^2 \approx \frac{2\frac{\alpha}{1+\alpha^2}k_BT}{\mu_0 M_s^2 V}, \tag{2.21}$$

where V is the sample volume. One can now use the nominator to approximate the prefactor of the force caused by thermal fluctuations entering the Thiele equation:

$$\frac{\gamma_\nu}{T} \approx \frac{2\frac{\alpha}{1+\alpha^2}k_BT}{T} \approx \frac{2k_B\alpha}{1+\alpha^2}. \tag{2.22}$$

Since the velocity of the vortex core is in the film plane, and therefore perpendicular to the gyrovector, one can rewrite the generalized Thiele equation (2.12) in the following form:

$$\vec{G} \times \vec{F} - G_0^2\vec{V} + \alpha D_0 \vec{G} \times \vec{V} = 0. \tag{2.23}$$

Using the expression for $\vec{G}\times\vec{V}$ from (eq. (2.23)) and inserting this expression into the original equation (2.12), one can derive the following equation for the velocity of the vortex core:

$$(G_0^2 + \alpha^2 D_0^2)\vec{V} = \vec{G} \times \vec{F} - \alpha D_0 \vec{F}. \tag{2.24}$$

To discuss the different contributions from a charge current and a pure magnon current, a homogeneous charge current parallel to the x axis and a linear temperature gradient along the x axis is taken into consideration. In the absence of a charge current, a pure magnon current, and any thermal fluctuation, just including the force F_{st} for the stray field, the energy landscape of the vortex has its minimum in the center of the sample. An excited vortex, i.e. a vortex with the

core not in the center position, performs an exponentially damped spiral rotation around its equilibrium position with the angular eigenfrequency

$$\omega = -\frac{pG_0 m\omega_r^2}{G_0^2 + \alpha^2 D_0^2}, \text{ with } \tilde{\kappa} = \frac{1}{2} m\omega_r^2, \tag{2.25}$$

and the damping constant

$$\Gamma = -\frac{\alpha D_0 \omega_r^2}{G_0^2 + \alpha^2 D_0^2}. \tag{2.26}$$

From the two equations above, equations (2.25) and (2.26), one obtains the following relation

$$\alpha D_0 = \frac{p\Gamma G_0}{\omega}. \tag{2.27}$$

Using equation (2.27), and the following relations

$$\frac{p\omega\Gamma}{\omega^2 + \Gamma^2} = \frac{\alpha D_0 G_0}{G_0^2 + \alpha^2 D_0^2}, \tag{2.28}$$

$$\frac{\omega^2}{\omega^2 + \Gamma^2} = \frac{G_0^2}{G_0^2 + \alpha^2 D_0^2}, \text{ and} \tag{2.29}$$

$$\frac{\Gamma^2}{\omega^2 + \Gamma^2} = \frac{\alpha^2 D_0^2}{G_0^2 + \alpha^2 D_0^2}, \tag{2.30}$$

one obtains the following equations of motion for the x and y coordinates of the vortex core:

$$\begin{aligned}
\frac{dx}{dt} =& - p\omega y - \Gamma x - (1 + \frac{\Gamma^2}{\omega^2 + \Gamma^2}\frac{\xi - \alpha}{\alpha}) b_j j \\
& - \frac{\omega^2}{\omega^2 + \Gamma^2}\frac{2Ja^2}{\hbar} j_m - \frac{\Gamma^2}{\omega^2 + \Gamma^2}\frac{\gamma_\nu}{T}\frac{\partial T}{\partial x}, \\
\frac{dy}{dt} =& + p\omega x - \Gamma y + \frac{p\omega\Gamma}{\omega^2 + \Gamma^2}\frac{\xi - \alpha}{\alpha} b_j j \\
& - \frac{p\omega\Gamma}{\omega^2 + \Gamma^2}\frac{2Ja^2}{\hbar} j_m + \frac{\omega^2}{\omega^2 + \Gamma^2}\frac{1}{G_0}\frac{\gamma_\nu}{T}\frac{\partial T}{\partial x}.
\end{aligned} \tag{2.31}$$

Here the first two terms in each equation are responsible for the damped spiral rotation, the second terms are proportional to the involved charge current density and describes the motion due to the spin transfer torque connected to charge carriers. The third terms are proportional to the pure magnon current and describe therefore the pure magnonic motion of the vortex core. The last terms in each equation describe the average motion of the vortex core due to random thermal fluctuations. It should be mentioned here that a fully micromagnetic code, which includes thermal fluctuations along a temperature gradient, would be able to fully describe the motion, hereby replacing the last two terms in the equations of motion. While fully micromagnetic simulations including a stochastic field can be

done assuming a constant temperature within the sample (see for example [70]) we are not aware of the attempt to do so including a temperature gradient. The inclusion of a temperature gradient would require an extremely small time step in the micromagnetic simulations to cover the pure magnonic motion correctly. To evaluate the vortex core motion and compare the results to experimental data, we have solved the equations of motion (2.31) numerically. The main advantage of this method is that one can analyse the different contributions to the final core position separately. The resulting core motion can be again described by a damped spiral motion, starting at the center of the sample, i.e. at $\vec{R}(t = 0) = (0, 0)$ and ending at the new equilibrium position $\vec{R}(t \to \infty) = (\Delta x, \Delta x)$, as shown in fig. 2.11.

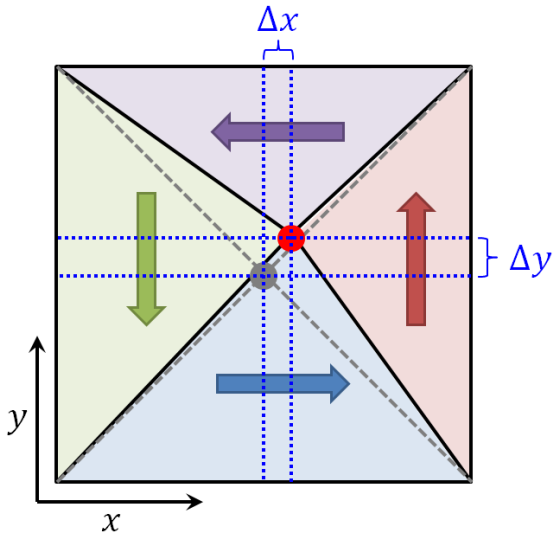

Figure 2.11: Sample geometry for the extended Thiele equation. At the beginning the vortex core is at the center of the sample, i.e. $\vec{R} = (0, 0)$ and shown as grey dot. Due to the additional forces, the vortex core undergoes a damped spiral rotation into its new equilibrium position, i.e. $\vec{R} = (\Delta x, \Delta y)$ and shown as red dot.

Similar to the case discussed in the previous section, where only a spin polarized charge current has been considered, it is possible to calculate the final core position analytically. Neglecting the forces due to spin polarized charge currents and random thermal fluctuation, the equations of motion (2.31) are given by

$$\begin{aligned} \frac{dx}{dt} &= -p\omega y - \Gamma x - v_{mx}, \\ \frac{dy}{dt} &= +p\omega y - \Gamma x - v_{my}. \end{aligned} \tag{2.32}$$

Here the components of the magnon velocity vector are defined as

$$v_{mx} = \frac{\omega^2}{\omega^2 + \Gamma^2} \frac{2Ja^2}{\hbar^2} j_m,$$
$$v_{my} = \frac{p\omega\Gamma}{\omega^2 + \Gamma^2} \frac{2Ja^2}{\hbar^2} j_m. \tag{2.33}$$

In order to calculate the final core deflection due to the pure magnon transfer torque, the solution for the vortex core needs to be stationary, i.e. $\frac{dx}{dt} = \frac{dy}{dt} = 0$. Under this condition the final core deflection is given by:

$$\begin{pmatrix} \Delta x^m_{end} \\ \Delta y^m_{end} \end{pmatrix} = \frac{1}{\Gamma^2 - \omega^2} \begin{pmatrix} -\Gamma v_{mx} + p\omega v_{my} \\ p\omega v_{mx} - \Gamma v_{my} \end{pmatrix} = \begin{pmatrix} 0 \\ -\frac{p\omega}{\Gamma^2+\omega^2} \frac{2Ja^2}{\hbar} j_m \end{pmatrix}. \tag{2.34}$$

This result can be directly compared with the obtained numerical results by solving the generalized equations of motion (2.23).
In the following, numerical solution of the extended Thiele equation (2.12) will be discussed including the forces associated with the stray field, the spin transfer torque via electric and pure magnon currents, and thermal fluctuations. Besides the previously discussed parameters, a saturation magnetization of 8×10^5 [A/m], a Gilbert damping constant of 0.006 [73], and a non-adiabaticity parameter of 0.05 [47] are used. According to the experiment the lateral sample dimension is chosen to be 2 μm and the sample thickness is 20 nm. Starting with the vortex core in the center of the sample, the resulting vortex core motion can be described again by a damped spiral rotation approaching the new equilibrium position, which in this case differs from the central position due to the involved forces. Such a motion is shown in fig. 2.12 for a vortex polarity of $p = 1$ and a chirality of $c = 1$. At $t = 0$ the vortex core is in the center of the sample, i.e. $\vec{R} = (0, 0)$.

To analyze the different contributions to the overall vortex core motion, the x- and y-amplitudes are shown separately in fig. 2.13(a). The x-component of the vortex core is shown as a solid line, and the y-component of the vortex core is shown as a dotted line. For the case where only the charge spin transfer torque or the thermomagnonic torque are considered, the analytic solutions (see equations (2.8) and (2.34)) are shown as black dashed lines. By analyzing the contributions to the final core position, one finds that the motion induced by spin transfer torque due to spin polarized charge currents is as expected zero in the direction of the temperature gradient (parallel to the x axis). However, it has a non-vanishing component in the direction perpendicular to the temperature gradient (parallel to the y axis). As already discussed in the previous section using this approach as well as fully micromagnetic approach, the final core deflection Δy is relatively small (see fig. 2.13 (b)). With a temperature gradient of 100 [mK/nm] which corresponds to a charge current density of 4×10^9 A/m^2 this contribution is below

1 nm. This small movement is mainly caused by the relatively small spin-Seebeck coefficient for permalloy and leads to a relatively bad efficiency to create charge currents using a temperature gradient. This movement is certainly below the resolution feasible in an experimental setup. However, the movement induced by pure magnon currents is for the given situation in the order of a few hundred nm. As can be seen in fig. 2.13(c) the final core deflection perpendicular to the temperature gradient is zero, as also expected from the analytic solution for the final core position. The final core position perpendicular to the temperature gradient is at 215 nm and therefore possible to detect experimentally. Using the involved magnon velocities in equation (2.33) and equations (2.28) and (2.29), one can easily show that the magnon velocity in the y direction, i.e. perpendicular to the temperature gradient, is proportional to the Gilbert damping parameter α and therefore much smaller than the magnon velocity in the x direction, i.e. parallel to the temperature gradient. For the considered case the magnon velocity in the y direction is about 70 times larger than the magnon velocity in x direction. A similar behavior has been derived theoretically for the magnon velocity for thermally driven skyrmions [23]. In fig. 2.13(d) the average contribution accounting for thermal fluctuations are shown. Due to the random nature of those fluctuations, a final core deflection parallel and perpendicular to the temperature gradient is expected. For the assumed temperature gradients, those movements are in the order of 3 nm, which has been also shown using a stochastic Landau Lifshitz equation by Machado et al. [70]. Therefore only the movement caused by pure magnon currents is accessible in an experimental setup.

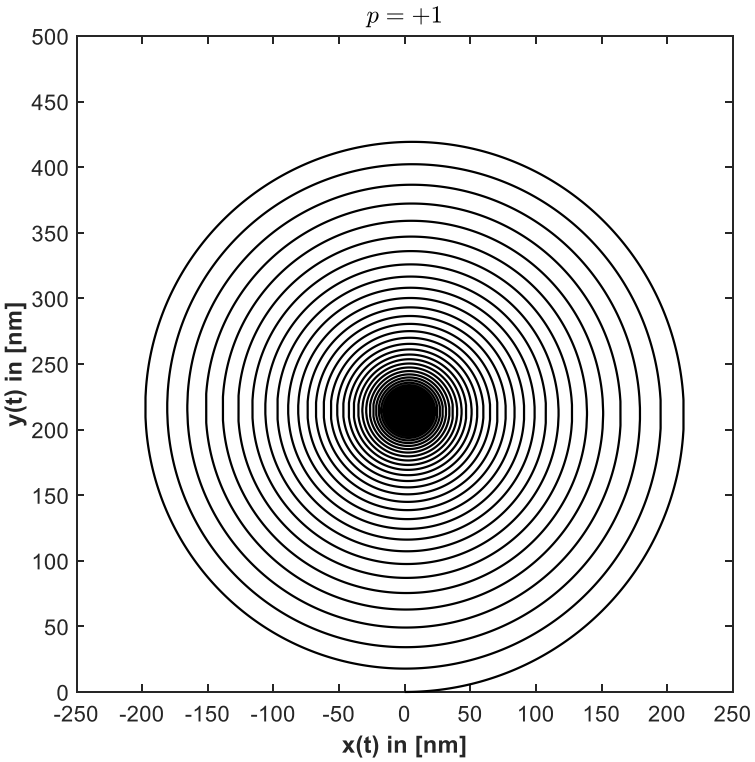

Figure 2.12: Damped spiral vortex core motion for $p = 1$ and $c = 1$ described by the extended Thiele equation, including forces due to the stray field, electric spin polarized currents, pure magnonic currents, and thermal fluctuations. At $t = 0$ the vortex core is in the center of the sample, i.e. $\vec{R} = (0, 0)$. A linear temperature gradient of $-100\,\mathrm{mK/nm}$ in x direction is applied, assuming that the left side of the sample is heated up to $500\,\mathrm{K}$ and the right side is kept at $300\,\mathrm{K}$. The effective magnon velocity is estimated as $1010\,\mathrm{m/s}$.

To verify that the experimentally accessible core motion is indeed caused by pure spin magnon currents, one can change the polarity of the vortex in the experiment. Figure 2.14(a) and (b) show the resulting vortex core motions for the two cases (i.e. $p = +1$ and $p = -1$). As discussed in the previous section the main contribution to the final core position is caused by the pure magnon spin transfer torque. This effect can be also seen in the two figures. In fig. 2.14(a) the vortex core moves mainly in the positive y direction, and in fig. 2.14(b) it moves mainly in the negative y direction as expected from the extended Thiele equation.

The different contributions to the overall vortex core motion are shown in comparison in fig. 2.15. The figures on the left (fig. 2.15(a), (c), (e), and (g)) show the case for the vortex polarization $p = +1$, and the figures on the right (fig. 2.15(b), (d), (f), and (h)) for a reversed polarization $p = -1$. Figure 2.15(a) and (b) show the x- and y-Amplitudes in the case that all forces are included. Figure 2.15(c) and (d) show the x- and y-Amplitudes in the case that only forces due to the stray field and the charge spin transfer torque are included. As expected the

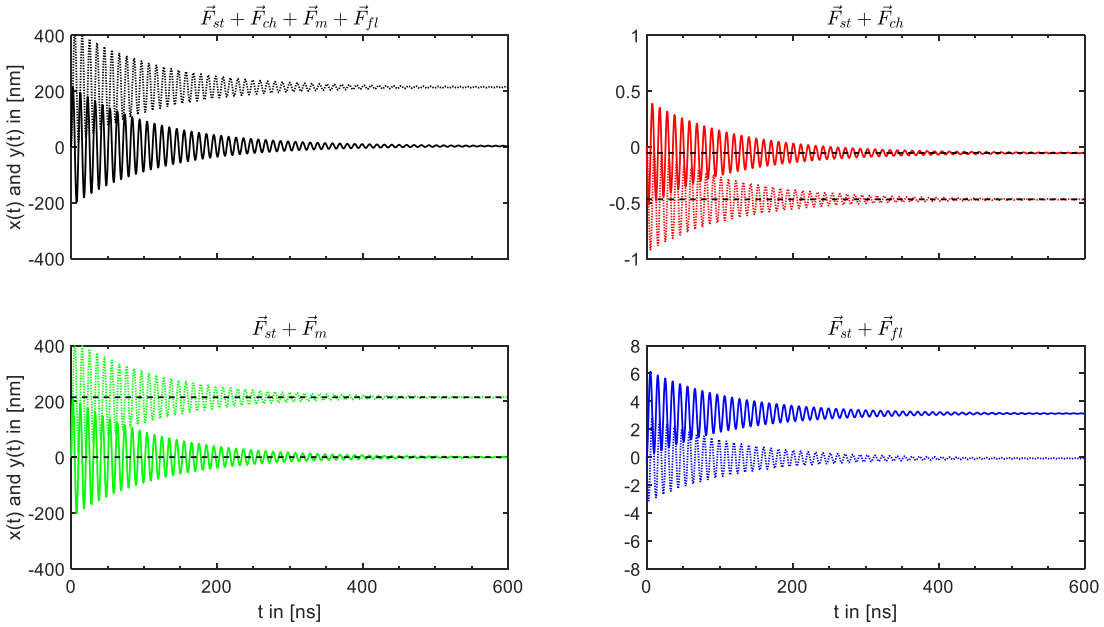

Figure 2.13: Contributions to the damped spiral vortex core motion for $p = 1$ and $c = 1$: (a) all forces includes, (b) forces due to the stray field and charge spin transfer torque, (c) forces due to stray field and magnon spin transfer torque, and (d) forces due to stray field and thermal fluctuations. At $t = 0$ the vortex core is in the center of the sample, i.e. $\vec{R} = (0, 0)$. A linear temperature gradient of $-100\,\mathrm{mK/nm}$ in x direction is applied, assuming that the left side of the sample is heated up to 500 K and the right side is kept at 300 K. The effective magnon velocity is estimated as $1010\,\mathrm{m/s}$.

vortex core motion perpendicular to the temperature gradient changes its sign. However, the final core position is to small to be detected in an experimental setup. Figure 2.15(e) and (f) show the x- and y-Amplitudes in the case that only forces due to the stray field and the magnon spin transfer torque are included. Again, the vortex core motion perpendicular to the temperature gradient changes its sign. Since the final core position is of the order of 200 nm, this motion in the opposite directions, depending on the polarization of the vortex, can be used to verify experimentally that the motion perpendicular to the temperature gradient is indeed caused by magnon spin transfer torque. Figure 2.15(g) and (h) show the motion caused by random thermal fluctuations and does not changes its sign.

In an experiment, where one side of the sample is heated to create a large temperature gradient, one has to take into account that the hot side of the disk will reach temperature, which can have a demagnetizing effect on a small region on the hot side of the sample. To estimate the movement caused by this demagnetizing effect, it is assumed that 10% of the left side of the sample is exposed to a reduction in the saturation magnetization as well as the exchange coupling. The new vortex core position is determined by fully micromagnetic simulations.

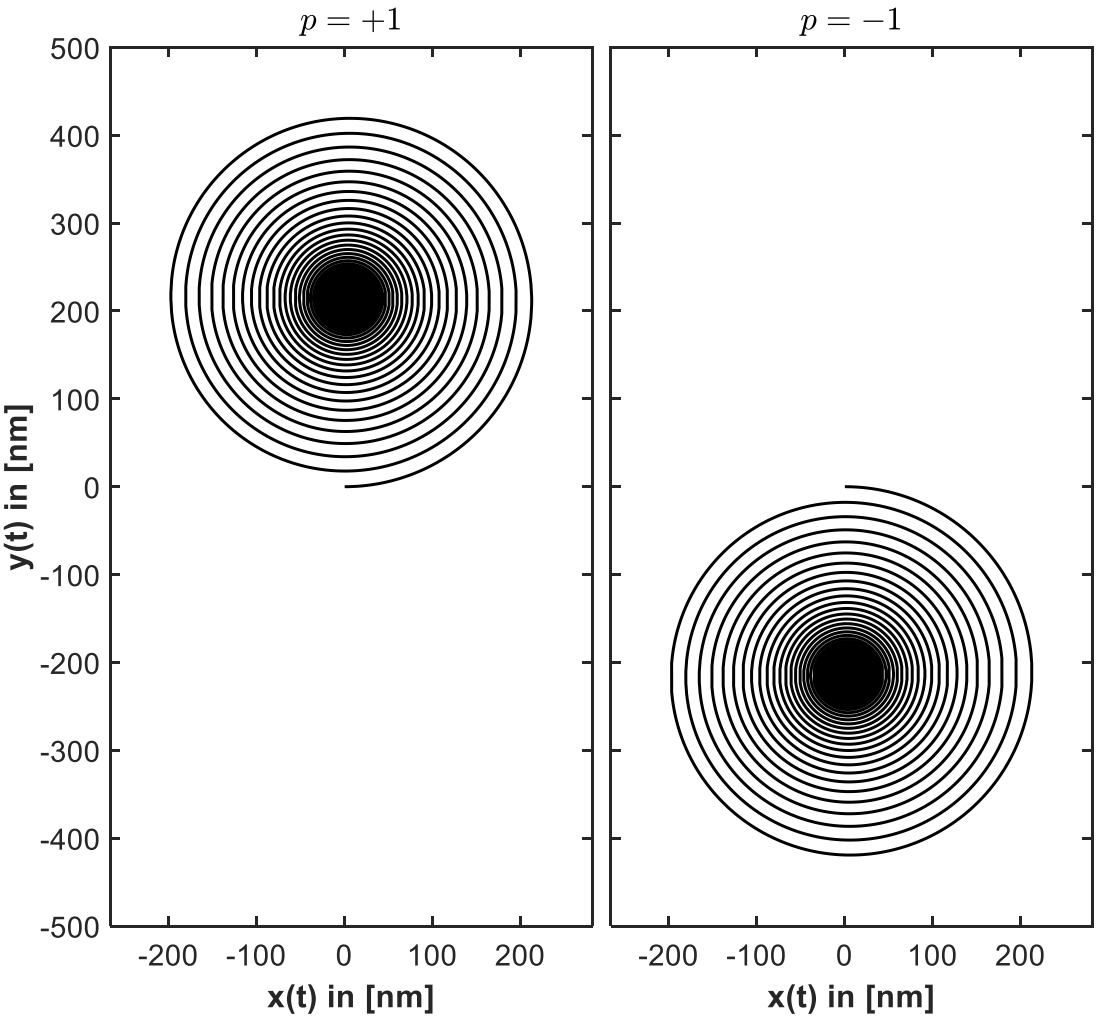

Figure 2.14: Damped spiral vortex core motion for different polarities: (a) $p = +1$ and (b) $p = -1$ described by the extended Thiele equation, including forces due to the stray field, electric spin polarized currents, pure magnonic currents, and thermal fluctuations. At $t = 0$ the vortex core is in the center of the sample, i.e. $\vec{R} = (0, 0)$. A linear temperature gradient of $-100\,\mathrm{mK/nm}$ in x direction is applied, assuming that the left side of the sample is heated up to 500 K and the right side is kept at 300 K.The effective magnon velocity is estimated as $1010\,\mathrm{m/s}$.

However, due to the nature of the problem, those simulations require a very high spatial resolution to be able to resolve the vortex core, which's core radius is of the order of 10 nm. In a large sample of 2 μm $\times$ 2 μm where the vortex core motion is orders of magnitudes smaller than the dimensions of the sample, micromagnetic simulations with the required precision are not feasible. Therefore the influence of the demagnetizing effect will be discussed in a much smaller sample of 100 nm $\times$ 100 nm with a spatial resumption of 1.25 nm and the known scaling behavior (see fig. 2.9) will be used to estimate the movement due to demagnetizing effects in the large sample used in the experiment. Figure 2.16 shows the results of the demagnetizing effects using micromagnetic simulations assuming that the

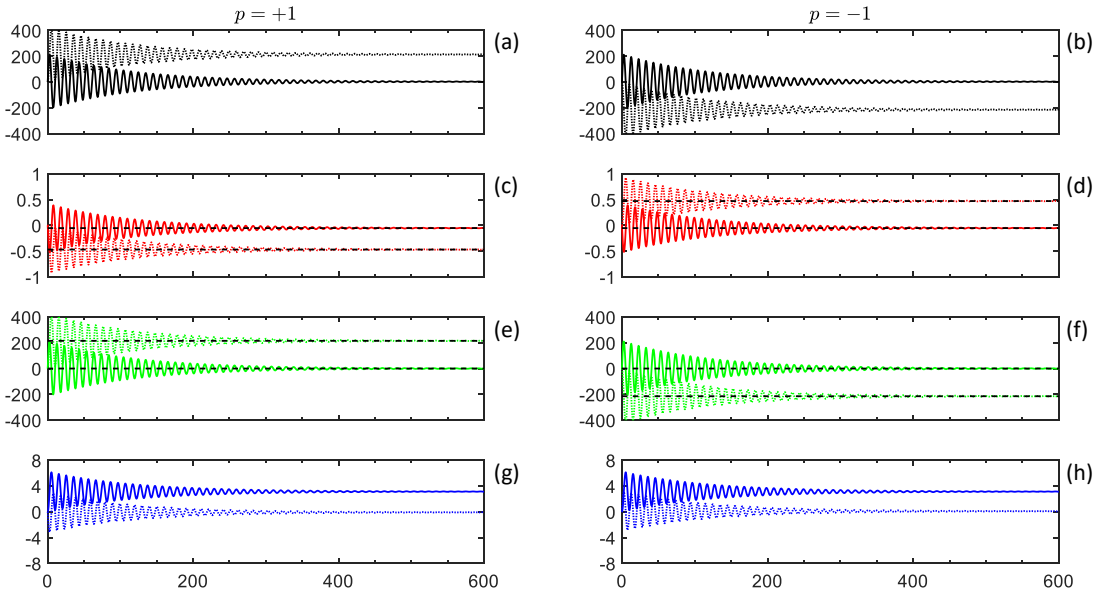

Figure 2.15: Contributions to the damped spiral vortex core motion for $p = 1$ and $c = 1$: (a) and (b) all forces includes, (c) and (d) forces due to the stray field and charge spin transfer torque, (e) and (f) forces due to stray field and magnon spin transfer torque, and (g) and (h) forces due to stray field and thermal fluctuations. At $t = 0$ the vortex core is in the center of the sample, i.e. $\vec{R} = (0, 0)$). A linear temperature gradient of $-100\,\mathrm{K\,nm^{-1}}$ in x direction is applied, assuming that the left side of the sample is heated up to 500 K and the right side is kept at 300 K. The solid lines are the components parallel to the temperature gradient ($x(t)$), and the dashed lines are the components perpendicular to the temperature gradient ($y(t)$).The effective magnon velocity is estimated as 1010 m/s

magnetization in a strip of 10 nm on the hot site of the sample is reduced by 40%, 50%, 60%, 70%, 80%, and 90%. For all simulations the vortex is initialized off center (see the blue dot in fig. 2.16(b)) and then the system is relaxed. The final vortex core position is determined by finding the global peak using a two dimensional polynomial fit and extremum detection. For the case that the strip at the hot side of the sample is completely demagnetized, the vortex core will move to the new center position in the smaller sample geometry. The results of the micromagnetic simulations are shown in fig. 2.16(a). The red dots indicate the vortex core movement in the x direction. Positive values indicate that the core is moving away from the hot side of the sample. The red and blue stars indicate the new relaxed position assuming that the strip at the hot side of the sample is completely demagnetized. In this case the vortex core simply assumes the new center position in the less wide rectangular shaped sample, as shown in fig. 2.16(b). As expected the core movement in the positive x direction, further away from the hot side of the sample, shows a linear dependence with increasing demagnetizing effects (i.e. decreasing M_s values). Due to the symmetry of the problem, there is no overall movement in the y direction. The movements in x

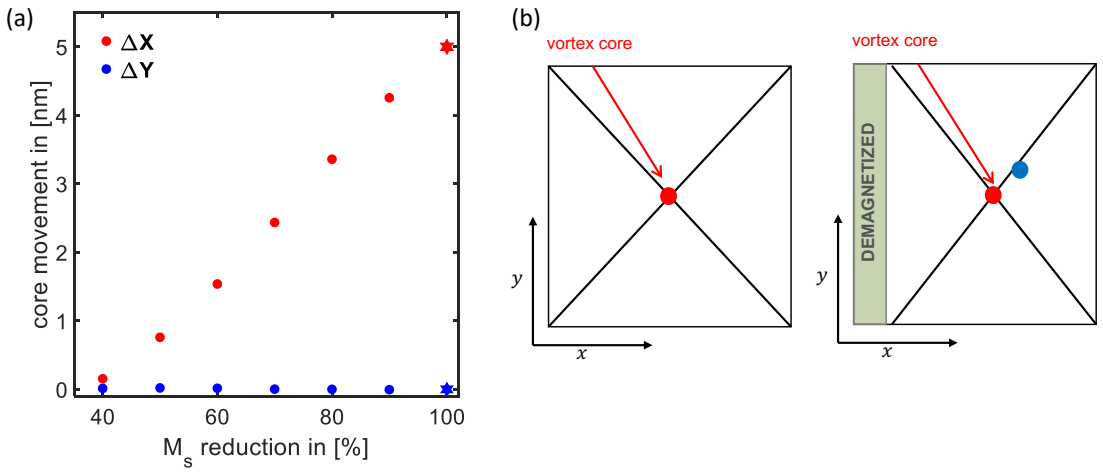

Figure 2.16: (a) Core movement for a 100 nm × 100 nm × 20 nm permalloy disk, assuming that 10% of the sample on the hot side is affected by a reduction in the saturation magnetization and the exchange coupling. The overall core motion under this new condition has been simulated with fully micromagnetic simulations and a lateral resolution of 1.25 nm. The hot side is on the left side of the sample. Positive values in the x direction indicate a movement away from the hot side. The red dots indicate the vortex core movement in the x direction and the blue dots the movement in the y direction. The red and blue stars show the result assuming that 10 nm of the sample are completely demagnetized. In this case the vortex core would move in the new center position, which is in this case 5 nm to the right, away from the demagnetized region, as illustrated in (b). The red dot shows the new equilibrium position for the case where no demagnetizing effects are present (left) and where the fill strip at the right side of the sample is fully demagnetized (right). The blue dot in the right figures indicates the off-center initialization of the vortex state for the micromagnetic simulations.

and y directions are independent from the vortex polarity. This linear behavior above 40% reduction in the saturation magnetization, together with the known scaling behavior from the Thiele equation (see fig. 2.9), can be used to estimate the overall movement of the vortex core due to demagnetizing effects, assuming again that 10% of the sample region on the hot end is exposed to demagnetizing effects due to the temperatures this side of the sample is exposed to.

The different contributions to the final vortex position as a function of the applied temperature gradient $|dT/dx|$ are shown in fig. 2.17(a)-(d). Figure 2.17(a) and (c) show the contributions from the charge spin transfer torque, the magnon spin transfer torque, and the thermal fluctuations for the polarity $p = +1$ (left column) and $p = -1$ (right column). All movements scale linear with the temperature gradient. Since the length scales differ by order of magnitudes, fig. 2.17 (b) and (d) show a magnification of the movements below 3 nm. Figure 2.17(e) shows the expected movement due to demagnetization effects, which are independent of the vortex polarity. As discussed earlier the experimental observable movement

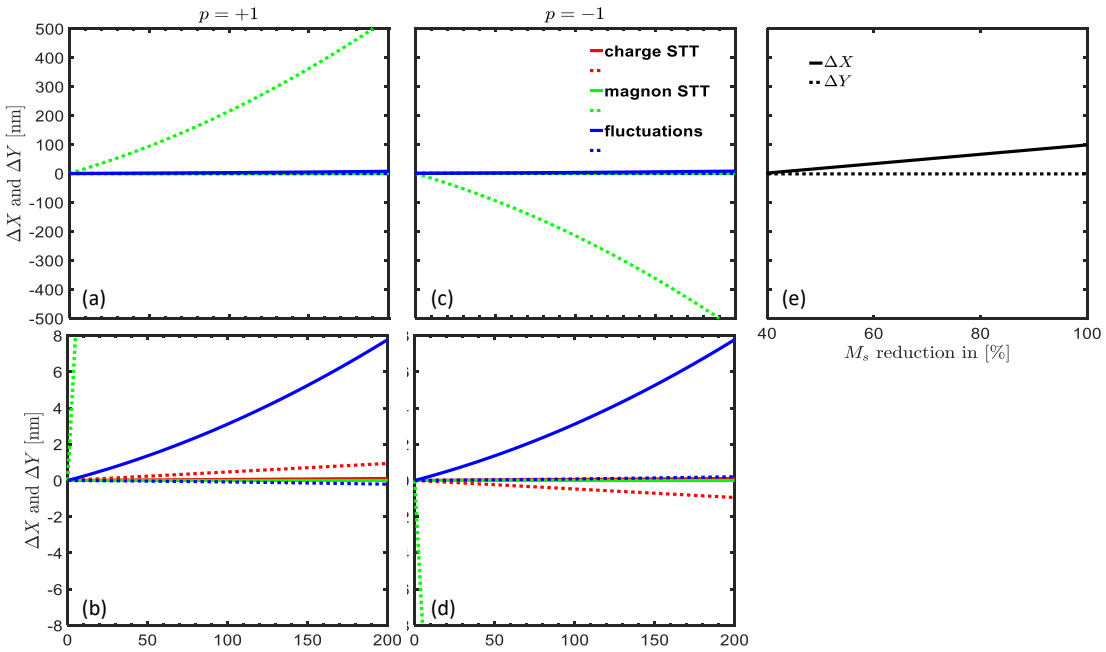

Figure 2.17: (a)-(d) Finale core position as a function of the applied temperature gradient for the different contributions caused by charge spin transfer torque (red), magnon spin transfer torque (green), and thermal fluctuations (blue) as discussed in fig. 2.15. The solid lines show the movement parallel to the temperature gradient (ΔX) and the dashed lines show the movement perpendicular to the temperature gradient (ΔY). The first column is for a vortex polarity $p = +1$, and the second column is for a vortex polarity $p = -1$. (e) shows the expected core movement as a function of the M_s reduction cause by demagnetization effects at the hot side of the sample. Those movements are independent of the vortex polarity.

perpendicular to the direction of the temperature gradient (y direction) is caused by magnon spin transfer torque. For different vortex polarities, this movement changes its sign, and can be identified by the experiment. The experimental observable movement along the direction of the temperature gradient (x direction) is caused by demagnetization effects and is always directed away from the hot side of the sample, independent of the vortex polarity.

2.4 Extended Thiele Equation for Coupled Vortices

The extended Thiele equation is also very useful to model the dynamics of magnetostatically coupled vortices. In addition to the studies of the gyrotropic motion of an individual vortex, there are several studies on the dynamics of coupled vortices [14, 35, 53, 74–77]. The spatially separated disks are sufficiently close to each other, that the magnetostatic (dipolar) interaction affects the vortex gyration in the individual disks. One particular important finding of those studies is the frequency splitting observed for the coupled system of two vortices. A more detailed study of the normal modes and their dependencies on the relative vortex state configuration in both disks can be found in [74]. Here, in addition to micromagnetic simulations, two coupled Thiele equations have been employed to describe the complex coupled vortex gyration in terms of the superposition of the two normal modes. To describe the experimental setup, in which one of the vortices is driven by an electric spin polarized current, one of the Thiele equations has been extended to include the spin polarized current density $\vec{j}$, as described in detail in the previous two sections. Since the second passive disk is in addition heated during the experiment to change the saturation magnetization and therefore the eigenfrequencies of the vortex gyration, it is necessary to distinguish between the corresponding gyro-vectors and the dissipation tensors for the driven (d) and heated (h) disk. The dynamics of this system are then modelled using the following coupled extended Thiele equations:

$$\begin{aligned} \vec{G}_d \times (\vec{V}_d + b_j\vec{j}) + \hat{D}_d(\alpha\vec{V}_d + \xi b_j\vec{j}) &= \vec{\nabla}_{\vec{R}_d} W(\vec{R}_d, \vec{R}_h), \\ \vec{G}_h \times \vec{V}_h + \hat{D}_h\alpha\vec{V}_h &= \vec{\nabla}_{\vec{R}_h} W(\vec{R}_d, \vec{R}_h). \end{aligned} \tag{2.35}$$

The first equation describes the vortex gyration in the driven disk, and the second equation describes the vortex motion in the heated disk. $\vec{R}_i = (x_i, y_i), i \in \{d, h\}$ is the vortex core elongation vector from the center of disk i and $\vec{V}_i = d\vec{R}_i/dt$ is the corresponding velocity vector. $b_j = P\mu_B/[eM_{sd}(1+\xi^2)]$ is the coupling constant between the applied current density $\vec{j}$ and the magnetization, where P is the spin polarization, and ξ the degree of nonadiabaticity [40]. M_{sd} is the saturation magnetization of the driven disk. The corresponding gyro-vectors depend on the saturation magnetization in each disk and are given by

$$\vec{G}_i = -\frac{2\pi M_{si}\mu_0 t p_i}{\gamma}\hat{e}_z \text{ with } i \in \{d, h\}. \tag{2.36}$$

Both gyro-vectors indicate the axes of precession perpendicular to the film plane, which for both disks is parallel to the z-axis. M_{sd} and M_{sh} are the saturation magnetization of the driven and heated disk. p_i is the polarity of the corresponding

vortex, μ_0 the vacuum permeability, t the sample thickness, and γ the gyromagnetic ratio. $\hat{D}_d$ and $\hat{D}_h$ are the two diagonal dissipation tensors, as discussed in more detail in the previous section, which are both proportional to the respective saturation magnetizations, M_{sd} and M_{sh}. In the coupled system the total potential energy can be written as

$$W(\vec{R}_d, \vec{R}_h) = W_0 + \frac{\kappa}{2}(\vec{R}_d^2 + \vec{R}_h^2) + c_d c_h(\eta_x X_d X_h - \eta_y Y_d Y_h). \tag{2.37}$$

The first term represents the potential energy for a central core position, i.e. $\vec{R}_i = (0, 0)$. The second term represents the stray field energy and for small deflections can be modelled as a parabolic potential [13] with stiffness constant $\tilde{\kappa}$. The third term reflects the magnetostatic energy between the side surfaces of the two disks [53], where η_x and η_y express the coupling strength along the x- and y-directions. c_i is the chirality of the corresponding vortex [14, 35, 53, 75]. To simulate the experiment the chirality and the polarity for both vortices were chosen to be $[p_d = +1, c_d = +1]$ and $[p_h = +1, c_h = +1]$. Each disk had a lateral size of 1800 nm and a thickness of 50 nm. The damping constant for the permalloy disk is set to $\alpha = 0.006$ [73].

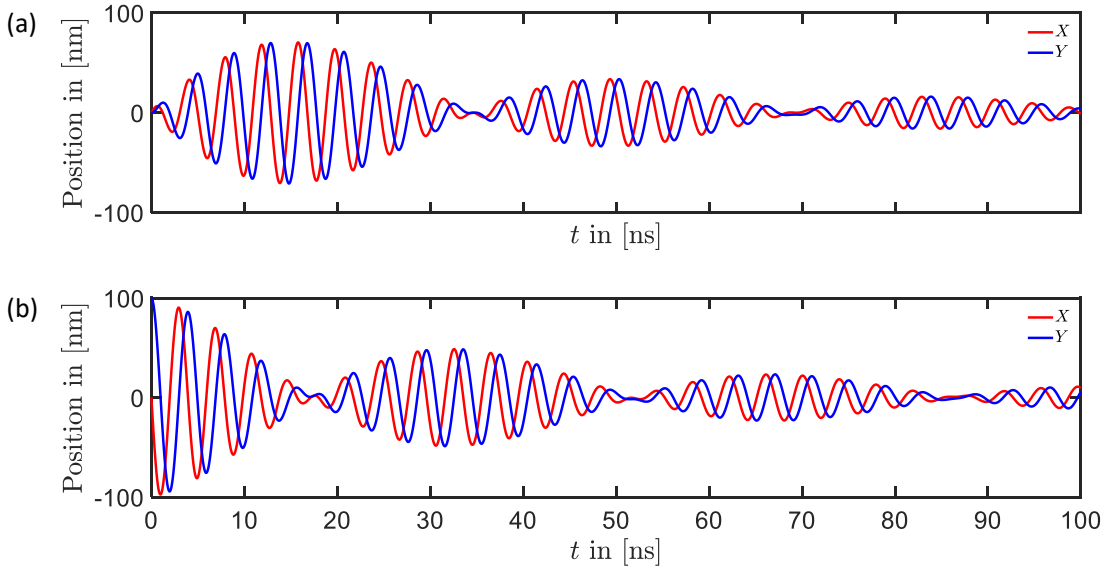

Figure 2.18: Example of the vortex gyration for $[p_d, c_d] = [+1, +1]$ and $[p_h, c_h] = [+1, +1]$ for ring down simulation. (a) The X (red line) and Y (blue line) components of the vortex core position vectors in $disk_d$ and (b) for $disk_h$. $disk_h$ has been displaced from the central position to an initial position, 100 nm in the $+y$ direction.

To excite all of the modes existing in the two coupled disks and to determine the eigenfrequencies of the coupled system numerically, so called ring-down experiments have been conducted. Here one of the vortex cores is initially displaced

from its center position. In the considered case the vortex core of one of the disks is displaced by 100 nm in the $+y$ direction and the resulting gyroscopic motion for the coupled vortices is recorded. Figure 2.18 shows the characteristic dynamics of the coupled vortex gyrations for the considered case. Here the saturation magnetization for both disks is the same, $M_{sd} = M_{sh} = 7.7 \times 10^5$ A/m. One recognizes as expected the beating pattern of the oscillating X and Y components of both vortices in addition to the crossover between the local maxima and minima of the modulation envelopes. A more detailed discussion of those ring-down simulations can be found in [74]. Figure 2.19 shows the frequency spectra obtained from the data shown in fig. 2.18. As expected the coupled system shows two eigenfrequencies, one below and one above the eigenfrequency of the individual systems at 254 MHz. The separation of the two eigenfrequencies is a measure of the coupling strength between the coupled system and can be used to adjust those parameters to experimental findings.

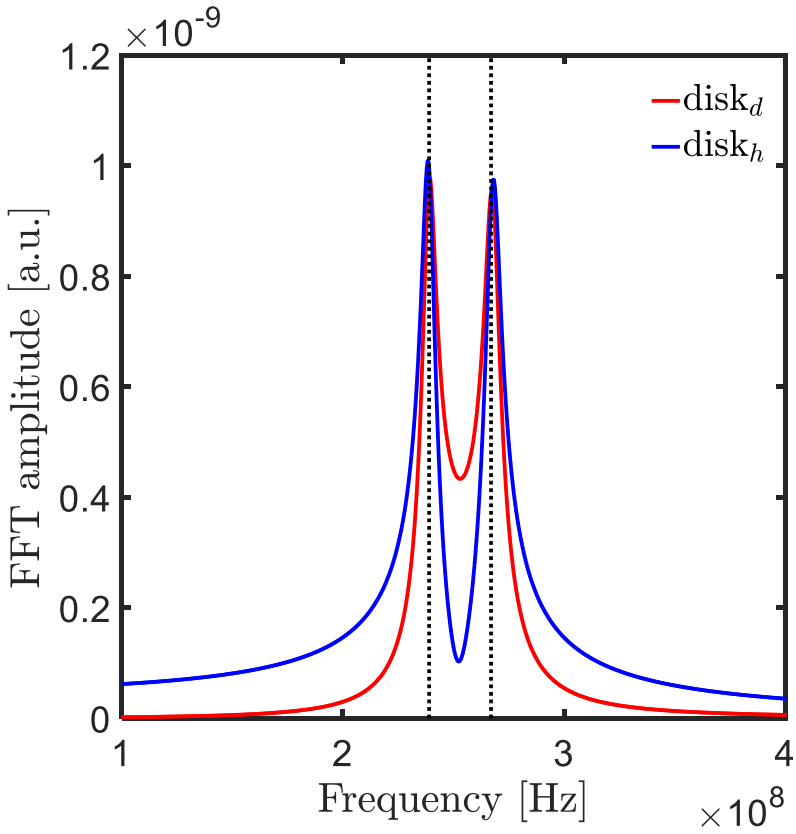

Figure 2.19: Frequency spectra obtained from the data shown in fig. 2.18. The red line is obtained from the gyromotion of the vortex in $disk_d$ and the blue line from the gyromotion of the displaced vortex in $disk_h$. The eigenfrequencies are as expected below and above the eigenfrequency of the single disk at 254 MHz.

In further simulations disk d is driven by an AC current which has an amplitude of 5×10^9 A/m^2 and varies sinusoidal with the driving frequency f_d. The driving frequency is set as in the experiment to the first peak in the frequency spectra of the coupled system, as shown in fig. 2.19. This peak corresponds to the case, where the coupled vortex oscillators are both in phase. However, due to experimental restrictions in the frequency resolution, small deviations from the main peak have been considered. The vortex in the heated disk, $disk_h$, is now placed in its original equilibrium position at the center of the disk. This disk is not driven and only coupled via the magnetostatic coupling to the driven disk. In the experiment this disk is heated to various temperatures to change its saturation magnetization. In the simulations this effect is included by changing the saturation magnetization M_{sh} of $disk_h$, while the saturation magnetization M_{sd} of the driven disk is kept constant. As a result one can analyze the resulting phase shift between the gyrotropic motion of the coupled vortices as a function of the saturation magnetization ratio M_{sh}/M_{sd}.

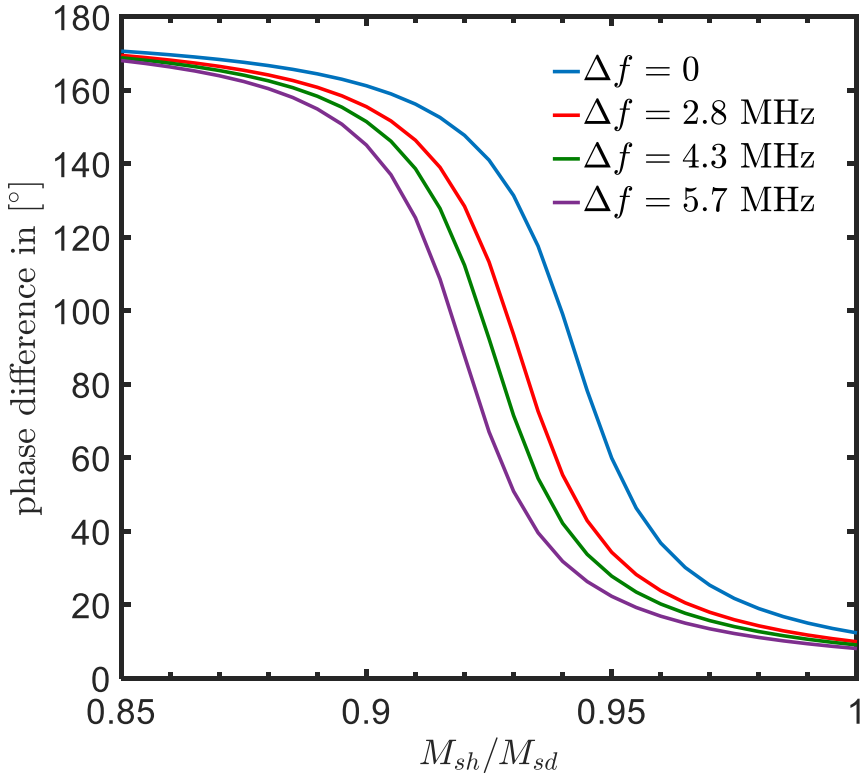

Figure 2.20: Phase difference for the two vortex gyrations as a function of the magnetization ratio $\frac{M_{sh}}{M_{sd}}$ of the heated disk and the driven disk. In the case that $\frac{M_{sh}}{M_{sd}} = 1$, both vortices gyrate in phase. For a phase ratio of $\frac{M_{sh}}{M_{sd}} = 0.85$ both vortices gyrate almost completely out of phase. The different colors indicate the detuning from the first eigenfrequency of the coupled system. Results for detuning of 0 MHz, 2.8 MHz, 4.3 MHz and 5.7 MHz to lower excitation frequencies than the first eigenfrequency are shown.

Figure 2.20 shows the phase difference between the two gyrotropic motions of the coupled vortices as a function of the saturation magnetization. Due to the selection of the driving frequency, one observes an almost zero phase difference, in case the two saturation magnetizations are the same, i.e. $M_{sh}/M_{sd} = 1$. In this case both vortices gyrate in phase. With a decreasing value of the saturation magnetization M_{sh} of the heated disk (M_{sh}/M_{sd} is decreasing), one can shift the resulting phase difference between the gyrotropic motion of the two coupled vortices to any value up to almost 180°, where both vortices gyrate out of phase. The different colors in fig. 2.20 belong to different detuning from the first eigenfrequency of the coupled system. Here a detuning to a lower frequency as the first eigenfrequency is assumed. For all cases it is possible to shift the phase difference between the in phase case to the out of phase case. However, with larger detuning slightly larger differences between the two saturation magnetizations are needed to reach the final phase difference.

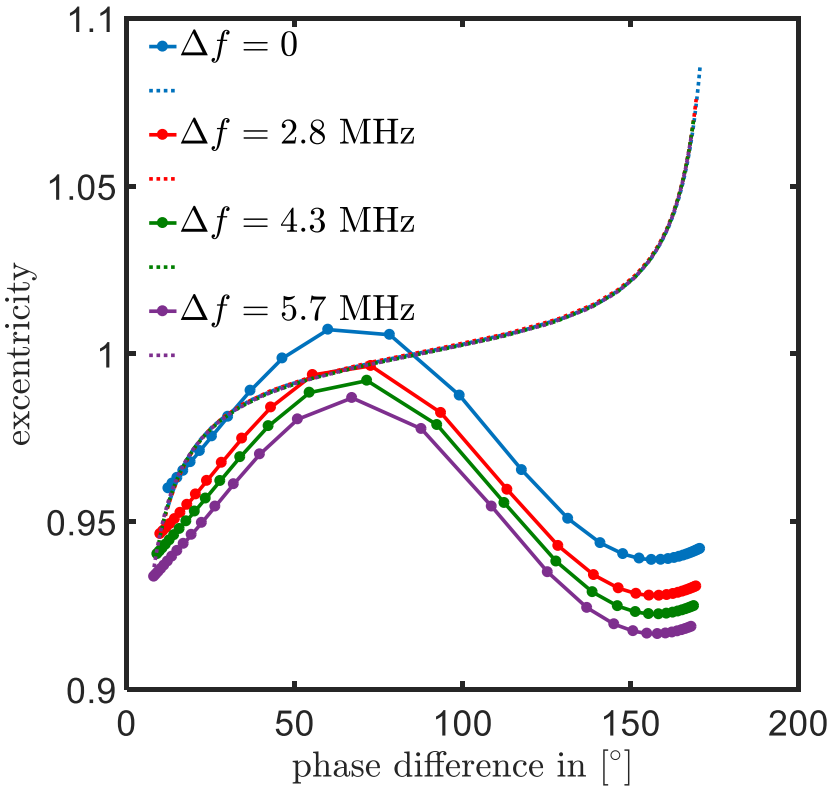

Figure 2.21: Eccentricity for the elliptical trajectory of the two vortex gyrations as a function of phase difference. The solid lines with the filled circles are the results for the driven $disk_d$, and the dotted lines are the results for the heated $disk_h$. The different colors indicate the detuning from the first eigenfrequency of the coupled system. Results for detuning of 0 MHz, 2.8 MHz, 4.3 MHz and 5.7 MHz to lower excitation frequencies than the first eigenfrequency are shown.

In addition to the phase difference analysis it is also possible to extract the eccentricity $e = A_X/A_Y$ of the elliptical trajectory, which can be also compared directly with experimental observations. Here A_X and A_Y are the amplitudes of the driven motion of the coupled vortices. Figure 2.21 shows the eccentricity of the elliptical trajectory of the driven and the heated disk as a function of the phase difference. The solid lines with the filled circles are the results for vortex motion in the driven disk and the dashed lines are the results for the vortex motion in the heated disk. The different colors indicate again different detuning from the eigenfrequency of the coupled system. The change of the eccentricity from $e > 1$ to $e < 1$ indicates a change in the overall elongation of the ellipse. If $e > 1$ the ellipse is elongated along the x-axis, and if $e < 1$ the ellipse is elongated along the y-axis. Taking detuning into account the eccentricity of the driven disk stays below 1, indicating an elongation along the y axis. Only in the case with no detuning is the eccentricity of the vortex in the driven disk for a small range of phase differences above 1. While the eccentricity for the vortex in the driven disk shows a dependence on the detuning, the eccentricity of the vortex in the heated disk is independent on the detuning of the driving frequency. Here the eccentricity changes from values below 1 to values above 1. The change from values below one to values above one takes place around a phase difference of 90°. The eccentricity as well as the phase difference are two experimentally accessible values and can be directly compared with the experimental results, discussed in chapter 6.

3 Magnetic Imaging

3.1 Introduction

In the past century a number of methods to image magnetic structures has been developed. This chapter is by no means meant as an overview [78, 79] of this manifold field nor it's recent advances [80, 81]. Instead a brief introduction into the methods, used in the course of this thesis. They are put into the historic context and further their contrast mechanisms, temporal and spatial resolution as well as some experimental requirements are given in more detail for each method. As a remark to this it has to be said, that some of these properties are only applicable to the specific combination of experimental setups and studied materials. They depend on the studied samples e.g. the used materials and dimension and can differ in different experimental setups. Further all of the presented methods are still undergoing rapid advance hence a lot of the given properties might change in the future. The rapid developments in the field of magnetic imaging can be e.g. seen in the historic oldest method to visualize magnetic structures in the following.

Diffraction limit

The Bitter method [82–84] can be seen as beginning of imaging magnetic structures. The technique uses a ferrofluid to decorate the surface to be studied. The magnetic particles disposed in the fluid coalesce on the surface where the magnetic field diverges. Subsequent the surface is viewed in an optical microscope. The development of this method over time is an excellent example why it is so complicated to compare e.g. the resolution and contrast of magnetic imaging methods. First the optical contrast arising from the particle concentration at the

places of largest field gradients was used [82–84]. The resolution is in this case determined by a combination of the size of the magnetic particles, the wavelength of light limiting the viewing of smaller size particles and the quantity of particles on the sample surface being numerous enough to disperse light [85]. Further optical anisotropy may be induced in the ferrofluid. This can produce additional optical contrast owing to the birefringence observed in polarized light [86–89] which can be used to get a reconstruction of a directional map of the stray field pattern. Recently the spatial resolution of this technique was pushed even further due to the development of the Scanning Tunneling Microscope (STM) [85]. An STM was used instead of the optical microscope [85] to overcome the limitation due to the diffraction-limit (eq. (3.1)) [90]:

$$r = f_i \times \frac{\lambda}{NA}. \tag{3.1}$$

With r being the resolution limit, λ the used wave length of the probe (photon, electron....) and NA being the numerical aperture. f_i is a constant depending on the diffraction criterion:

resolution limit	f_i
Rayleigh	0.61
Abbe	0.5
Sparrow	0.47

Subsequent to Bitter, various light-optic magnetic field imaging techniques have been developed, each adding another pixel to the always evolving picture of understanding magnetic structures. The discovery of the Kerr-effect [93] allowed for another technique of visualization of magnetic surface structures. The combination of this technique with the development of pulsed Laser systems led to the time-resolved magneto-optic Kerr-effect (TR-MOKE) microscopy. In this thesis TR-MOKE measurements were performed on spin-waves in a temperature gradient. The measurements were performed in Regensburg in collaboration with Martin Decker and Johannes Stigloher.

To study the magnetization dynamics of coupled magnetic vortex oscillators with predicted movements in the order of a few hundred nanometers section 2.2 high spatial resolution in combination with high temporal resolution is required. To overcome the limited resolution for visible light (VIS) ($\lambda = 390\,\text{nm}$ to $700\,\text{nm}$) due to 3.1 one way is to shorter wavelength λ in the X-ray regime ($\lambda = 0.01\,\text{nm}$ to $10\,\text{nm}$). In combination with using X-ray Magnetic Circular Dichroism section 3.3.1 as contrast mechanism this leads to Scanning transmission X-ray microscopy (STXM) (see section 3.3). The need for circular polarized X-rays at tunable wavelengths to measure XMCD requires the use of synchrotron radiation. Hence the measurements were performed at the MAXYMUS Beamline at Bessy II in Berlin. By

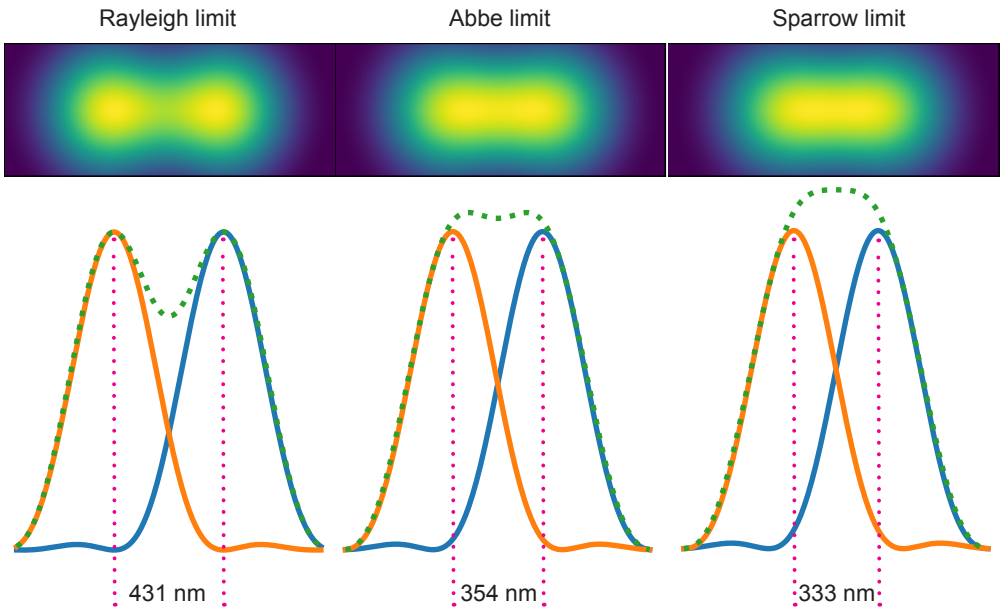

Figure 3.1: Conventional resolution limits due to diffraction illustrated by Airy profiles [91] for 800 nm (Ti:Sapphire Laser) with a numerical aperture of $NA = 1.13$ [92]. Rayleigh: the first minimum of one Airy profile overlaps the maximum of the second Airy profile, with sum of the profiles and the 2D image showing a significant dip. In the Abbe limit the dip is significant smaller and disappears in the Sparrow limit.

synchronising the applied excitation of the magnetization dynamics to the time structure of the photon pulses emitted from the storage ring high temporal resolution can be achieved (section 3.3.2). The results are presented in chapter 6.

The invention of the electron microscope by Ernst Ruska and Max Knoll in 1934 [94] enabled the microscopy of magnetic structures to go beyond the limitation of VIS optical microscopy. Almost 3 decades later the first successful attempts to directly visualize magnetic structures [95–97] by using Transmission electron microscopy TEM (see section 3.2) were made. The Lorentz-TEM (L-TEM) measurements in this thesis on magnetic vortices in static temperature gradients (see chapter 7) were performed in Regensburg in cooperation with Prof. Dr. Josef Zweck, Johannes Wild and Felix Schwarzhuber.

3.2 Lorentz Microscopy

The force F_L acting on a moving electric point charge q with instantaneous velocity v, due to an external electric field $\vec{E}$ and magnetic field $\vec{B}$, is given by:

$$\vec{F_L} = q(\vec{E} + \vec{v} \times \vec{B}). \tag{3.2}$$

Magnetic imaging in TEM is based on the deflection of the electron beam by the magnetic induction in the sample plane. Thus the magnetic induction is detected

rather than the magnetization $\vec{M}$ itself. By neglecting stray fields and internal demagnetization fields $\vec{B}(x,y) \propto \vec{M}(x,y)$ can be assumed in most cases [98]. The angle of deflection β is given by [99]:

$$\beta_L = \frac{e\lambda}{h} \int_{-\infty}^{\infty} B_\perp(x,y)dz, \tag{3.3}$$

with the electron charge $e = 1.6 \times 10^{-19}C$, the electron wavelength λ (see section 3.2.1) the Planck constant h and the magnetic induction of the sample perpendicular to the electron beam $B_\perp(x,y)$. If stray-fields are ignored, for a uniform in-plane magnetized sample of thickness t this expression simplifies to:

$$\beta_L = \frac{e\lambda B_s t}{h}. \tag{3.4}$$

For a 10 nm thick sample with a saturation induction $B_s = \mu_0 M_s = 1\,\mathrm{T}$ the deflection angle is $\beta_L \approx 5 \times 10 \times 10^{-6}\,\mathrm{rad}$. This is about 4 orders of magnitude smaller than the angle of Bragg diffraction commonly seen in normal TEM [100]. A diffraction of this size is experimentally hard to resolve [100]. This can be overcome by considering the electron beam as a propagating wave by a quantum mechanical approach and measuring the phase shifts induced due to the interaction with the magnetic vector potential: $\vec{B} = \nabla \times \vec{A}$. There are many ways to measure this small phase change like Foucault mode [101] or differential phase contrast (DPC) measurements [102]. The most commonly used method though is to use the Fresnel mode [103]. Here the specimen is illuminated with a parallel homogenous electron beam (see section 3.2.1) and contrast changes in over- and under-focus images (see section 3.2.2) are measured.

3.2.1 TRANSMISSION ELECTRON MICROSCOPY

There are two common modes to record an image with a transmission electron microscope (TEM): Conventional transmission electron microscopy (CTEM) and scanning transmission electron microscopy (STEM). While in STEM the electron beam probe is scanned through the sample plane to record a pixel of the total image in serial mode the CTEM mode is very similar to optical microscopy with a conventional light microscope (see fig. 3.2). The image generation is done in two steps. First the sample is illuminated by an as parallel as possible beam (often there is a trade of between a highly coherent parallel beam and brightness [98]) then the magnified image of the transmitted signal is recorded. The electrons are provided by a field emission gun (FEG). They are extracted via an electric field from a pointed cathode tip. Compared to traditional thermal filament emitter the small curvature of the sharp tip is an ideal point like source for high spacial coherence. The acceleration of the emitted electrons is done in a multi stage process in

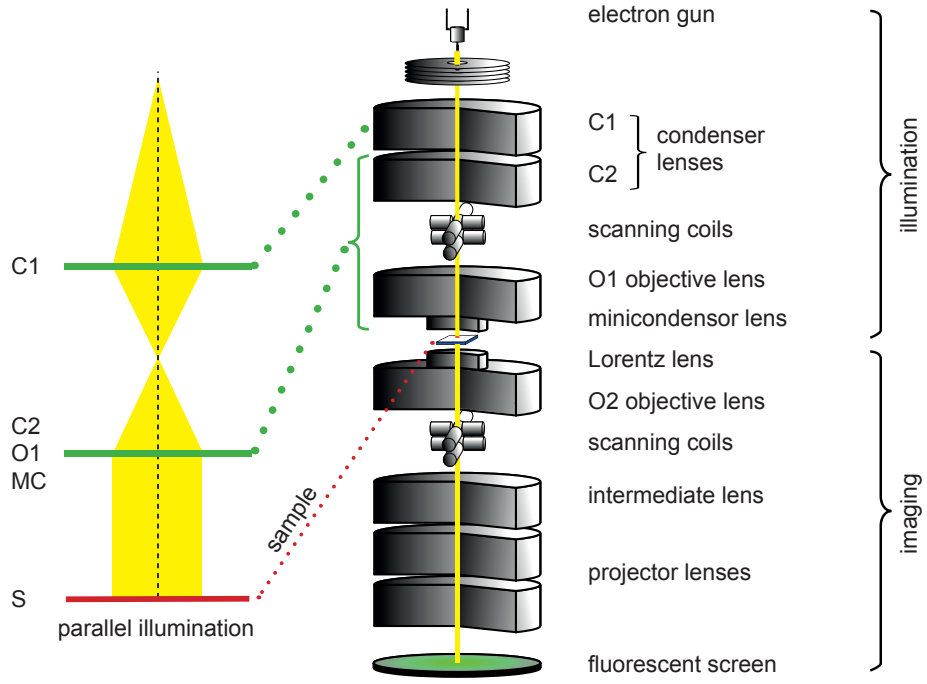

Figure 3.2: Left: Ray path in a TEM for parallel illumination. Right: Schematic of a typical modern TEM.

which the beam is further shaped for optimal imaging. Directly after leaving the FEG the illuminated sample region is defined by the two stage condenser lenses and an aperture. In case of the Tecnai F30 from FEI used in this thesis the electrons are accelerated of up to 300 keV. Their de-Broglie wavelength is related to their momentum through the Planck constant h:

$$\lambda = \frac{h}{m_e v}, \tag{3.5}$$

with the electron mass m_e and the velocity v. Taking highly relativistic effects into account the wavelength for 300 keV is around 1.97 pm. However, the resolution is limited by the lens aberrations rather than the diffraction limit. Since the electromagnetic and electrostatic lenses used for beam shaping have poor imaging qualities compared to optical lenses [104] astigmatism and aberration for most lenses have to be compensated for. In case of the Tecnai F30 this is done for the condenser lenses and the objective lenses. By using state of the art spherical and chromatically aberration correction 50 pm a resolution of up to 50 pm can be achieved [105]. For L-TEM imaging high kinetic energy is needed for sufficient beam penetration through the sample (typically metals of up to 200 nm thickness), the resolution is typically limited by the small interaction between the magnetic induction in the specimen and the passing electrons (see section 3.2.2). After

passing through the sample several lenses follow which magnify the CTEM image further.

3.2.2 The magnetic specimen phase object

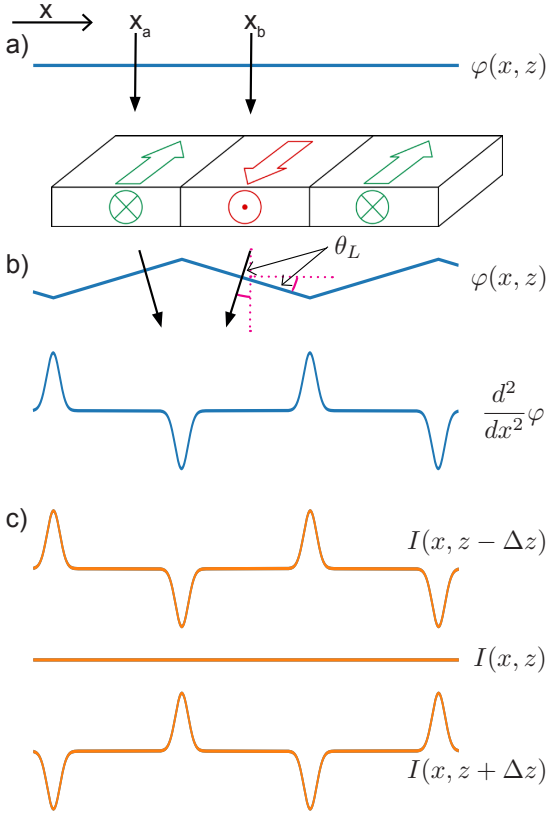

Figure 3.3: Schematic diagram of the electron beam deflection and wave-front curvature due to scattering by a magnetic specimen a) original front b) wave front and phase after magnetic sample c) Intensity in over ($+\Delta z$) and under-focus ($-\Delta z$).

The specimen's transmission function $T(\vec{r})$ can be described by an absorption part $U(\vec{r})$ and a phase shift $\varphi(\vec{r})$ [106]:

$$T(\vec{r}) = U(\vec{r}) \times e^{i\varphi(\vec{r})}. \tag{3.6}$$

For thin samples the absorption can be neglected. Further for demonstration purposes here the 2D phase-shift $\varphi(\vec{r}) = \varphi(x, y)$ is reduced to a 1D problem $\varphi(x)$ (see fig. 3.3). The phase shift between the two beams at $x = x_a$ and $x = x_b$ can be described as:

$$\varphi = \frac{2}{\hbar} \int_{-\infty}^{\infty} \int_{x_a}^{x_b} B_{\perp}(x) \times dz \times dx. \tag{3.7}$$

$\int B_{\perp}$ can be attributed to the collected phase shift along the electron trajectories. Equation (3.7) basically describes the total flux contained within a rectangular section of the specimen confined by $dx \times dz$. The wavefront after passing the specimen is at the same angle β_L to the incident beam as the deflected beam in the classical Lorentz angle determined by geometry considerations before (see fig. 3.3). Using wave-propagation the intensity at a given defocus Δz can be expressed by:

$$I(x, \Delta z) = 1 - \frac{\Delta z \times \lambda}{2\pi} \frac{d^2}{dx^2} \varphi(x, y). \tag{3.8}$$

Thus, in Fresnel imaging it is the change of the magnetic induction which is imaged rather than the induction itself. Domain walls appear as bright or dark lines, depending on the relative alteration of the magnetization in the two adjacent domains (see fig. 3.3). By changing the defocus from positive to negative values

the contrast is also inverted. For $\Delta z = 0$ (in-focus) the contrast vanishes. In case of a magnetic vortex core the same principle applies. Due to eq. (3.7) only the change in the in-plane curling magnetization of the outer part produces a contrast in the middle of the vortex core. Depending on the vortex chirality this contrast appears as a dark or bright spot [98]. In fig. 3.4 a focus series is shown. The focus is varied from $\Delta z = -50\,\mu\text{m}$ to $\Delta z = 40\,\mu\text{m}$. As can be seen the vortex core contrast changes from a bright spot for $\Delta z < 0\,\mu\text{m}$ to a dark spot for $\Delta z > 0\,\mu\text{m}$. In focus ($\Delta z = 0\,\mu\text{m}$) no contrast is visible.

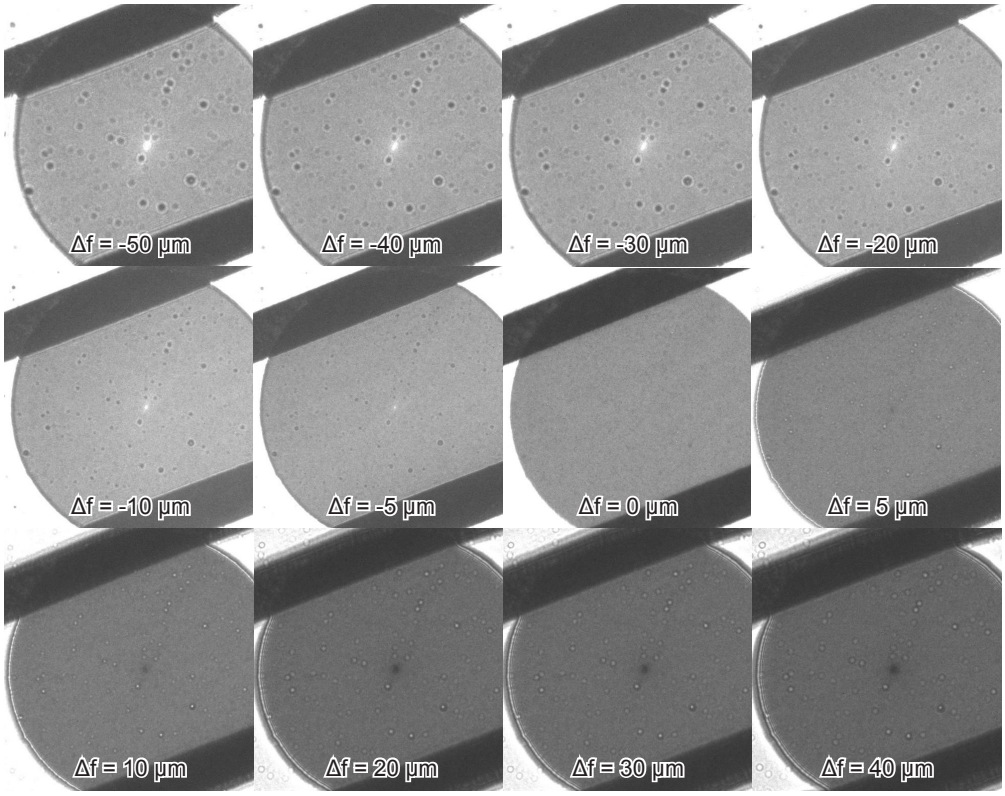

Figure 3.4: L-TEM focus series of a Py disk with a diameter of $d = 2\,\mu\text{m}$ and a thickness of $t = 20\,\text{nm}$ in vortex ground state. The focus is varied from $\Delta z = -50\,\mu\text{m}$ to $40\,\mu\text{m}$. The contrast associated with the in plane curling depends on the defocus. For $\Delta z < 0\,\mu\text{m}$ white, for $\Delta z > 0\,\mu\text{m}$ black, in-focus the contrast disappears.

It is also possible to reconstruct the phase and thus the magnetic induction from a series of such defocused images by solving the transport of intensity (TIE) equation [107] that can be written in Poisson form:

$$\nabla^2 \Phi(x, y) = -\frac{2\pi}{\lambda} \frac{\partial}{\partial z} I(x, y, z), \tag{3.9}$$

with the substitution $\nabla\Phi(x, y, z) = I(x, y, z)\nabla\varphi(x, y)$. This can be solved numerically e.g. fast Fourier transformations allowing for quantitive measurements of the magnetic induction (see fig. 3.5). As part of this thesis various TIE reconstructions for magnetic vortex cores and skyrmions have been performed [108–110] and

have been compared to DPC measurements. Further the reconstruction has been extended to higher order reconstructions [111] and benchmarking them against analytical and numerical simulations allowing a precise measurement of the vortex core size. This work is currently in the process of publishing. The focus in the current work is on the movement of the vortex core position. Hence the measurements here have been performed in normal Fresnel mode with typical defocus lengths of 10 µm to 15 µm.

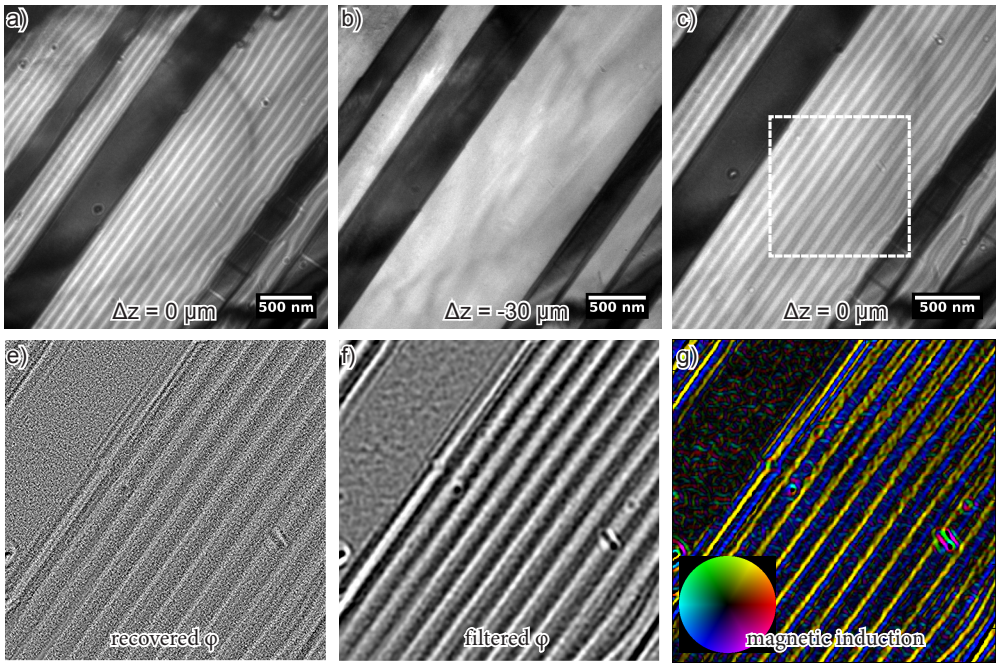

Figure 3.5: Example of TIE-phase retrival for the helical phase in $Mn_{1.4}PtSn$. (a) shows the under-focused image, (b) the focused and (c) the over-focused image. The retrived phase is shown in (d) and smoothed with a bandpass-filter (e) to reconstruct the magnetic induction (f).

3.3 STXM

As described in section 3.2 one way to overcome the diffraction limit (eq. (3.1)) for VIS light is to use high energy electrons in TEM. To image the magnetization dynamics in magnetic vortex core oscillator networks (see chapter 6) high temporal resolution is required. Recently, there have been some approaches to incorporate fs time resolution in TEM [112] by creating ultrashort highly coherent electron pulses by illuminating the FEG with an pulsed laser system. This new method seems very promising for investigation magnetization dynamics at the *nm*-scale with high temporal resolution without the need for synchrotron radiation.

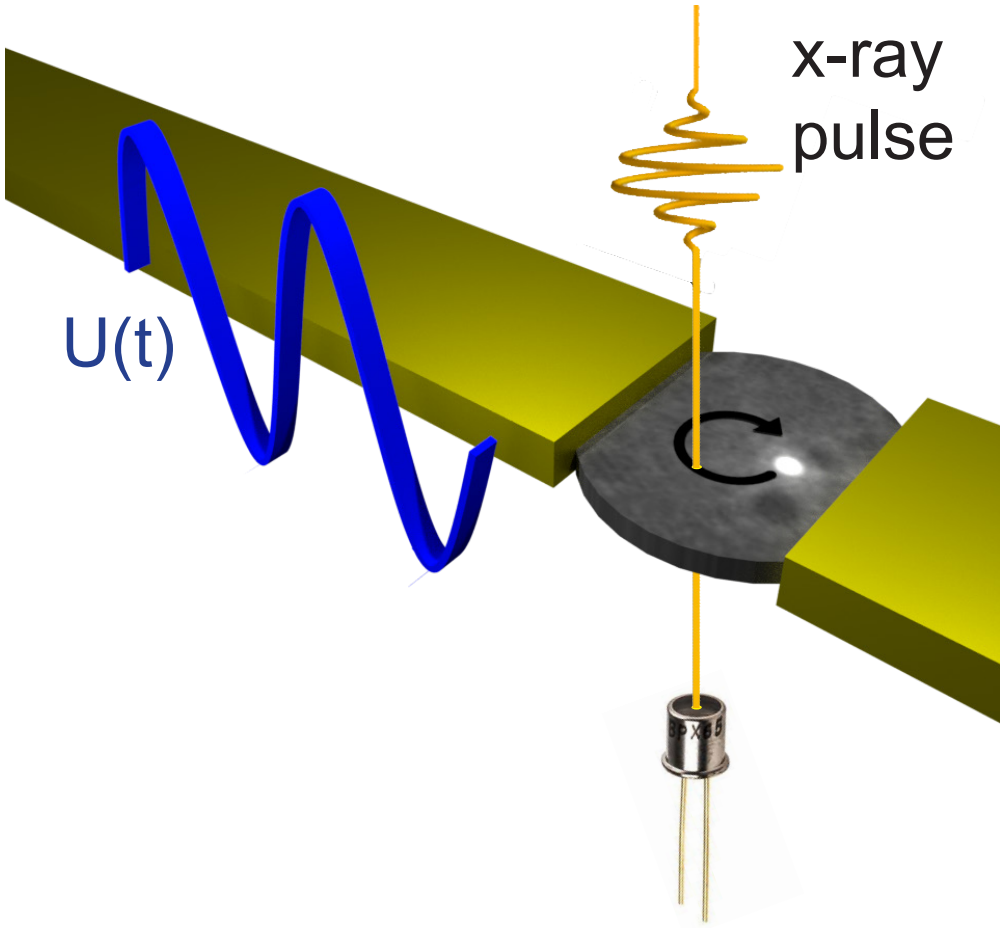

Figure 3.6: Sketch of the experimental setup. The transmitted X-ray intensity is modulated by the XMCD effect which is proportional to the magnetization component projected onto the beam direction. For vortex dynamics the X-rays enter the specimen perpendicular to the sample plane. The focussed beam is scanned across the sample. Time resolution is achieved by a pump - probe type approach by synchronizing the STT-excitation of the magnetization dynamics with the electron bunch creating the X-ray pulses.

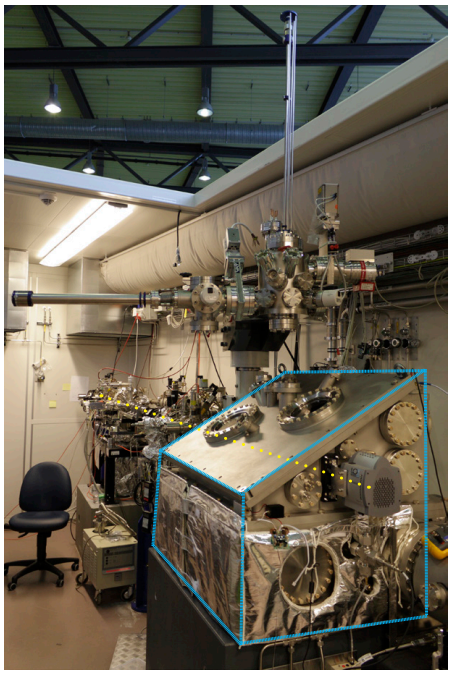

Figure 3.7: STXM Microscope in UHV-chamber (blue) at MAXYMUS Beam-line at BESSY II.

Here the magnetization dynamics were investigated by Scanning transmission X-ray microscopy (STXM). Instead of overcoming eq. (3.1) by using high energy electrons the spatial resolution is increased by using shorter wavelength X-rays. The magnetic contrast is achieved by harnessing X-ray magnetic circular dichroism (see section 3.3.1). For experiments on magnetic vortex core dynamics a polar configuration is used to image the out of plane magnetization of the vortex core. The transmitted X-ray intensity is modulated by the XMCD effect which is proportional to the out of plane magnetization. So in this case the core itself is imaged and not the surrounding curling magnetization hence a dark or bright contrast determines the polarity of the vortex core. The contrast can be inverted by changing the circularity of the X-ray beam.

The X-ray beam is focused on the sample (see fig. 3.6) and scanned across the region of interest to generate an image. The wavelength for the L_3-edge of nickel at an energy of 851 eV is $\lambda = 1.46\,\text{nm}$. The spatial resolution in this case is determined by the focussing of the x-ray beams. This is done by Zone Plates [113] and determines the numerical aperture. At the MAXYMUS beamline at Bessy II a typical resolution of 20 nm can be achieved [113]. STXM not only offers an increase in lateral resolution by using soft X-rays, but also the inherent pulsed time structure of synchrotron radiation sources makes time dependent magnetic studies feasible by using a pump probe approach in combination with the excitation of the magnetization dynamics (see section 3.3.2). The time resolution depends on the temporal bunch-width of the synchrotron and is 10 ps to 35 ps.

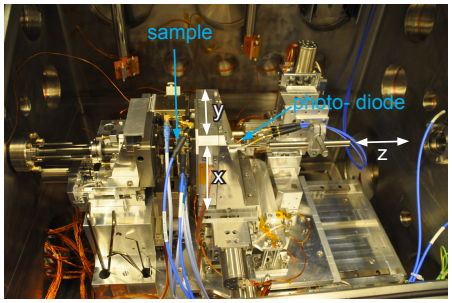

Figure 3.8: STXM Microscope UHV-chamber opened. The sample and the Photodetector are placed on a 3-axis dual stepper- and piezzo-stage for focussing and scanning.

3.3.1 XMCD-Effect

Lambert-Beer law

Analogue to visible light the change of the intensity $\frac{dI}{dz}$ compared to the initial intensity I_0 of X-ray radiation passing through a sample in z-direction is antiproportional to the distance passed z. This leads to a simple first-order linear ordinary differential equation ODE:

$$\frac{dI}{dz}(z) = -\mu(E)I(z) \Rightarrow I(z) = I_0 e^{-\mu(E)d}, \tag{3.10}$$

where $\mu(E)$ is the material dependent photo-absorption coefficient, that also depends on the photon energy $E = \hbar\omega$. This relation is also known as Lambert-Beer law. In case of energies below 20 keV, which is applicable to the experiments in the present work, the photo-effect is the dominant absorption mechanism between the X-ray photons and the electrons in the sample. Thus the photo-absorption coefficient itself can be related to the energy dependent absorption cross section σ_{tot} [114, 115]:

$$\mu(E) = \sum_j w_i \cdot \sigma_{tot,j}(E) \cdot \rho_j. \tag{3.11}$$

For a real target $\mu(E)$ is the summation over all elements j with their individual properties: w_j being the fraction weight and the density ρ_j . In the energy range of a few hundered-electron-volts up to some tens of kilo-electron-volts, in which the experiments of the present work were carried out, the dominant process when a photon of energy E is absorbed is the excitation of an electron in a core shell of energy E_i in its initial state $|i>$ to a final state $|f>$ with energy $E_f = E_i + E$ and the final states density $\rho(E_f)$. Thus the absorption cross section σ_i is given as the probability for this excitation $\Gamma_{i\to f}$ per time divided by the photon flux:

$$\sigma_i(E) = \frac{\Gamma_{i\to f}}{I_{ph}}. \tag{3.12}$$

The photon flux I_{Ph} being the number of photons striking a surface is related to the intensity: $I = \frac{I_{Ph}E}{\lambda}$.

Fermi's golden rule

Following Fermi's golden rule, the one electron absorption cross section can be described as [114, 116]

$$\Gamma_{i\to f} = \frac{2\pi}{\hbar}| < M_{fi} > |^2 \delta(E_f - E_i - E), \tag{3.13}$$

with $< M_{fi} >$ being the matrix element $< f|H'|i >$ of the perturbation H' between the final and initial states. In combination with first order perturbation theory

the absorption coefficient can be expressed as [81, 117]:

$$\mu(E) \propto \sum_f | < f|\mathbf{p} \cdot \mathbf{A}|i > |^2 \delta(E_f - E_i - E) = | < M_{fi} > |^2 \rho(E), \qquad (3.14)$$

with momentum operator $\mathbf{p}$ and $\mathbf{A}$ being the vector potential of the incident electromagnetic field and $\rho(E)$ being the density of states for the final states $|f >$.

In X-ray absorption the atom absorbs a photon giving rise to the transition of a core electron to an empty state above the Fermi energy (see fig. 3.9 (a)). This transition has to obey the selection $\Delta m_l = 1$ for right circular polarized light and $\Delta m_l = -1$ for left circular polarized light for reasons of angular momentum conservation. This restriction in combination with the fact that $\mu(E)$ is proportional to $\rho(E)$ this gives rise to the XMCD effect hence $\mu(E)$ is different for right or left circular polarized X-rays depending on the magnetization. This difference in the X-ray absorption spectra (XAS) is shown in fig. 3.9 (b) for the Nickel L_3-edge. This contrast allows for absorption contrast of up to 20% in the case of Ni (see fig. 3.9 (b)).

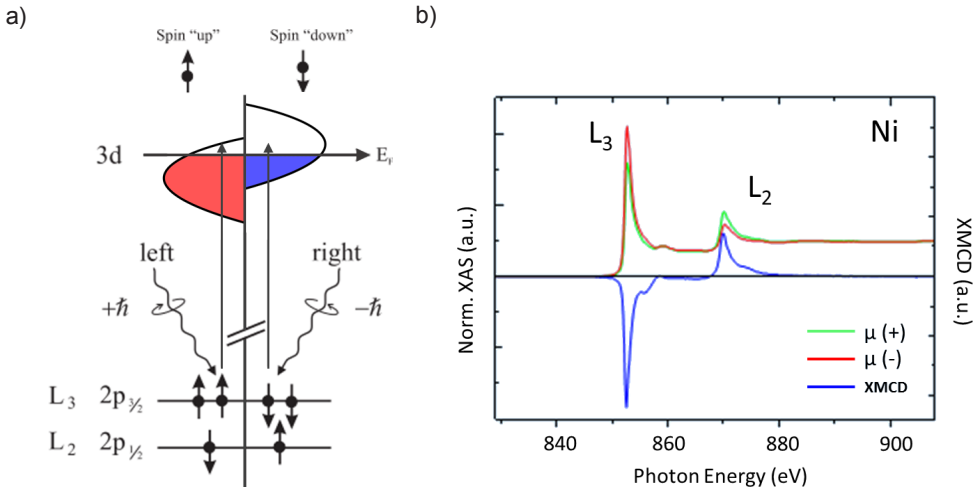

Figure 3.9: (a) Pictorial description for the absorption process causing XMCD at the $L_{2,3}$ edge for 3d transition metals for left and right circularly polarized X-rays (b) XAS and XMCD spectra of Ni. $\mu(+)$ for right and $\mu(+)$ for left circularly polarized X-rays. Taken from [118].

3.3.2 STXM Time Resolution

Since the electrons traveling through the storage ring are not distributed uniformly but are traveling in bunches, evenly spaced along the ring, the emitted X-ray radiation used for the STXM measurements is not a continuous but a pulsed X-ray emitter. The distance between these bunches at BESSY II is 60 cm which is an exact fraction of the storage ring itself. The frequency of these X-ray pulses is:

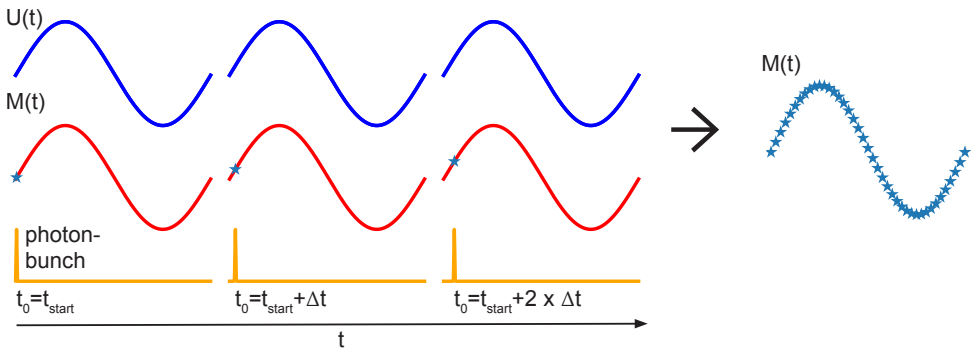

Figure 3.10: Synchronization of the electrical excitation (via STT) pump (blue) to the optical probe of the X-ray bunches emitted by the synchrotron (orange) at 500 Mhz allow for stroboscopic measurements of the magnetization dynamics (blue).

$$f = \frac{c}{60\,\mathrm{cm}} \approx 499.654\,\mathrm{MHz}. \tag{3.15}$$

By synchronising the "pump" electronic excitation of the magnetization dynamics to the "probe" x-ray pulses (see fig. 3.10) by delaying the electronic (here via STT) excitation relative to the x-ray flashes time resolved imaging can be achieved. Single Photon detection allows for multi-channel acquisition, which can be performed in standard multi-bunch operation mode of the synchrotron. The time resolution itself depends on the stability of the synchronisation and the temporal pulse width of the probe pulses. The synchronisation is usually not the limiting factor since modern integrated electronics allow the usage of FPGA running at operating frequency 10-100 times the storage ring frequency. The temporal bunch width depends on the operation mode of the storage ring and varies from 10 ps to 35 ps limiting the temporal resolution.

4 Sample Preparation

This chapter presents various methods and materials for preparing the samples used in this work. Theoretical modeling and defined geometries are the foundation for the results presented in this work. As discussed in chapter 2 and chapter 5 the exact design of the temperature landscape with respect to the magnetization dynamics is critical for the observation of the presented results. Hence nanofabrication is an essential part of the work presented. The sample fabrication consists of two main steps: Lithography and thin film deposition. This chapter gives an overview of the involved methods and parameters. Some of the sample preparation information in this chapter goes beyond the experiments discussed in this thesis and focuses on further collaborations. The entire Lithography and most of the thin film deposition are performed in the facilities at the University of Regensburg.

4.1 Materials

Permalloy (Py) $Ni_{80}Fe_{20}$ is one of the standard workhorses in the field of materials used for investigating magnetization dynamics. For experiments involving local heating it's high Curie Temperature ($T_C = 872\,\mathrm{K}$) [119] in the fcc phase makes it an excellent choice to study spin-caloric effects [120–122]. It's relatively high Saturation Magnetization $M_S = 8 \cdot 10 \times 10^5\,\mathrm{A/m}$ [123] and low coercivity [123] make it an ideal material to study magnetization dynamics and domain wall movement [124]. In case of numeric calculations the lack of significant crystalline anisotropies are helpful. A typical exchange parameter for simulations of Py is $A = 1.3$ [125]. The significant anisotropic magnetoresistance makes electrical mea-

surements of the magnetization state possible [15]. Combined with many robust film thin deposition methods Py is an obvious choice for the work presented here. Especially, if considering the experimental challenges involved with local heating nanoscale structures on fragile SiN-membranes a robust choice of materials is important. However, there is a wide range of materials with different properties that are interesting candidates for further investigations.

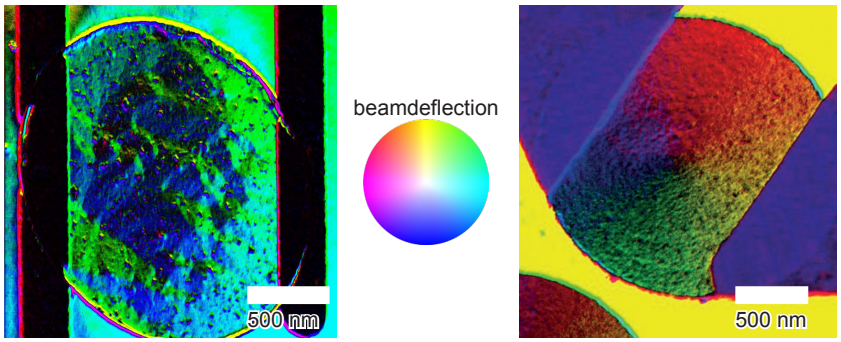

Figure 4.1: TEM - DPC measurement of different ferromagnetic materials deposited on 50 nm SiN-membranes. a) 30 nm Co_2MnSi full film sputtered, negative edged. b) 50 nm Py sputtered, positive lift-off.

For experiments involving spin torques created by high temperature gradients and their interaction with the magnetic domain structure any soft magnetic material with a high spin polarization at the fermi edge is of interest. Hence one promising candidate class are half-metals [126]. Per definition a half-metal is a conducting material to electron of one spin orientation and an insulator or semiconductor for those of the opposite direction hence having a spin-polarization of theoretical 100% for the conducting electrons. Many of the known half-metals are Heusler alloys [126]. A prominent candidate to study thermal driven influence on the magnetic domain structure is Co_2MnSi with a high spin-polarization [126] and low coercivity [127]. Since Co_2MnSi can also be sputtered on many different substrates such as MgO, $SrTiO_3$, Si and SiO_3, it might be a possible candidate to try on SiN-membranes. Unfortunately, our efforts so far were not successful to harness this material for transmission magnetization dynamics experiments. The thin films were sputtered at the University of Bielefeld in the group of Dieter Reiss at 400 °C substrate temperature and prepared in a similar manner as on Si bulk substrates. Most likely due to the high defect rate in the SiN-membranes the magnetic domain configuration in the full-films as well as the structured (via ion-etching) disks were defined by small multi-domains pinned to the defects (see fig. 4.1) and hence not usable here. The use of the SiN-membranes hence significantly narrows the choice of materials.

4.1.1 The SiN-membrane platform

The experiments presented in this work all require well defined controllable lateral temperature distribution across the sample plane (see chapter 5). One way to realize this experimentally is to reduce the general 3D problem of heat-dissipation to a quasi 2D problem by elimination of one dimension. The SiN-membranes used here have a thickness of 30 nm to 50 nm. This is at least 2 orders of magnitude lower than the relevant dimensions in the x-y-plane. Combined with the low thermal conductivity of SiN [128] compared to other materials, mainly being metals, this allows for a controlled thermal environment [128, 129]. In case of the measurements on vortex core movement by pure thermomagnonic torques hight temperature gradients are needed (see section 2.3). In this case the membrane frame can be used as a heatsink (see section 5.2) due to being infinite thick (200 µm) compared to the membrane as shown in fig. 4.2.
In addition to this, the membranes are also a necessity for the transmission measurements performed in the course of this thesis (STXM and L-TEM). As seen in fig. 4.3(a) the quality of the SiN-membranes is of overall poor quality compared to bulk substrates. The number and size of defects varies greatly from supplier to supplier and also depends on the individual processed batch as shown in fig. 4.3. This makes beforehand screening of each membrane necessary. The overall roughness and defects of the SiN-membranes can cause magnetic pinning centers influencing the movability for film thicknesses below 30 nm (see fig. 2.5).

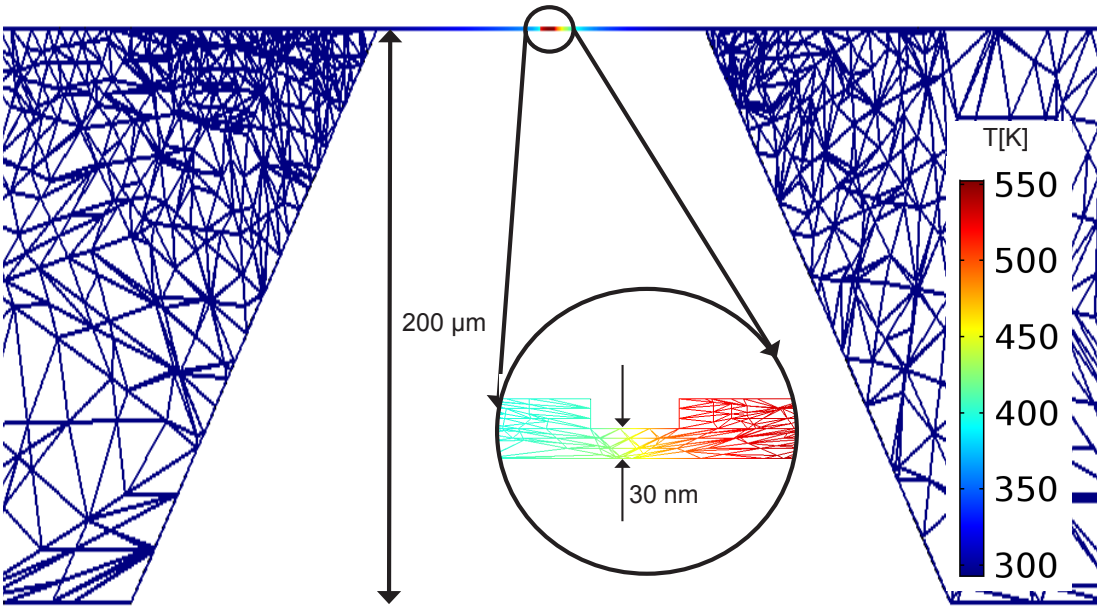

Figure 4.2: Wireframe model from FEM-Simulation (see chapter 5). The membrane frame has a thickness of 200 µm and tapers to a 30 nm thick suspended membrane in the middle which is about the same thickness as the two Py disks structured on top.

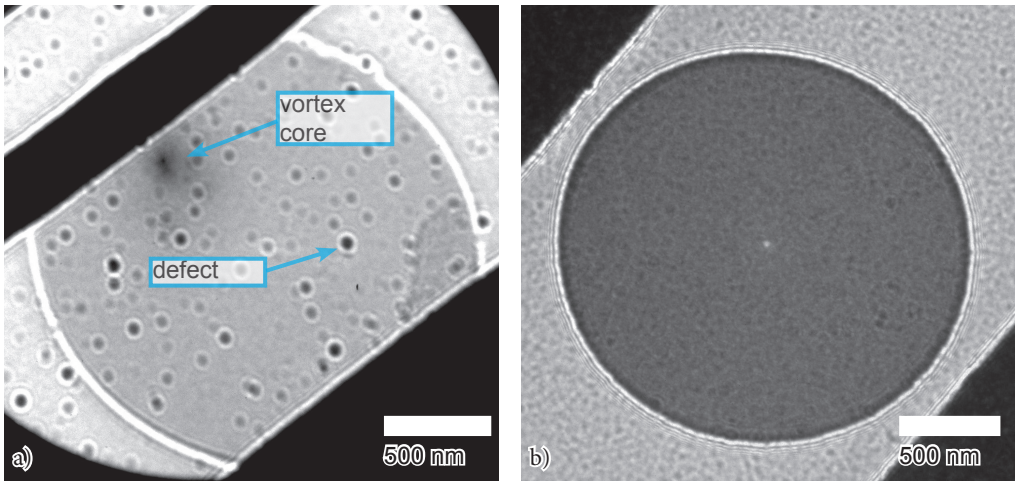

Figure 4.3: L-TEM measurement at similar defoci of two different samples prepared on 30 nm thick SiN-membranes from different suppliers. The Py thickness in both cases is 20 nm. The vortex core chirality is reversed thus the contrast relative to the background changes. a) The sample is prepared on a membrane form Silson, the vortex core is pinned in the upper left corner of the vortex disk. The dark sports in the Py disk are defects embedded in the membrane. Due to the defocussing of the objective lens the defects appear slightly larger. b) The second sample was prepared on a membrane from spi supplies. The overall number and size of defects is significant less. The vortex core is in the middle of the Py disk at the expected ground state position.

4.2 Litography

4.2.1 Electron-beam lithography

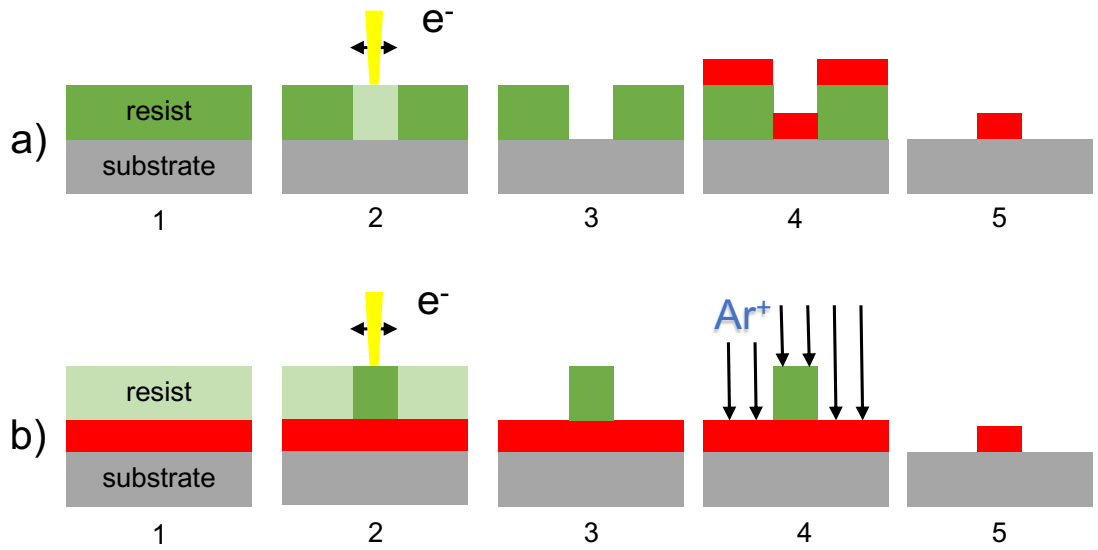

Figure 4.4: EBL process a) positive mask resist (e.g. PMMA) process steps: 1) resist coating 2) e-beam exposure 3) development in solvent 4) thin film deposition 5) lift-off b) negative tone resist 1) resist coating 2) e-beam exposure 3) development in solvent 4) etching 5) lift-off.

Electron-beam lithography (EBL) is the practice of writing patterns in thin films of electron sensitive materials (resist) with a focused electron beam [127]. With the ability to pattern high resolution 2D structures with arbitrary shapes down to the nanometer scale [130, 131] it is one of the most widely used and versatile methods of thin film sample structuring. A sketch of the overall process for positive mask e-beam resist can be found in fig. 4.4 a. Most of the sample preparation was done with a positive tone e-beam resist in the following steps.

1) Resist coating

Especially for structuring on SiN-membranes the choice of the right resist is critical. Due to the fact that the membranes can not be exposed to ultrasonic vibrations while being submerged in solvent, lift-off can be critical. Here a bi-layer resist was chosen:

Layer	Resist
lower layer	PMMA 50K
upper layer	PMMA 950K

Poly(methyl methacrylate) (PMMA) is a long chain polymer often used as a standard positive e-beam resist. The 50-950K indicate the molecular weight and thus the length of the methyl methacrylate chains. As positive resist it undergoes

a conversion from low to high solubility upon exposure to electrons by fission of the molecular chains. In general the solubility becomes much higher the shorter the molecule chains become [132]. Thus by choosing a longer chain length on-top a shorter one, an undercut effect during development can be achieved to benefit easier lift-off. The layer thickness of the resist, being critical for easy lift-off, mainly depends on the percentage of solved PMMA in anisol, the timing and rotation settings during spin-off and additional the substrate roughness. Thus should be determined individually for different batches of membranes. As an indicator for SiN-membranes the following thicknesses of the resist were observed by AFM measurements:

resist	thickness [nm]
PMMA 50K 6%	230
PMM 50K 2%	150

The spin coating process was carried out as:

1	deposit a few drops of the resist on the sample mounted on the spin-coater
2	spin for 5 s at 3000 rpm
3	spin for 30 s at 8000 rpm
4	bake sample for a min of 10 min at 150 °C

2) E-beam exposure

To precisely locally expose the resist good focusing is key. However, even with a very well focused beam electron scattering in the resist and substrate lead to undesired influences exposing the adjacent regions next to the focus of the beam [132] (see fig. 4.5).

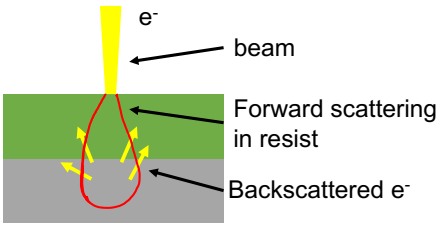

Figure 4.5: Proximity effect due to backscattered and secondary electrons.

This proximity effect process is strongly depending on the acceleration voltage U_{ex} and the substrate material. Depending on the acceleration voltage the lack of material in the region of the membrane window can produce significantly less scattered electrons compared to the membrane frame. This can easily be visualised by taking a SEM image with the secondary electron detector (SE2) of the final sample at different U_{ex} (see fig. 4.6).

Here a 30 nm thick SiN-membrane with 50 nm of Py structured on top was imaged with the SE2 at different acceleration voltages. For $U_{ex} = 5\,\text{kV}$ the measurement is relatively surface sensitive and the membrane barely visible. At $U_{ex} = 25\,\text{kV}$ the membrane window is clearly visible due to a lack of backscattered electrons in

the missing material compared to the frame. While structuring fine elements and sharp edges with the electron beam in an EBL process this effect has to be compensated by varying the relative dose:

location	dose $[\mu C/cm^2]$
on frame	400
on window	600

Of course these values are only average values. Many factors such as feature size of the structure to be written, scanning resolution, the inevitable exposure during alignment and many more factors have to be considered. In some cases this might vary but the values above should be a good starting point. For fine structures a dose test is inevitable. As already mentioned they depend on U_{ex} and also the intensity distribution inside the focus spot of the electron beam and thus on the used aperture. For most structures in this work the following settings were used:

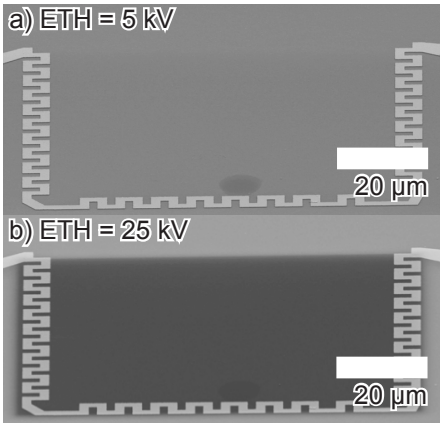

Figure 4.6: SEM image of a 30 nm thick SiN-membrane with a 50 nm Py film on-top. a) taken at $U_{ex} = 5$ kV b) taken at $U_{ex} = 25$ kV at similar contrast settings.

accelerating voltage	25 kV
aperture	20 µm
working distance	7-10 mm

3) Development

The parts of the resist exposed to the electron beam can be subsequently removed using a suitable solvent solution. For developing exposed PMMA a solvent of methyl-isobuthyl-ketone (MIBK) and 2-propanol (IPA) is a common choice. The interdependence of exposure and development conditions is not trivial [133–135] and the tuneable parameters are numerous (ratio of IPA to MIBK, temperature, development time...). For the samples presented here a ratio of 1:3 MIBK to IPA was used and the development performed as follows:

1	dipping the exposed sample in 1:3 MIBK to IPA for 15s
2	rinsing sample in pure IPA for 30s
3	dry sample with nitrogen

The rinsing is necessary to stop the development of the sample due to the MIBK, prolonged rinsing can increase the undercut in bi-layer resists as used here.

4) & 5) Deposition and Lift-Off

The developed sample is ready for deposition of the desired material (see section 4.2.2). After deposition the substrate is submerged in acetone for at least a few hours (preferably over night) at 60 °C. By this the remaining developed resist is dissolved and the deposited material on top looses footing.

Negative Tone Resist

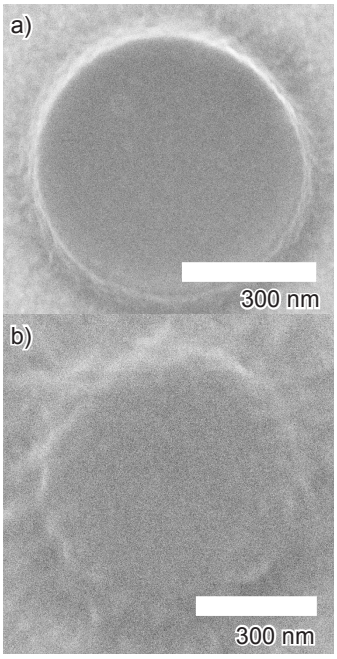

Figure 4.7: SEM image of Py/CoFe/Py - nanopiler prepared via (a) PMMA - cross linking (b) ma-N 2400 negative tone resist.

For negative tone resists the process steps are also shown in fig. 4.4. The steps are similar as for negative tone resist despite negative resist undergoes a change from high to low solubility upon exposure to electrons by cross-linking. The resist used here is ma-N 2400 [136]. After exposure and development the sample was exposed to an ion etching process to remove the previously deposited full-film. The ion etching for structuring with this resist on SiN-membranes turned out with pretty poor results. The reason for this is the short distance between the sample and the filament during the ion etching process, leading to a significant temperature increase inside the membrane window. It is also possible to use PMMA as a negative tone resist via cross-linking at higher resolutions of up to 10 nm [133]. Since negative tone resist was not needed for direct electric connection and the remaining height off cross-linked PMMA can be controlled very well, even allowing bridges and steps [137], PMMA-cross linking was the preferred method over the use of negative tone resist producing higher quality results (see fig. 4.7).

4.2.2 Metal Deposition Methods

The materials of the samples in this work are composed of a metallic stack grown on the 30 nm SiN-membrane. The Py $Ni_{80}Fe20$) disks are grown directly on the SiN and are capped by 3 nm of aluminium (Al). The contacts and heaters are composed of gold (Au) grown on top of chromium (Cr) as bonding agent. The films are deposited by thermal physical vapour deposition (PVD). The deposition is performed by a base pressure of 10^{-8} mbar. Film-thickness is indirectly monitored by a crystal oscillator during growth and checked via atomic force microscopy (AFM) measurements.

4.2.3 Sample fabrication: Coupled Vortices

The samples for the vortex dynamics measurements (see chapter 6) are prepared in a simple three step process (see fig. 4.8). First alignment Au markers are structured on the membrane (thickness $\approx$ 30 nm to centre the pair of Py disks (thickness 50 nm in a second step. In a last step the oscillators are contacted with Au contacts (thickness 100 nm). The last step is done at two different apertures to minimize EBL times. All process but the large orange marked contacts (see fig. 4.8 (c)) in the last step are written with a 20 µm aperture. The large contacts for bonding the sample (see fig. 4.9) are written with a 300 µm aperture.

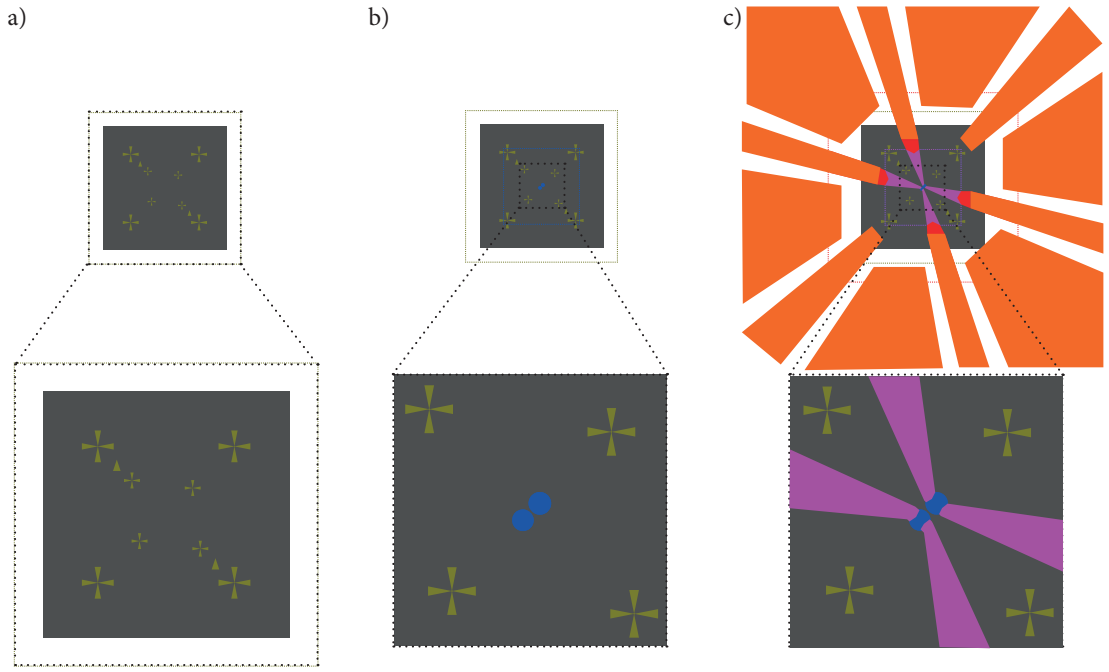

Figure 4.8: Lithography process: (a) alignment markers (Cr/Au) are deposited on the membrane (b) the two Py disks are structured in the centre (c) the Py disks are contacted with high frequency Cr/Au contacts.

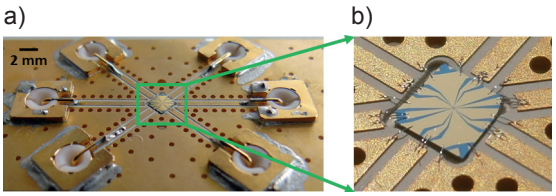

Figure 4.9: STXM sample holder with six high frequency contacts from [138].

Due to the sample holder design for the MAXYMUS Beamline (see fig. 4.9 (a)) the entire sample design is rotated by a 45° angle. The samples are prepared on 30 nm thick SiN-membranes necessary for the STXM measurements and selectively heating a single disk while exciting the other disk with STT current pulses (see section 5.3). The results of the time resolved STXM measurements can be found in chapter 6.

4.2.4 Sample fabrication: Thermal Magnon STT

The samples for the experiments focused on thermal magnon driven vortex core motion (see chapter 7) are prepared in a similar way to section 4.2.3. The structuring is done in a three step process. In a first step (see fig. 4.10(a)) alignment crosses are written in combination with the 2 meander heaters and evaporated (30 nm Au on 5 nm Cr). The lateral dimensions of the membranes are determined beforehand for optimal placement of the heaters near to the edge to maximize the temperature gradients (see section 5.2). The alignment is done relative to the membrane corners. To minimize shifts, additional alignment markers are placed symmetric to each heater. In a second step the Py elements are prepared (see fig. 4.10(b)). The disks have a radius of $r = 1\,\mu m$ and a thickness of $t = 20\,nm$. This specific size is chosen to find a good compromise between maximum movability of the vortex core (section 2.4) and adequate temperature gradients (see section 5.2). The Py disks are capped by 3 nm Al. Additional Py elements are placed for focussing and imaging optimisation as well as additional indicators for remaining in plane fields. In the last step (see fig. 4.10(c)) the contacts are written similar to step 3 in section 4.2.3. In some cases a few Py disks are also contacted for resistance measurements, temperature calibration and being able to ensure both sides of the Py disk being at the same electrical potential. Due to the Seebeck effect a charge current in the Py disk is created. This charge current interacts with the vortex core via STT (see "charge STT" in section 2.4). In thermal equilibrium this charge current could be compensated by induced charges building up on both sides of the Py disk. This can be compensated by shorting both sides instead of leaving the Py element electrical isolated on the membrane. Since theoretical predictions show that the effect of this charge current driven STT can be neglected here (see fig. 2.17(a)-(d)), these contacts were left out in later samples. The experimental results for these samples can be found in chapter 7.

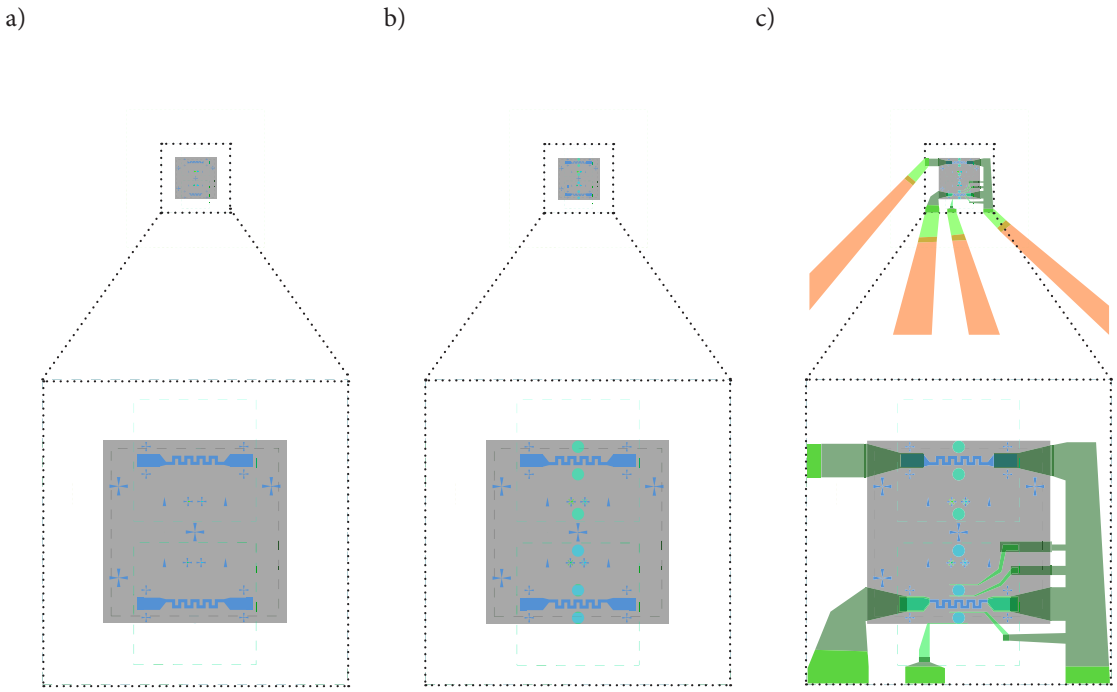

Figure 4.10: Lithography process: (a) Alignment markers (30 nm Au on 5 nm Cr) are deposited on the membrane together with the meander heaters. The lateral dimensions of the membranes are determined beforehand for optimal placement of the heaters near to the edge. (b) The two Py disks 20 nm capped with 3 nm Al are placed between the membrane edge and the meander heater. Additional Py elements are placed for focussing, image optimization, and as indicators for remaining in plane magnetic fields due to the TEM lenses. (c) 130 nm Au on 5 nm Cr contacts are prepared for electrical connection to the meander heater.

5

Designing the 2D temperature landscape

5.1 Thermal modelling (COMSOL)

To model the temperature distribution in the sample designs 3D finite element methods (FEM) simulations using the COMSOL software package were performed. This package solves the general heat transfer equation based on the general energy balance:

$$\nabla \cdot (-k\nabla T) = Q - \rho C_p \frac{\partial T}{\partial t}, \tag{5.1}$$

where ρ is the density of the material and k the thermal conductivity. In case of stationary problems eq. (5.1) simplifies due to $\frac{\partial T}{\partial t} = 0$. This is the case for the two experiments presented here. In both cases the samples are heated locally via Joule heating applying a constant voltage U_{heat} to a heating element structured on the sample. The applied heating power Q can be described as:

$$Q = \frac{U_{heat}}{R(T)}. \tag{5.2}$$

In the temperature range relevant for the experiments the temperature dependence of R can be described by the linear equation:

$$R = R_0[1 + \alpha(T - T_0)], \tag{5.3}$$

with the temperature coefficient α. The values for the parameters used can be found in section 9.1.1.

In 3D FEM the discretezation or meshing of the geometry, on which eq. (5.1) is solved, is critical. Especially if the size of domains varies by four order of

magnitude (see fig. 4.2). Hence the mesh used to evaluate eq. (5.1) was generated adaptively to the geometry with a minimum feature size of 10 nm in x and y direction (see fig. 5.1(a)). Since the temperature changes in z direction are of less interest, the resolution is set to adapt from 10 nm in the region of the heater to single domain on the membrane frame (see fig. 5.1(b)). Since the measurements were performed at room temperature, the edge of the membrane frame was set to 295 K.

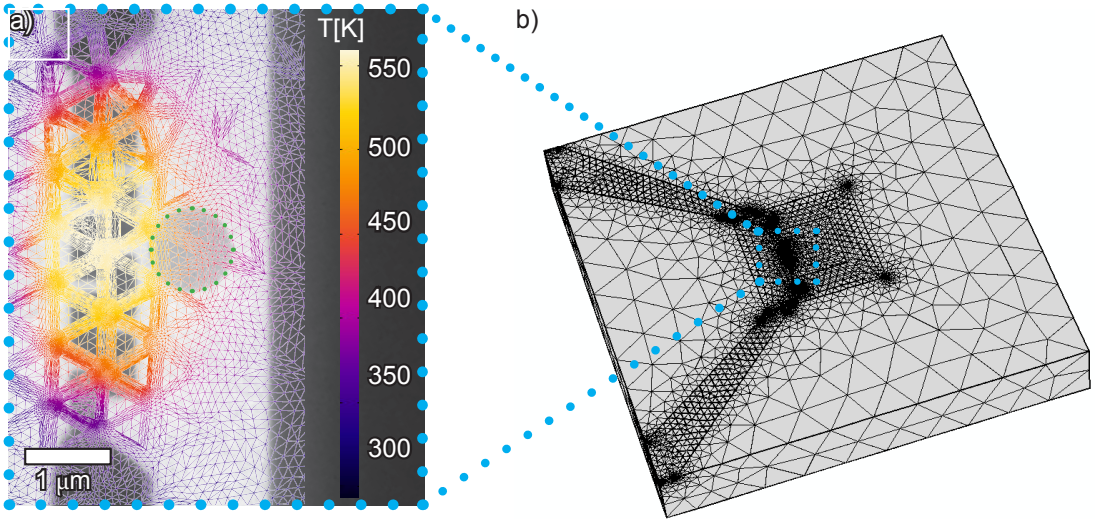

Figure 5.1: (a) TEM overview image of the sample. The meander heater, to which the heating voltage U_{heat} is applied, is on the left side on top of the SiN-membrane (bright contrast). The membrane frame which functions as heatsink is on the right side (dark contrast). The Py disk is indicated by the green dots. The temperature distribution at $U_{heat} = 0.25V$ is plotted using the colorscale on the right for the used mesh points. (b) Mesh geometry used for the simulations.

Even though the stationary simulation of nanometer-sized geometries (by a lot larger than the relevant phonon wavelengths) using the described methods is a straight forward classical approach, an unsuitable choice of meshing or parameters can lead to numeric errors. To benchmark the performed calculations special calibration samples were produced. The samples consist a meander heater structured on the SiN-membrane and an additional probe line (see fig. 5.2(a)). A voltage of $U_{heat} = 0\,\mathrm{V}$ to $0.37\,\mathrm{V}$ is applied to the heater. The resistivity of the heater and an additional metal probe structured at the edge of the membrane, which doubles as heat sink, is monitored during the voltage sweep. Together with the temperature coefficient of Au ($\alpha = 0.0034\,\mathrm{K}^{-1}$) these resistivity measurements can be used to experimentally determine the temperature gradient between the two elements (see fig. 5.2(b)).

These measurements were performed in the framework of the Bachelor Thesis of Bernhard Zimmermann [139] and are in good agreement with the simulations. The materials used as well as the overall dimensions are the same for the experi-

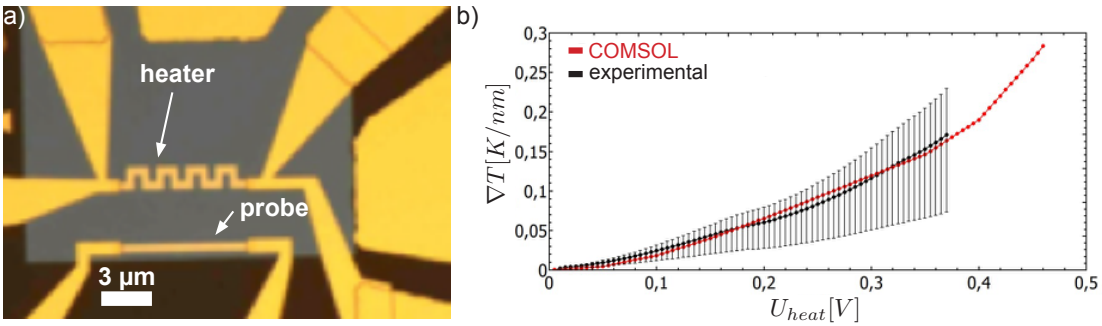

Figure 5.2: (a) Microscope image of the calibration sample design. The meander heater is structured on the SiN-membrane (light grey), the probe is placed on the edge of the Si frame (dark). (b) The temperature gradients from the COMSOL calculations (red) are compared to the experimental data (black).

ments presented here. The same parameters and meshing methods were used in section 5.2 and section 5.3.

5.2 Generating high temperature gradients on a SiN-membrane

As discussed in section 4.1.1 the SiN-membranes are an ideal platform for controlled temperature landscapes [128]. To displace a magnetic vortex core from its equilibrium position high temperature gradients are needed as shown by the calculations using an extended Thiele equation model (see section 2.3). To realize temperature gradients of such magnitude the Py disk is placed between the meander heater ($R = 100\,\Omega$ at $T = 109\,\mathrm{K}$) and the edge of the SiN-membrane (see fig. 5.3). The z dimension of the frame ($t = 200\,\mu\mathrm{m}$) is infinitely thick compared to the membrane itself ($t = 30\,\mathrm{nm}$) (see fig. 4.2) and functions as an ideal heatsink.

The calculated temperature gradients are shown in fig. 5.4. For applied voltages of up to $U_{heat} = 0.37\,\mathrm{V}$ temperature gradients of $\nabla T = 0.21\,\mathrm{K\,nm^{-1}}$ are reached. As can be seen the measurements do not go beyond 0.37 V, since the heater reaches temperatures close to the melting temperature of Au and can not be used anymore due to irreversible changes (destroyed). According to the calculation using an extended Thiele equation model (section 2.3) temperature gradients in the order of 0.1 K/nm are sufficient to experimentally observe a shift of the vortex core position due to thermomagnonic excitation of the vortex core. Thus, in the experiment voltages of up to 0.27 V are applied. The experimental results are presented in chapter 7.

Due to the electric current passing through the heater an Oerstedfield is created. This field is mainly perpendicular to the sample plane due to the sample geometry. The field can also be simulated by the COMSOL simulations. The out of plane

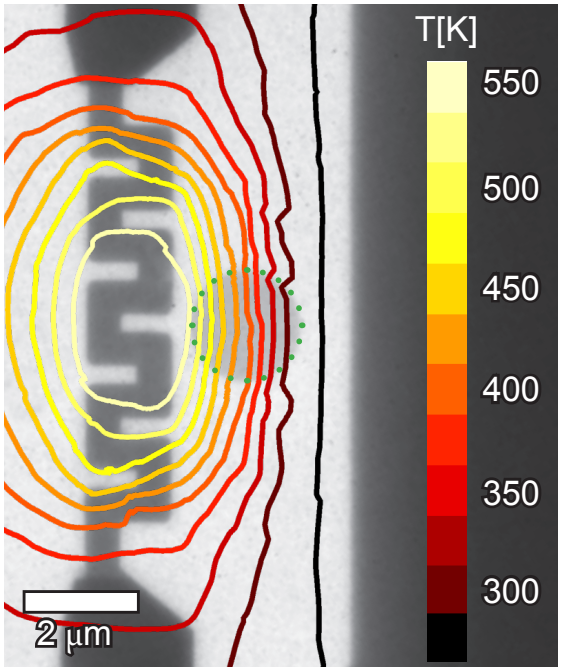

Figure 5.3: TEM overview image of the sample. The meander heater, to which the heating voltage U_{heat} is applied, is on the left side on top of the SiN-membrane (bright contrast). The membrane frame which functions as heatsink is on the right side (dark contrast). The Py disk is indicated by the green dots. The temperature distribution at $U_{heat} = 0.25V$ is plotted using the colorscale on the right.

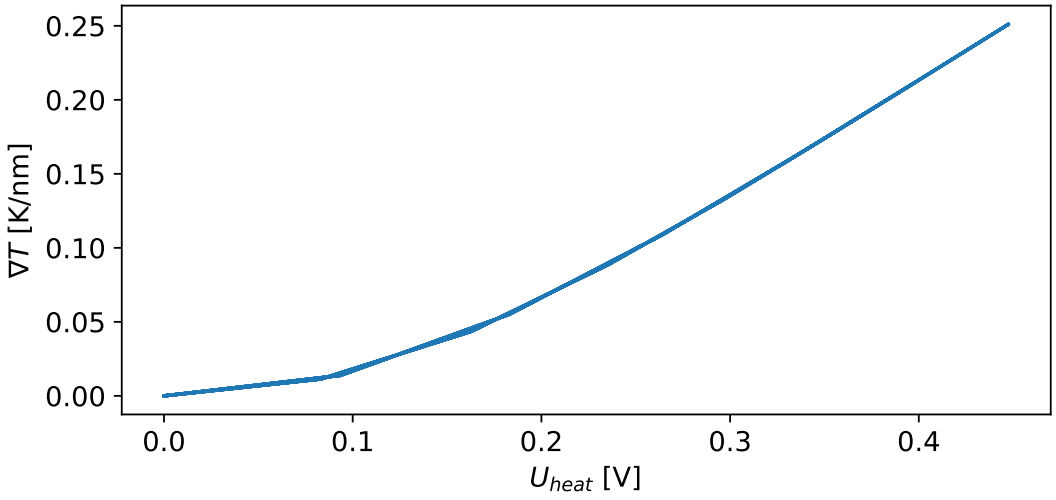

Figure 5.4: Temperature gradient ∇T vs voltage applied to heater U_{heat}, at the center of the Py disk from 3D finite elements COMSOL simulations.

component is below $B_z < 10\,\mathrm{mT}$ and does not cause a lateral motion of the magnetic vortex core. The in plane component is about two orders of magnitude smaller and can be neglected as well.

5.3 Heating a single disk in a pair of coupled vortex oscillators

Here we investigate a system of two permalloy disks (radius $r = 0.9\,\mu m$, thickness $d = 50\,nm$) placed next to each other on a thin 30 nm SiN-membrane needed to perform Lorentz Transmission Electron Microscopy (LTEM) and Scanning Transmission X-ray Microscopy (STXM). A continuous wave (cw) excitation is applied to the right "driven" disk ($disk_d$) to excite the coupled system harnessing the Spin Transfer Torque effect (STT) [140]. A dc-voltage U_{heat} is applied to the left "heated" disk ($disk_h$) to change its temperature via joule heating and thereby the saturation magnetization M_S (see section 2.4). The temperature of the heated disk can be estimated by

$$T_h = T_0 + \frac{R_{thermal}}{R_d + R_c} U_{heat}^2, \tag{5.4}$$

with $T_0 = 293.15\,K$ being the ambient temperature, $R_d = 90\Omega$ the electrical resistance of $disk_h$ at T_0, and R_c the resistance of the electrical contacts. $R_{thermal} = 63\,300\,K\,W^{-1}$ is the thermal resistance calculated using 3D finite elements methods (FEM). The right $disk_d$ stays at ambient temperature as shown by the 3D FEM simulations (see fig. 5.5), which can be explained by the low thermal conductivity through the thin SiN-membrane.

This configuration allows for a controlled way to change the temperature of $disk_h$ without significant influence on the temperature of $disk_d$. The results on the phase manipulation in such a network of two magnetic vortex core oscillators are presented in chapter 6.

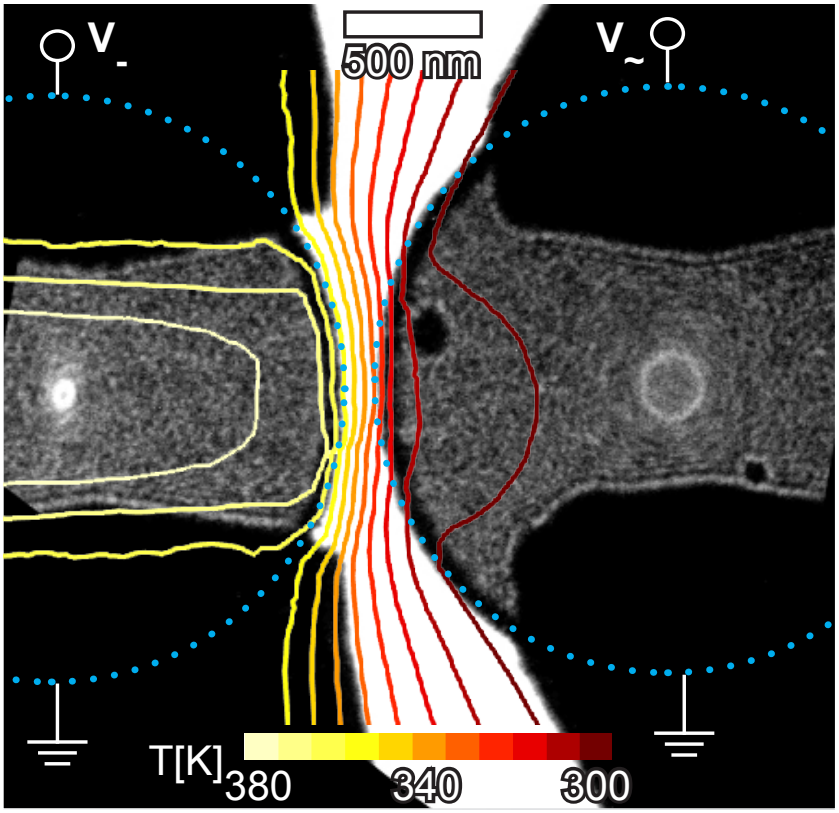

Figure 5.5: L-TEM image of the pair of magnetic vortex oscillators with a radius of $r = 0.9\,\mu m$. The gyration mode is driven by a cw excitation at 239 MHz applied on the right disk ($disk_d$), as can be seen at the middle of both disks in form of bright ellipses. A dc voltage U_{heat} is applied on the left "heated" disk ($disk_h$). U_{heat} is varied between 0 V to 0.4 V to manipulate the phase. In addition, the contour lines of the temperature distribution at $U_{heat} = 0.4\,V$ are plotted. The driven disk ($disk_d$) remains at ambient temperature.

Part II

Results

6

Fine-grain phase control in magnetic vortex oscillators networks for neuromorphic computing

As discussed in chapter 1 the goal of this experiment is to manipulate the phase relation in a pair of coupled magnetic vortex core oscillators. Phase manipulation in a controlled manner and phase contrast in ONNs is critical and promises a wide range of applications mimicking rhythmic motive patterns in robotics [18, 19] to neuromorphic image recognition [20]. In many cases the computation of "grey-scale" data favours fine grain phase manipulation for fast parallel processing [141, 142]. n ONNs consisting of compact electronic oscillators phase manipulation has been a challenging problem and despite promising efforts made with spin-torque oscillators [143] and oxide electronics based oscillators [144, 145] so far mainly binary phase contrast has been achieved. Fine-grain phase contrast has only recently been demonstrated in resistive random access memory type oxide oscillators [146] at relatively low frequencies. In this chapter fine-grain phase control in a pair of coupled magnetic vortex core oscillators (see Fig. 5.5) is demonstrated. This can help advance the efforts into high frequency neuromorphic spintronics. Here the dynamics of a system of two Permalloy disks (radius $r = 0.9\,\mu m$, thickness $d = 50\,nm$) placed next to each other on a thin 30 nm SiN-membrane is investigated by Lorentz Transmission Electron Microscopy (L-TEM) and Scanning Transmission X-ray Microscopy (STXM). A continuous wave (cw) excitation is applied to the right driven disk ($disk_d$) to excite the coupled system, harnessing the Spin Transfer Torque effect (STT) [140] (see fig. 6.1(a)). The

resonance frequencies are determined in L-TEM measurements by sweeping the excitation frequency (see section 6.1). To further investigate the phase relation time-resolved STXM measurements at the MAXYMUS Beamline at Bessy II in Berlin were performed, the results can be found in section 6.2. To manipulate the phase in a controlled manner dc-voltage U_{heat} is applied to the left heated disk ($disk_h$) to change its temperature via Joule heating and thereby the saturation magnetization M_S. The dynamics of this system can be modelled using two coupled Thiele equations [24, 74] as shown in section 2.4.

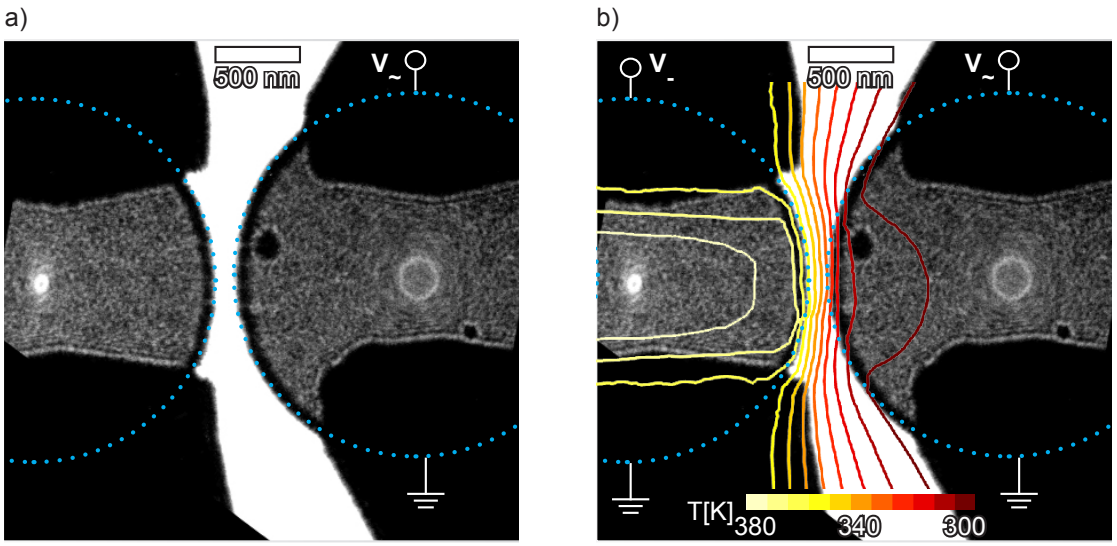

Figure 6.1: (a) L-TEM image of the pair of magnetic vortex oscillators with a radius of $r = 0.9\,\mu m$. The gyration mode is driven by a cw excitation at 239 MHz applied on the right disk ($disk_d$), as can be seen at the middle of both disks in form of bright ellipses. The excitation in the disk on the left $disk_h$ (which is later heated) is due to mutual dipolar interaction. A series of such images is taken at different excitation frequencies. The two axes of each of the two ellipses are determined to resolve the frequency spectra of the excitation in both disks (see fig. 6.2). (b) For the time resolved STXM measurements the gyration mode is driven by a cw excitation at the fixed, previously determined in phase frequency $f_{in} = 239\,MHz$, applied on the right disk ($disk_d$). In addition a dc voltage U_{heat} is applied on the left heated disk ($disk_h$). U_{heat} is varied between 0 V to 0.4 V to manipulate the phase. As described in section 5.3 the temperature of $disk_h$ can be increased in a controlled manner while $disk_d$ remains at ambient temperature.

6.1 Frequency spectra of a pair of coupled vortex oscillators

The frequency spectra shown in fig. 6.2 were determined by L-TEM measurements performed in the group of Prof. Zweck at the University of Regensburg in cooperation with Johannes Wild and Felix Schwarzhuber. To investigate the phase relation in a pair of coupled vortex oscillators the excitation frequency is crucial (see fig. 2.20). Even though it is possible to determine the resonance frequencies in a ring down experiment (as demonstrated theoretically in fig. 2.18) using pulsed excitation harnessing the time-resolved measurement capabilities of the STXM measurements, knowledge of the frequency resonance spectra beforehand saves measurement time and allows to confirm theoretical assumptions such as the coupling strength and damping parameters used for the coupled Thiele equations in section 2.4. To resolve the two resonance frequencies of the coupled system, frequency sweep L-TEM measurements were performed (see fig. 6.1(a)). A cw excitation of 0.15 V was applied to $disk_d$ and the frequency varied from $f = 200\,\mathrm{MHz}$ to 300 MHz in steps of 3 MHz. For each frequency an image (fig. 6.1(a)) was taken. From the images the two axes A_x and A_y of each of the elliptical excitations in the two disks was measured by automatic image recognition and the average $r_a = (A_x + A_y)/2$ calculated. When plotted against the applied frequency the two resonance frequencies (in phase f_{in} and out of phase f_{out}) can be resolved. The spectra are shown in fig. 6.2. The blue spectrum corresponds to the driven $disk_d$ and the red spectrum to $disk_h$, which is later heated to control the phase between both excitations. The resonance frequencies are indicated by green lines. The overall shape of the spectra is in agreement with the theoretical model (compare fig. 2.18) and behaves similar to a diatomic molecule with bonding and antibonding states [147].

To further investigate the phase relation, time-resolved STXM measurements at the MAXYMUS Beamline at Bessy II in Berlin were taken. First the $disk_d$ was excited by a 0.15 V at the previously determined resonant frequencies, in a similar manner to the L-TEM measurements. The gyration was resolved with a time resolution of 66 ps leading to a series of 62 images. One image for each disk and each frequency combination is shown in fig. 6.3. The bright spot on the dark background is a direct image of the z-component of the magnetization M_z and allows to determine the polarities $p_d = p_h = 1$ for the two disks. The sense of rotation for both disks is counter clockwise (ccw) and hence, in combination with the observed polarity, the chirality can be determined to be $C_d = C_h = 1$ [147], which serves as an input for the simulations. The positions of the vortex core were tracked by the Laplacian of Gaussian method [140] and are overlaid on the image

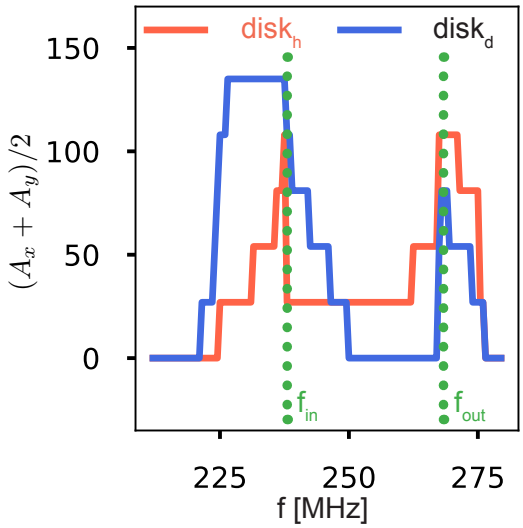

Figure 6.2: Average $(A_x + A_y)/2$ of both elliptical vortex core excitations retrieved from L-TEM measurement (see fig. 6.1) vs. frequency. The blue spectrum corresponds to the driven $disk_d$ and the red spectrum to $disk_h$, which is later heated to control the phase between both excitations. The resonance frequencies are determined by taken the maxima of both spectra into account: resonances at $f_{in} = 238\,\mathrm{MHz}$ and $f_{out} = 270\,\mathrm{MHz}$.

as white spots for all 62 measurements, with the position of the shown image colored in red. This data can be plotted against time and fitted by a least squares sinusoidal fit with a fixed frequency equal to the excitation frequency. From the fit the phase between the two disks is retrieved. The error for the phase is determined by the error from the covariance matrix in combination with an estimated error of $\Delta_{x,y} = \pm 50\,\mathrm{nm}$ for the vortex core position by simple propagation of uncertainty. Further the eccentricity $e = A_x/A_y$ of the elliptical trajectory is calculated. The experimental results match the theoretical predictions:

	Phase [°]		Eccentricity			
f[MHz]	φ_{exp}	φ_{th}	e_{hexp}	e_{dexp}	e_{hth}	e_{dth}
238	16.4 ± 7	15	0.80	0.88	0.95	096
270	176.3 ± 8	176	1.12	1.02	1.05	1.04

Table 6.1: Experimental values from STXM measurements of phase and eccentricity compared to simulations using coupled Thiele equations.

The measured phase is in good agreement with the results from the calculations. The change of the eccentricity from $e < 1$ to $e > 1$ is typical [147].

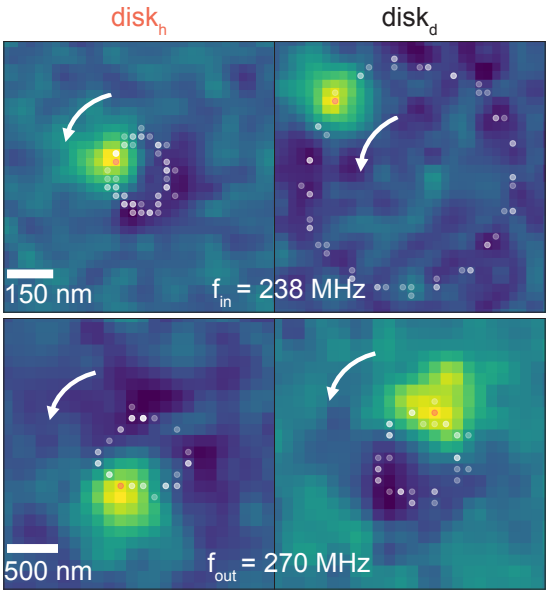

Figure 6.3: STXM measurements at f_{in} (upper) and f_{out} (lower) with respective phase-shifts of 16.4° and 176.3°.

6.2 Phase manipulation in a pair of coupled vortex oscillators

To manipulate the phase a voltage U_{heat} applied to $disk_h$ is now increased stepwise from 0 V to 0.43 V while the frequency of the excitation is kept constant at 239 MHz. For each heating voltage a series of images with the same time resolution as before is captured. A series of five images from the minimum and maximum heating voltage is shown in fig. 6.4(a). For $U_{heat} = 0$ V the coupled system is in the in phase resonance, similar to the upper pair of images in fig. 6.3. The images show the vortex cores in both disk almost in the same state of the oscillation. For $U_{heat} = 0.43$ V the vortex cores are on opposing sides in the two disks similar to the lower images in fig. 6.4. In this case this is achieved by manipulating the saturation magnetization M_{Sh} of $disk_h$ rather than changing the excitation frequency. Since the temperature of $disk_d$ stays at ambient temperature, according to section 5.3 the saturation magentization of $disk_d$ M_{Sd} stays constant.

The eccentricity and phase are calculated in the same manner as in section 6.1 for all 15 different applied values of U_{heat}. The results for the experimental resolved phase relation are shown in fig. 6.4(b) as orange dots with U_{heat} shown in the upper axis. The series starts again at a phase of 16.4° for $U_{heat} = 0$ V and the phase shifts up to a maximum of 167° for $U_{heat} = 0.43$ V caused by a temperature increase of up to 85 K. In the simulation these two states correlate to a ratio of $M_{Sh}/M_{Sd} = 1$ for the in phase state and $M_{Sh}/M_{Sd} = 0.85$ for the out of phase state (see section 2.4). The temperature dependence of the ratio of $M_{Sh}(T)/M_{Sd}$ can be approximated

via Bloch's law [68]:

$$M_{Sh}(T) = M_0 \left(1 - \left(\frac{T}{T_c}\right)^{\frac{3}{2}}\right) = M_0 \left(1 - \left(\frac{T_0 + \beta U_{heat}^2}{T_c}\right)^{\frac{3}{2}}\right). \tag{6.1}$$

The undetermined variable, the Curie temperature T_c, can be used as a fitting parameter for a least square fit to match the analytic values to the experimental data and one can estimate an experimental value of T_c, which can be compared to data from literature. By the nature of the fit, this is a very crude method of determining T_c. However, the received value of $T_c = 885\,\mathrm{K} \pm 200\,\mathrm{K}$ is in good agreement with literature [119]. The resulting plot (fig. 6.4(b)) shows a good agreement of the theory data (blue) with the experimental measured phase-relations (orange symbols). Fine-grain phase manipulation in a controlled manner of a pair of magnetic vortex oscillators has been shown. The proposed method allows for a high resolution of the desired phase differences, which is basically only limited by the measurement time. An additional sanity check of the applied theoretical framework is shown in section 6.3 by examination of the phase difference dependency of the eccentricity of the elliptical excitation.

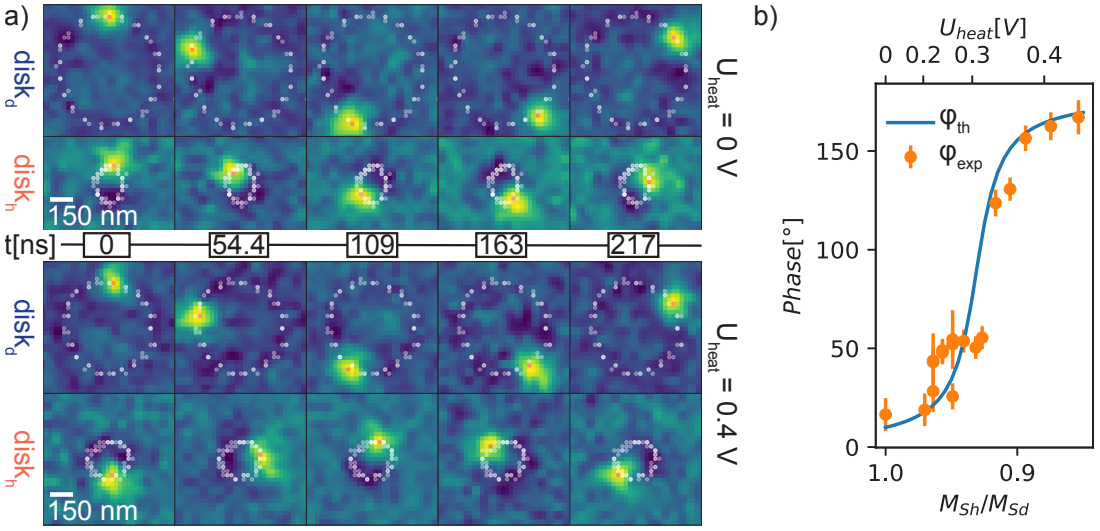

Figure 6.4: a) STXM image series for $f_{ex} = 239\,\mathrm{MHz}$ and $U_{heat} = 0\,\mathrm{V}$ (top) as well as $U_{heat} = 0.43\,\mathrm{V}$ (bottom). For $U_{heat} = 0\,\mathrm{V}$ the phase between both oscillators is $16.4° \pm 7°$. For $U_{heat} = 0.43\,\mathrm{V}$ the phase is increased to $167.1° \pm 12°$, and the vortex cores are almost on the opposite side of the gyration. Only 5 out of the 62 frames are plotted. All vortex core positions are overlaid in white. b) The phase φ_{ex} retrieved from STXM data is plotted against U_{heat} and the corresponding ratio of $\frac{M_{Sh}}{M_{Sd}}$. It agrees with the calculated phase change φ_{th}.

6.3 Dependence of the eccentricity on phase difference

As shown in fig. 2.21 the transition from the in phase to the out of phase state is combined by a change of the eccentricity from $e_h < 1$ to $e_h > 1$ for $disk_h$ while the elongation of excitation in $disk_d$ does not change $e_d < 1$. This behaviour can also be observed in the experimental data as shown in fig. 6.5. The experimental resolved eccentricity of the driven disk e_{dexp} is shown in red. The error for the phase is the same as in fig. 6.4. The error of the eccentricity follows from the error of the recorded values for the two axes A_x and A_y of the elliptical excitation by error-propagation. As can be seen e_{dexp} stays below a value of 1 (green line) for the described transition between the two states. The eccentricity e_{hexp} of the heated disk $disk_h$ on the other hand changes from $e_{hexp} < 1$ for phase-shifts below 90° to $e_{hexp} > 1$ for phaseshifts above 90° (within the errorbars). This agrees with the simulations in section 2.4. The overall behaviour of the eccentricities of the two disks is also reproduced. However, the small changes predicted by the coupled Thiele equation are difficult to resolve with used experimental resolution. Nevertheless, the recorded change of an elongation of the elliptical excitation from the y direction to the x direction for $disk_h$, without such a change in $disk_d$, is an additional sanity check for the applied theoretical model.

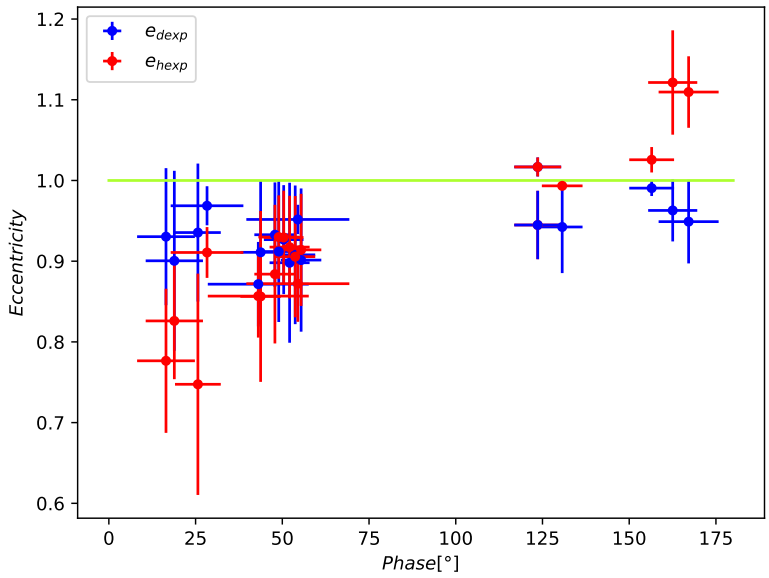

Figure 6.5: Eccentricity e for the experimentally resolved elliptical trajectory of the two vortex gyrations as a function of phase difference. The eccentricity e_{dexp} for the driven disk $disk_d$ is shown in blue. For the heated disk $disk_h$ the eccentricity e_{hexp} is shown in red. To exemplify the change of $e_{hexp} < 1$ to $e_{hexp} >$ the green line at $e = 1$ is shown.

7

Vortex Core Motion driven by Magnon Spin Seebeck Effect

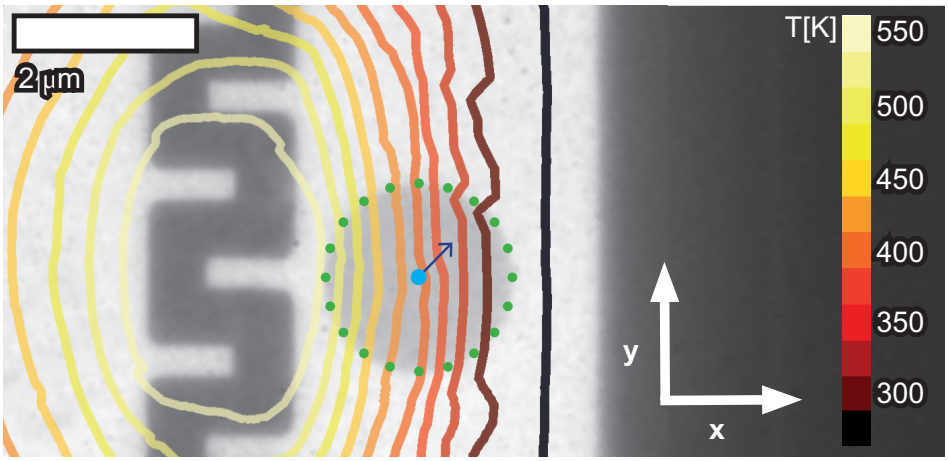

Figure 7.1: TEM image of the used sample geometry. The meander heater can be seen on the left on the SiN-membrane (light contrast). The Py disk is placed between the heater and the frame of the membrane (dark contrast) on the right which doubles as heatsink. The isothermals of the temperature distribution calculated by 3D FEM simulation (see section 5.2) is overlaid with the color temperature scale on the very right. The temperature gradient ∇T is along the x axis. In the magnetic ground state the vortex core is at the center of the disk (blue dot). The calculated direction of the lateral movement of the vortex core due to ∇T is indicated by the blue arrow. The y component of this movement is caused by thermally induced thermal magnon spin transfer torque (TMSTT) and dependents on the vortex polarity p. The movement parallel to the direction of ∇T is due to the reduction of the saturation magnetization in the hot side of the Py disk, next to the heater, and independent of p (see fig. 2.17).

This chapter focuses on the Lorentz Transmission Electron Microscopy (L-TEM)

measurements performed to investigate the motion of a magnetic vortex core due to an applied temperature gradient ∇T. A sketch of the measurement setup is shown in fig. 7.1. The temperature gradient is created by placing a Py disk (green) on a 30 nm thick SiN-membrane (light contrast) between a meander Au heater (shown on the left side) and the membrane frame (dark contrast), which acts as a heatsink due to being infinite thick (200 µm) compared to the membrane. The used coordinate system is also shown. Due to the geometry the direction of ∇T is along the x axis. As shown in section 2.2 the dynamics of magnetic vortex cores are theoretically well understood. This is of great importance, since the essence of the experimental problem to resolve the movement of the vortex core, due to the application of a temperature gradient, is essentially a scaling problem. The motion of the vortex core scales with the lateral and perpendicular dimensions of the Py disk (see section 2.2). Lateral the movement of the vortex core scales almost linear with the size of the magnetic element (see fig. 2.9) favouring large diameters for the Py disk to create an experimentally accessible movement. Simultaneously a large temperature gradient in the order of 0.1 K/nm (see fig. 2.9) is needed, which restricts the maximum size of the Py disk. As shown in section 5.2 temperature gradients of this size can be achieved by the proposed sample geometry. To observe a large movement of the vortex core, thin samples are favourable as shown in fig. 2.9. The minimum film thickness of the Py disk is limited by the roughness and quality of the substrate due to the increasing role of local pinning sites in thinner samples. The overall quality of the SiN-membranes, needed for the L-TEM measurements and the creation of large ∇T, as substrate is anything but optimal due to the roughness and large number of local defects compared to bulk substrates (see fig. 4.3). The defects can cause an increased number of local pinning center as shown in fig. 2.5. By taking all these effects into account the diameter of the Py disk was chosen to be 2 µm and the thickness 20 nm. The simulations predict a lateral movement (see fig. 2.17) of the vortex core, that is experimentally resolvable with the high resolution L-TEM measurements performed here. The coordinate system is also shown in fig. 7.1. The equilibrium position of the vortex core is at the center of the Py disk (indicated by a blue dot). The predicted movement (indicated by the blue arrow, not to scale) has a component Δy orthogonal to the temperature gradient direction mainly due to magnon spin transfer torque as shown in fig. 2.17(a,b,c,d). For different vortex polarities, this movement changes its sign. In addition one observes a movement parallel to ∇T, as shown in fig. 2.17(e), due to the partial reduction of the saturation magnetization M_S of the Py disk at the hot side next to the heater (left). This movement Δx is in positive x direction. Unlike Δy, this movement is always directed away from the hot side of the sample to the cold side, independent of the vortex polarity. The

Oerstedfield, created by the electric current induced by an applied Voltage U_{heat} to the meander heater, is too small (see section 5.2) to cause a lateral movement of the vortex core. To further exclude its influence, the sign of U_{heat} is reversed. This reversal causes also a sign change in the current I flowing through the heater and thus, due to the linear dependence of the Oerstedfield on I, reverses any observable movement. The measurements were performed in the group of Professor Zweck in Regensburg in cooperation with Johannes Wild. The defocus for the L-TEM measurements is set to 15 µm which allows for a resolution of $\approx 10\,\mathrm{nm}$ [110] and adequate contrast (see fig. 3.4). The polarity p of the magnetic vortex core was determined by tilting the sample in the out of plane field of the objective lens with decreasing values of the applied lens current. The direction of the lens current was inverted to reverse the polarity. During the measurements the focus lens is turned off, using the Lorentz lens for imaging. The micro-condenser lens is used to compensate for small remaining fields, thus the measurements are performed in a near magnet field free environment in the sample plane. The chirality c of the vortex core can be directly determined by the recorded images (see section 3.2). For all measurements taken the chirality is $c = 1$.

7.1 Observation of vortex core movement due to thermomagnonic spin torques by Lorentz TEM measurements

To measure the dependency of the vortex core movement Δx and Δy on the temperature gradient ∇T different voltages $U_{heat} = 0\,\mathrm{V}$ to $0.27\,\mathrm{V}$ are applied. Series of three images for each polarity are taken at increasing values of U_{heat}, as shown in fig. 7.2. The direction of ∇T is, as indicated by the arrow, in x direction, with the hot side being on the left. The TEM image of the sample background surrounding the vortex core is shown in greyscale. The 3 vortex core positions for the applied ∇T are shown on-top (color) blended with an intensity cut off mask. The two axes indicate the shift of the vortex core position in the x and y direction. The coordinate system is chosen in such a way that for $\nabla T = 0$ (vortex core in equilibrium state) both shifts are equal to zero. For a polarity of $p = +1$ (see fig. 7.2(a)) the vortex core shifts to positive values of Δy. The shift increases with higher values of ∇T. If the polarity is switched to $p = -1$, the direction of the shift in y direction also changes sign, causing a downward movement of the vortex core in fig. 7.2(b). This agrees with the theoretical predictions (see fig. 2.17). In both cases the shift along the direction of ∇T is from the hot to the cold side, which also agrees with fig. 2.17(e). However, there is a small deviation of the

magnitude of the shifts from $p = +1$ to $p - 1$. This is caused most likely by the local energy landscape created by pinning centers.

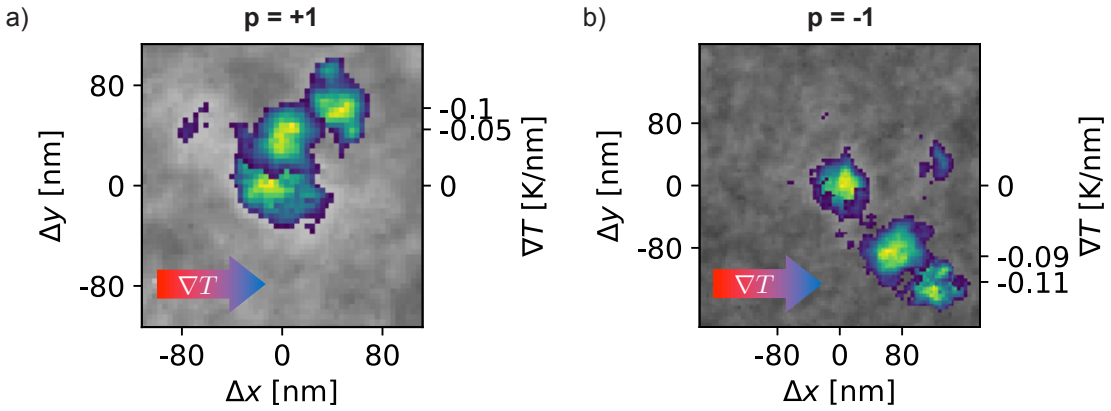

Figure 7.2: L-TEM measurements for 3 different applied temperature gradients ∇T. The direction of ∇T is indicated by the arrow, with the hot side being on the left. The TEM signal of the sample background surrounding the vortex core is shown in greyscale. The 3 vortex core positions for the applied ∇T are shown on-top (color) blended with an intensity cut off mask. The additional y-axis on the left shows the temperature gradients. (a) For a polarity $p = +1$ the vortex core shifts to positive Δy with increasing ∇T due to TMSTT. (b) For a reversed polarity $p = -1$ the vortex core shifts to negative values Δy with increasing ∇T. In both cases a shift in positive x-direction is observed due to the partial demagnetization of the Py disk on the hot side.

7.2 Statistic investigation of the movement due to thermomagnonic spin torques

To further investigate this behaviour and rule out the possibility of the change of direction of Δy, being solely due to local energy landscape, a series of 256 measurements, with samples prepared in the same manner, was performed. The positions of the vortex cores were tracked by the Laplacian of Gaussian method [140] and the relative shifts Δx and Δy from the equilibrium position at the beginning of each image series were determined. The results are shown in fig. 7.3. For a polarity $p = +1$ (see fig. 7.3(a)) the shifts are again to positive values of Δy. The influence of the local energy landscape due to local pinning centers becomes visible in plateaus of Δy, especially for small values of ∇T. In this case the magnitude of MSTT needs to overcome a threshold value. In most measurements the observed shifts after overcoming this threshold show a linear dependency on ∇T. In some cases the movement ends in a new local minimum causing a slight deviation from the linear dependency. No significant shifts to negative values are observed, if the resolution limit is taken into account. Due to the almost linear dependency of the theoretical predicted shift due to TMSTT the observed values of Δy are fitted by a linear regression (red line). The statistical error limits of the

fit are shown as blue area. Compared to the theoretical predicted Δy (indicated as solid black lines) the observed values in the LTEM measurements are slightly smaller. This can be explained by the extended Thiele model, not taking pinning centers into account. For negative values of U_{heat} and the same polarity $p = +1$ the same overall behaviour is observed, as shown in fig. 7.3(b), ruling out an influence of the Oerstedfield created by the current passing through the heater. If the polarity is reversed to polarity $p = -1$ the vortex core shifts to negative values of Δy, as can be seen in fig. 7.3(c) and (d). Taking all data points into account the average movement determined by the fit is again slightly below the theoretical predictions. As for polarity $p = +1$ the reversal of U_{heat} from positive to negative values does not change the overall direction of Δy.

In conclusion the experimental resolved movement of the vortex core in an applied temperature gradient ∇T match the theoretical predictions. A reversal of the polarization of the vortex core is accompanied by a change of the direction of Δy, the component of the movement orthogonal to ∇T. The magnitude of the observed shifts Δy is on average slightly below the theoretical results, which is caused by local pinning of the vortex core typical for thin Py films. Further the Δy scales with the effective magnon velocity as shown in figs. 9.1 and 9.2. The effective magnon velocity for a 20 nm thick Py film here is estimated as 1900 m/s [148]. By taking the linear regression, calculated from the experimental data (red line), it is possible to scale the effective magnon velocity by the fitted slope: $v_{mexp} = 2200\,\mathrm{m/s} \pm 1100\,\mathrm{m/s}$. This is by no means a precise measurement of v_m but functions as a sanity check. A reversal of the electric current direction inside the heater does not change the overall behaviour of the movement. An influence of magnetic fields induced by the electric current can be excluded. A similar sized movement parallel to ∇T is observed, independent of the polarity and the direction of the current inside the heater. This shift can be explained by the partial reduction of the saturation magnetization on the hot side of the Py element, as shown by a combination of micromagnetic and analytic calculations.

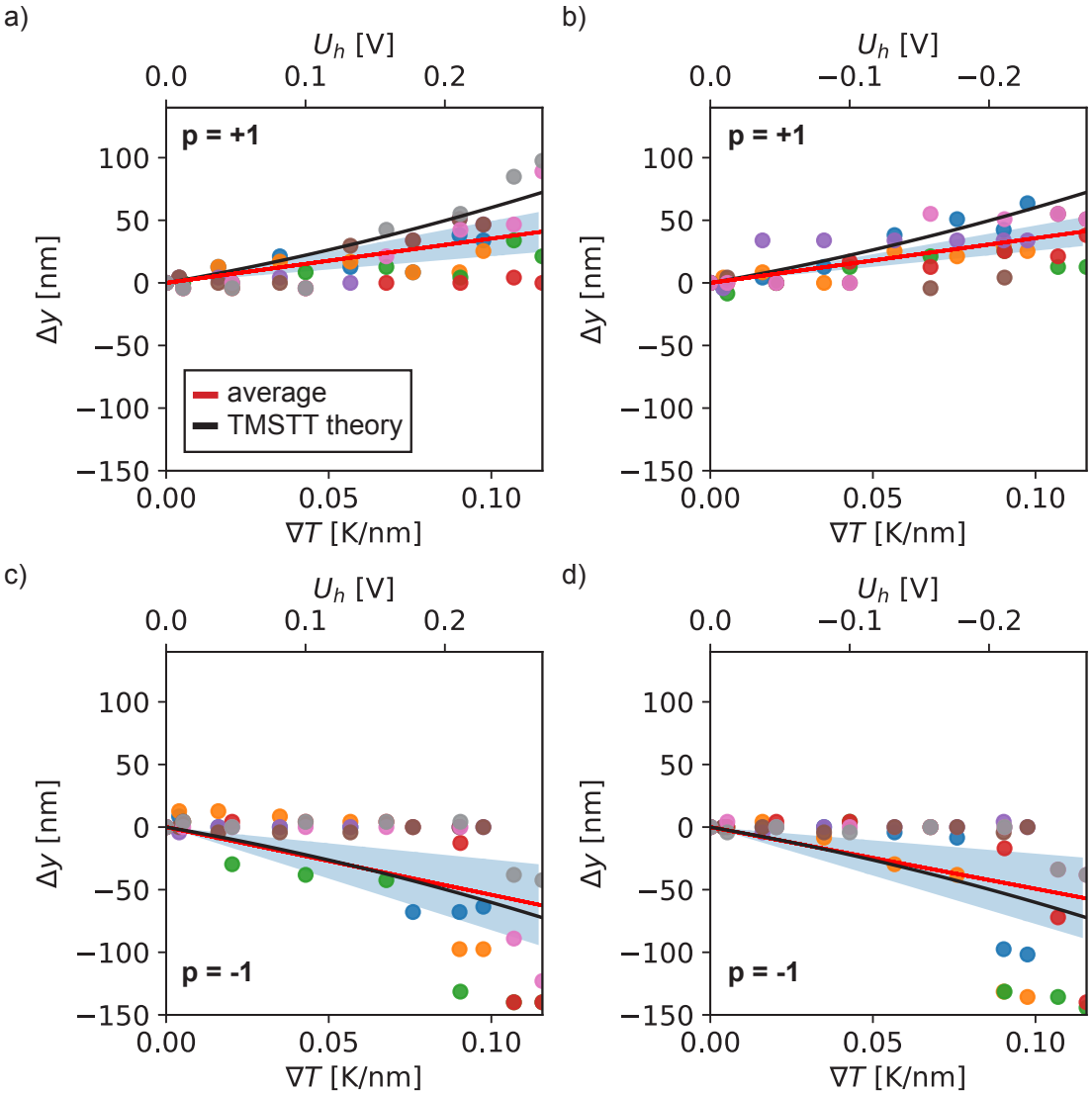

Figure 7.3: Statistic plots of the vortex core shift Δy perpendicular to the applied temperature gradient. The observed values are shown as a scatter plot with the color indicating each measurement series versus the applied temperature gradient (lower x-axis). The corresponding heating voltages U_{heat} are shown in the top x-axis. A linear fit is applied to the data points (red) with the lower and upper standard error limits shown in blue. The theoretical values obtained with an extended Thiele equation model are indicated in black. (a) For a positive polarity $p = +1$ the core shifts to positive Δy values. (b) The same shift is observed if the sign of U_{heat} is reversed. This is done to rule out any effects of the Oerstedfield created by the electric current inside the heater. (c) If the polarity is reversed, the direction of the vortex core shifts is as well, due to the symmetry of the MSTT. (d) The same shifts are observed for negative values of U_{heat}. The motion of the vortex core calculated by the extended Thiele model is shown in black. The effective magnon velocity is estimated as 1900 m/s [148].

7.3 Comparison of the movement due to spin transfer torque induced by thermal generated magnons and direct electric currents

The observed movements of the vortex core due to thermomagnonic spin torques presented in section 7.2 and section 7.1 are already of the same order of magnitude as the elliptical excitation presented in chapter 6, excited by STT via a spin polarized current directly applied to the Py disk (electron current induced STT). In case of the dynamic measurements, harnessing traditional STT, the excitation is dynamic in resonance due to pulsed or sinusoidal applied voltages. This of course increases the magnitude of the excitation by a few orders of magnitude compared to the static case. To compare the two effects, a constant dc voltage applied directly to the Py disk (see fig. 7.5(a)) is considered. Using the same theoretical framework as before (section 2.4), it is possible to calculate the movement of the vortex core dependent on the dc spin polarized current density induced by the applied voltage, as can be seen in fig. 7.4. To move the vortex core by similar amounts by traditional charge current induced STT, very high current densities have to be applied. For a movement of $\Delta y = 50\,\mathrm{nm}$ current densities in the order of $0.5 \times 10^{12}\,\mathrm{A\,m^{-2}}$ are necessary. Of course such dc current densities can not be applied without the immediate destruction of the device. The temperature of the Py disk for similar current densities due to Joule heating is shown in fig. 7.5(b). The values are calculated by the same 3d FEM simulations as performed in section 5.3. Of course this is only shown here to illustrate the impossibility of applying dc current densities of this order to similar devices. The absolute values for the calculated temperatures are far beyond the melting temperature and non-linear effects for the resistivity as well as electromigration are not taking into account.

Current densities are important to the design of electrical and electronic systems. High current densities have undesirable consequences such as the Joule heating of the surrounding area, and electromigration. The maximum electron current density in the device used in section 7.1 are inside the meander heater at $2 \times 10^{11}\,\mathrm{A\,m^{-2}}$, which is of the same order as the switching current densities used in modern magnetic tunnel junctions [149, 150] with the advantage of being not directly applied to the magnetic element.

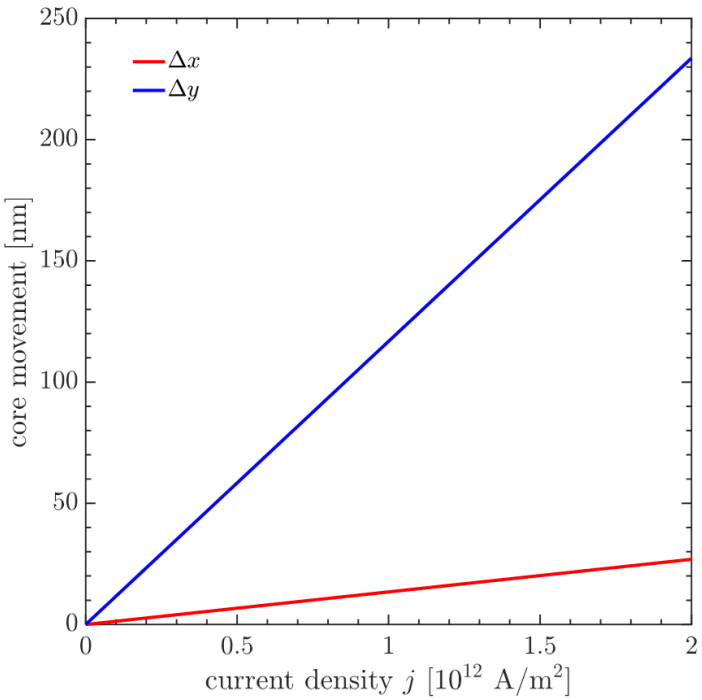

Figure 7.4: Finale core position as a function of applied current density via charge STT for a Py disk of 2 µm diameter and 20 nm thickness. The current density is applied constant (dc). Very high current densities are needed to reproduce the movements measured in section 7.1.

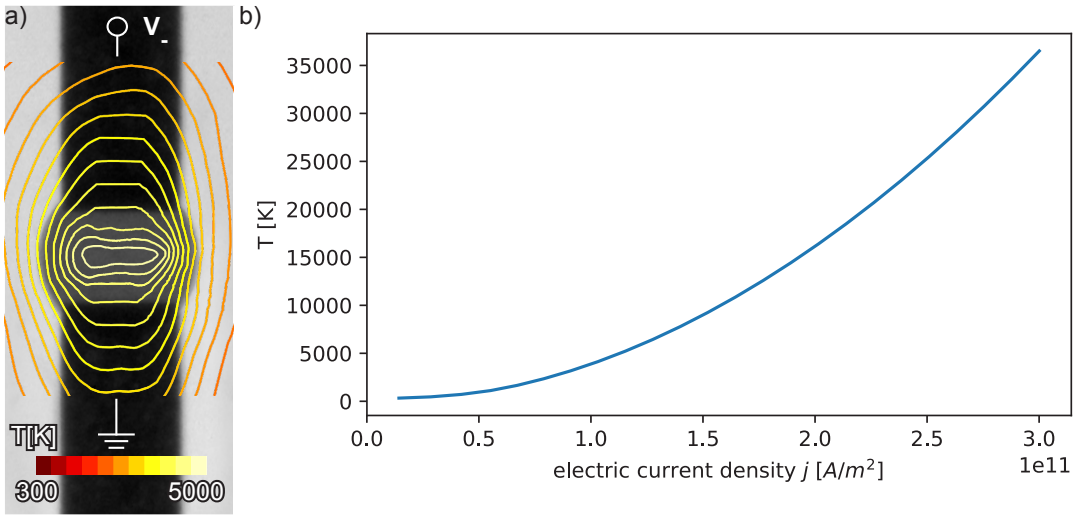

Figure 7.5: (a) TEM image of a directly contacted Py disk conventionally excited via short current pulsed or ac voltage harnessing the charge STT of the induced electric current densities. In a gedankenexperiment a dc voltage is applied to the Py element to determine the movement of the vortex by a constant excitation. (b) The current density at the center of the Py disk is plotted versus the simulated temperature, this is only shown here to illustrate the impossibility of applying dc current densities of the order needed to achieve movement similar to section 7.1. The simulated disk has the same dimensions as before with a diameter of 2 µm and a thickness 20 nm.

8 Summary / Outlook

In the first experiment in this thesis fine-grain phase manipulation for a pair of magnetic vortex oscillators in a controlled manner with high resolution (basically only limited by the measurement time) is demonstrated. The measurements are performed at 239 MHz, but vortex core dynamics are easily scalable from the kHz to the GHz regime. Therefore, the findings allow a new way of phase manipulation in oscillatory networks at high frequencies. The power needed to control the phase is significant at 1.7 mW, but scales down orders of magnitudes for nano-oscillators. Moreover, we have developed a new way of phase programming over a wide range from 16.4° up to 167°.

The second experiment demonstrates the manipulation of the vortex position due to application of a thermal gradient. The developed theoretical framework combines analytical and numerical approaches to identify the contribution of the different involved forces. Thus, the driving force for the lateral movement orthogonal to the applied temperature gradient, and depending on the polarity of the vortex core, can be identified as pure thermomagnonic torque. This shows a new efficient way to manipulate vortex core dynamics. Due to theoretical well described vortex core dynamics, it further allows a deeper insight in the interaction of thermomagnonics with magnetic solitons.

9 Appendix

9.1 Material parameters

9.1.1 3D FEM temperature simulation parameters

Material	Parameter	Value	Unit	Reference
Au	λ	317	W / (mK)	Comsol Multiphysics
Au	c_p	129	J / (kg K)	Comsol Multiphysics
Au	ϱ	19300	kg / (m^3)	Comsol Multiphysics
Au	ϵ_R	6.9	1	Comsol Multiphysics
Au	σ	45.6×10^6	S/m	Comsol Multiphysics
Au	ρ	2.2×10^{-8}	Ωm	Comsol Multiphysics
Au	α	0.003	1	Comsol Multiphysics
Si	λ	130	W / (mK)	Comsol Multiphysics
Si	c_p	700	J / (kg K)	Comsol Multiphysics
Si	ϱ	2329	kg / (m^3)	Comsol Multiphysics
Si	ϵ_R	11.7	1	Comsol Multiphysics
SiN	λ	20	W / (mK)	Comsol Multiphysics
SiN	c_p	700	J / (kg K)	Comsol Multiphysics
SiN	ϱ	3100	kg / (m^3)	Comsol Multiphysics
SiN	ϵ_R	9.7	1	Comsol Multiphysics
SiN	σ	≈ 0	S / m	Comsol Multiphysics
Py	λ	46.4	W / (mK)	[151]
Py	c_p	430	J / (kg K)	[151]
Py	ϱ	8700	kg / (m^3)	[151]
Py	ϵ_R	1	1	[151]

9.2 Scaling behaviour of vortex core motion dependent on the magnon velocity

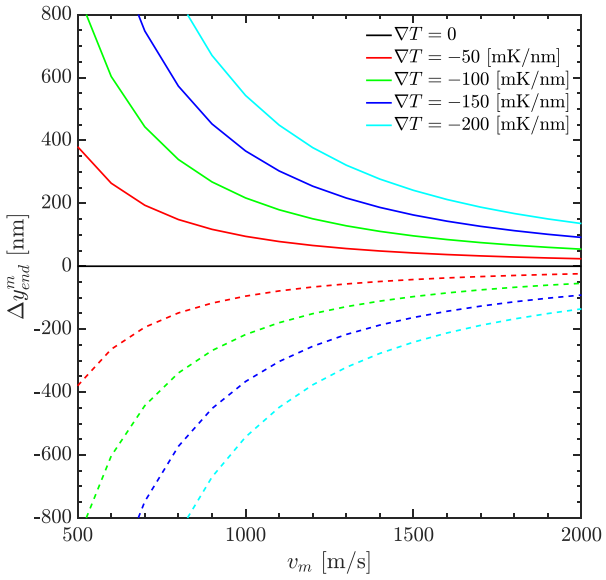

Figure 9.1: Vortex core movement Δy^m_{end} perpendicular to the temperature gradient as a function of the effective magnon velocity v_m. The different colors represent different linear temperature gradients applied to the 2 µm × 2 µm × 20 nm sample along the x direction. The right side of the sample is kept at 300 K and the left side of the sample is heated to temperatures up to 700 K. The solid lines are for a vortex polarity of $p = +1$ and the dashed lines for a vortex polarity of $p = -1$.

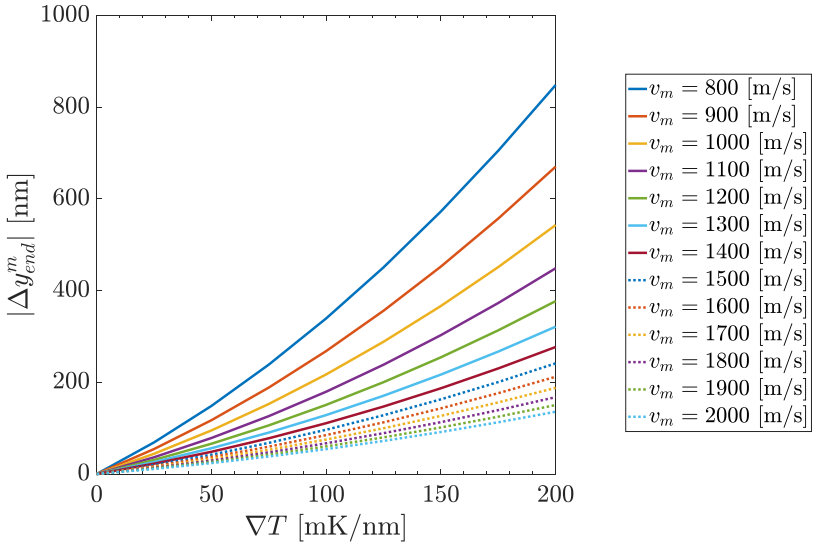

Figure 9.2: Vortex core movement Δy^m_{end} perpendicular to the temperature gradient as a function of the temperature gradient. The different colors are for different effective magnon velocities v_m ranging from 800 m/s to 2000 m/s.

PUBLICATIONS

Journal Articles

- Decker, M., Woernle, M., Meisinger, A., **Vogel, M.**, Körner, M. S., Shi, G. Y., Song, C., Kronseder, M., and Back, C.H. (2017). "Time resolved measurements of the switching trajectory of Pt/Co elements induced by spin-orbit torques". In: *Phys. Rev. Lett.* URL: https://journals.aps.org/prl/accepted/c207fY99P1c1d863c4de527032f6b8abbd2191988%20https://arxiv.org/abs/1704.06418.
- Srichandan, S., Wimmer, S., Kronseder, M., **Vogel, M.**, Ebert, H., Back, C.H., and Strunk, C. (2017). "Magnon scattering in the transport coef□cients of CoFe alloys". In: *In Preparation*.
- **Vogel, M.**, Schillinger S., Deutsch S., Mewes, T., Mewes, C.K.A., and Back, C. H. (2017). "Vortex core motion driven by thermal gradients ". In: *in preparation*.
- **Vogel, M.**, Stigloher, J., Decker, M., Zimmermann, B., Müller, M., and Back, C.H. (2017). "Snell's law for spin waves in a temperature gradient". In: *In Preparation*.
- **Vogel, M.**, Wild, J., Schwarzhuber, F., Zimmermann, B., Mewes, C., Mewes, T., Zweck, J., and Back, C.H. (2017). "Phase control in magnetic oscillators". In: *In Preparation*.
- **Vogel, M.**, Wild, J., Zimmermann, B., Mewes, C., Mewes, T., Zweck, J., and Back, C.H. (2017). "Phase control in magnetic oscillators". In: *In Preparation*.
- **Vogel, M.**, Zimmermann, B., Mewes, C., Mewes, T., and Back, C.H. (2017). "Manipulation of the spin wave spectrum in a magnetic bilayer by an applied temperature gradient". In: *In Preparation*.
- Kronseder, M., Meier, T. N. G., Zimmermann, M., Buchner, M., **Vogel, M.**, and Back, C. H. (2015). "Real-time observation of domain □uctuations in a two-dimensional magnetic model system". In: *Nature Communications* 6, p. 6832. ISSN: 2041-1723. DOI: 10.1038/ncomms7832. URL: http://www.nature.com/doifinder/10.1038/ncomms7832.
- Schmid, M., Srichandan, S., Meier, D., Kuschel, T., Schmalhorst, J.-M., **Vogel, M.**, Reiss, G., Strunk, C., and Back, C. H. (2013). "Transverse Spin Seebeck Effect versus Anomalous and Planar Nernst Effects in Permalloy Thin Films". In: *Physical Review Letters* 111.18, p. 187201. ISSN: 0031-9007. DOI: 10.1103/PhysRevLett.111.187201. URL: https://link.aps.org/doi/10.1103/PhysRevLett.111.187201.
- Lach, S., Altenhof, A., Tarafder, K., Schmitt, F., Ali, M. E., **Vogel, M.**, Sauther, J., Oppeneer, P. M., and Ziegler, C. (2012). "Metal-Organic Hybrid Interface States of A Ferromagnet/Organic Semiconductor Hybrid Junction as Basis For Engineering Spin Injection in Organic Spintronics". In: *Advanced Functional Materials* 22.5, pp. 989–997. ISSN: 1616301X. DOI: 10.1002/adfm.201102297. URL: http://doi.wiley.com/10.1002/adfm.201102297.
- **Vogel, M.**, Schmitt, F., Sauther, J., Baumann, B., Altenhof, A., Lach, S., and Ziegler, Ch. (2011). "Photoionization cross-section weighted DFT simulations as promising tool for the investigation of the electronic structure of open shell metal-phthalocyanines." In: *Analytical and bioanalytical chemistry*. ISSN: 1618-2650. DOI: 10.1007/s00216-011-4785-x. URL: http://pubget.com/paper/21340688.

Conference Proceedings

- Schillinger, J., Mewes, T., Mewes, C.K.A., **Vogel, M.**, and Back, C.H. (2017). "Micromagnetic Study of Vortex Core Motion driven by Thermal Spin Transfer Torque". In: *APS March meeting*.

- **Vogel, M.**, Stigloher, J., Decker, M., and Back, C.H. (2017). “Talk: Snell’s law for spin waves in a temperature gradient”. In: *DPG Fühjahrstagung*.
- **Vogel**, **M.**, Wild, J., Mewes, T., Mewes, C.K., Zeck, J., and Back, C.H. (2017). “Vortex Core Motion Driven by Magnon Spin Seebeck Effect”. In: *MAGNETISM AND MAGNETIC MATERIALS*.
- **Vogel**, **M.**, Zimmermann, B., Mewes, T., Mewes, C.K., Bauer, G., and Back, C.H. (2017). “Manipulation of the spin wave spectrum in a magnetic bilayer by an applied temperature gradient”. In: *MAGNETISM AND MAGNETIC MATERIALS*.
- Förster, J., Dieterle, G., Noske, M., Gangwar, A., **Vogel, M.**, Stoll, H., Weigand, M., Bykowa, I., Bechtel, M., Back, C.H., and Schütz, G. (2016). “Talk: Imaging of Higher Order Gyromodes in Vortex Structures”. In: *DPG Fühjahrstagung*.
- **Vogel, M.**, Stigloher, J., Decker, M., Zimmermann, M., Müller, M., and Back, C.H. (2016). “Talk: Snell’s law for spin waves in a temperature gradient”. In: *ICMM*.
- **Vogel, M.**, Wild, J., Zimmermann, B., Müller, M., Mewes, C., Mewes, T., Zweck, J., and Back, C.H. (2016). “Talk **(invited)**: Thermally Tunable Coupled Magnetic Vortex Oscillators”. In: *ICMM*.
- **Vogel, M.**, Zimmermann, B., Mewes, C., Back, C.H., and Mewes, T. (2016). “Poster: Implementation of a Spin-Seebeck Diode”. In: *ICMM*.
- **Vogel**, **M.**, Stigloher, J., Decker, M., Zimmermann, M., Müller, M., and Back, C.H. (2016). “Spin Waves in Temperature Gradients”. In: *603. WE-Heraeus-Seminar: Magnonics – Spin Waves Connecting Charges, Spins and Photons*.
- Wild, J., **Vogel, M.**, Mueller, M., Back, C.H., and Zweck, J (2016). “Talk: Study of Magnetic Vortex Oscillations in Permalloy Disks by Lorentz TEM and Differential Phase Contrast Microscopy”. In: *DPG Fühjahrstagung*.
- Wild, J., **Vogel, M.**, Schwarzhuber, F., Back, C.H., and Zweck, J. (2016). “Talk: Transport of Intensity Equation (TIE) without ltering and TIE videos”. In: *European Microscopy Congress*.
- **Vogel, M.**, Chauleau, J-Y., Mewes, C., Mewes, T., and Back, C.H. (2015). “Talk: Vortex Core Motion driven by Thermal Spin Transfer Torque”. In: *DPG Fühjahrstagung*.
- Srichandan, S., Schmid, M., **Vogel, M.**, Strunk, C., and Back, C.H. (2014). “Talk: Magneto-thermopower on FeNi and FeCo thin lms”. In: *DPG Fühjahrstagung*.
- **Vogel, M.**, Chauleau, J-Y., Mewes, C., Back, C.H., and Mewes, T. (2014). “Talk: Vortex Core Motion driven by Thermal Spin Transfer Torque”. In: *MAGNETISM AND MAGNETIC MATERIALS*.
- **Vogel, M.**, Gangwar, A., Brunner, S., Günther, S., Chauleau, J-Y., Mewes, C., Mewes, T., Woltersdorf, G., and Back, C.H. (2014). “Poster: Thermal spin transfer torque in vortex state structures”. In: *DPG Fühjahrstagung*.
- Schmid, M., Srichandan, S., **Vogel, M.**, Strunk, C., Back, C.H., Meier, D., Kuschel, T., Schmalhorst, J. M., and Reiss, G. (2013). “Nernst vs. spin-Seebeck effects in Py thin lms”. In: *DPG Fühjahrstagung*.
- Srichandan, S., Schmid, M., **Vogel, M.**, Strunk, C., and Back, C.H. (2013). “Talk: Transverse magneto-thermoelectric effects in Permalloy lms”. In: *DPG Fühjahrstagung*.
- Lach, S., Altenhof, A., Tarafder, K., Schmitt, F., Ehesan, A., **Vogel, M.**, Sauther, J., Oppeneer, P., and Ziegler, C. (2012). “Talk: Metal-organic hybrid interface states of a ferromagnet/organic semiconductor hybrid junction as basis for engineering spin injection in organic spintronics”. In: *DPG Fühjahrstagung*.
- **Vogel, M.**, Kronseder, M., Freund, F., Woltersdorf, G., and Back, C.H. (2012). “Poster: Theoretical and experimental investigation of ultrathin iron fcc lms”. In: *DPG Fühjahrstagung*.
- Altenhof, A., Schmitt, F., **Vogel, M.**, Lach, S., and Ziegler, C. (2011). “Talk: Spin-resolved photoemission study of the interface of transition

metal phthalocyanines (CuPc, FePc, CoPc) on Co(100)". In: *DPG Fühjahrstagung*.

- **Vogel, M.**, Altenhof, A., Schmitt, F., Sauther, J., Baumann, B., Lach, S., and Ziegler, C. (2011). "Talk: Experimental and theoretical spin-resolved investigations of the electronic structure of open shell metal-phthalocyanines". In: *DPG Fühjahrstagung*.
- **Vogel, M.**, Schmitt, F., Sauther, J., Baumann, B., Altenhof, A., Lach, S., and Ziegler, C. (2011). "Poster: Photoionization cross section weighted DFT simulations as promising tool for the investigation of the electronic structure of open shell metal-phthalocyanines". In: *DPG Fühjahrstagung*.

The following references have been reformatted and corrected after the referee reports of the thesis comittee.

References

[1] C. Mead. Proceedings of the IEEE, **78**:1629–1636 (1990).

[2] M. Sharad, D. Fan, K. Yogendra, and K. Roy. In *2013 Third Berkeley Symposium on Energy Efficient Electronic Systems (E3S)*, pages 1–2. IEEE (2013). ISBN 978-1-4799-3372-3.

[3] J. M. Shalf and R. Leland. Computer, **48**:14–23 (2015).

[4] G. Buzsaki. *Rhythms of the Brain*. Oxford University Press (2006). ISBN 9780195301069.

[5] D. E. Nikonov, G. Csaba, W. Porod, T. Shibata, D. Voils, D. Hammerstrom, I. A. Young, and G. I. Bourianoff. IEEE Journal on Exploratory Solid-State Computational Devices and Circuits, **1**:85–93 (2015).

[6] F. Hoppensteadt and E. Izhikevich. IEEE Transactions on Neural Networks, **11**:734–738 (2000).

[7] T. Shibata, R. Zhang, S. P. Levitan, D. E. Nikonov, and G. I. Bourianoff. In *2012 13th International Workshop on Cellular Nanoscale Networks and their Applications*, pages 1–5. IEEE (2012). ISBN 978-1-4673-0289-0.

[8] S. I. Kiselev, J. C. Sankey, I. N. Krivorotov, N. C. Emley, R. J. Schoelkopf, R. A. Buhrman, and D. C. Ralph. Nature, **425**:380–383 (2003).

[9] W. Rippard, M. Pufall, S. Kaka, S. Russek, and T. Silva. Physical Review Letters, **92**:027201 (2004).

[10] J. Torrejon, M. Riou, F. A. Araujo, S. Tsunegi, G. Khalsa, D. Querlioz, P. Bortolotti, V. Cros, K. Yakushiji, A. Fukushima, H. Kubota, S. Yuasa, M. D. Stiles, and J. Grollier. Nature, **547**:428–431 (2017).

[11] B. Pakkenberg and H. J. G. Gundersen. Journal of Microscopy, **150**:1–20 (1988).

[12] B. A. Ivanov and C. E. Zaspel. Journal of Applied Physics, **95**:7444–7446 (2004).

[13] K. Y. Guslienko, X. F. Han, D. J. Keavney, R. Divan, and S. D. Bader. Phys. Rev. Lett., **96**:67205 (2006).

[14] S. Sugimoto, Y. Fukuma, S. Kasai, T. Kimura, A. Barman, and Y. Otani. Physical Review Letters, **106**:197203 (2011).

[15] M. Noske, A. Gangwar, H. Stoll, M. Kammerer, M. Sproll, G. Dieterle, M. Weigand, M. Fähnle, G. Woltersdorf, C. H. Back, and G. Schütz. Physical Review B, **90**:104415 (2014).

[16] V. Novosad, F. Y. Fradin, P. E. Roy, K. S. Buchanan, K. Y. Guslienko, and S. D. Bader. Physical Review B, **72**:024455 (2005).

[17] S.-B. Choe. Science, **304**:420–422 (2004).

[18] A. Crespi, D. Lachat, A. Pasquier, and A. J. Ijspeert. Autonomous Robots, **25**:3–13 (2008).

[19] A. J. Ijspeert. Neural Networks, **21**:642–653 (2008).

[20] M. Sharad, D. Fan, K. Yogendra, and K. Roy. 2013 3rd Berkeley Symposium on Energy Efficient Electronic Systems, E3S 2013 - Proceedings (2013).

[21] H. G. Bauer, M. Sproll, C. H. Back, and G. Woltersdorf. Physical Review Letters, **112**:077201 (2014).

[22] D. Hinzke and U. Nowak. Physical Review Letters, **107**:027205 (2011).

[23] L. Kong and J. Zang. Physical Review Letters, **111**:067203 (2013).

[24] A. A. Thiele. Journal of Applied Physics, **45**:377–393 (1974).

[25] N. Manton and P. Sutcliffe. *TOPOLOGICAL SOLITONS*. Cambridge University Press, New York, NY, USA, 1st edition (2004). ISBN 9780511617034.

[26] V. Afanasiev. Physics of the Gaseous and Stellar Disks of the Galaxy, ASP Conference Series, **66**:153 (1994).

[27] M. Yan, H. Wang, and C. Campbell. Journal of Magnetism and Magnetic Materials, **320**:1937–1944 (2008).

[28] D. Suess, A. Bachleitner-Hofmann, A. Satz, H. Weitensfelder, C. Vogler, F. Bruckner, C. Abert, K. Prügl, J. Zimmer, C. Huber, S. Luber, W. Raberg, T. Schrefl, and H. Brückl. arXiv, page 1712.07061 (2017).

[29] T. Shinjo, T. Okuno, R. Hassdorf, K. Shigeto, and T. Ono. Science (New York, N.Y.), **289**:930–2 (2000).

[30] B. Van Waeyenberge, A. Puzic, H. Stoll, K. W. Chou, T. Tyliszczak, R. Hertel, M. Fähnle, H. Brückl, K. Rott, G. Reiss, I. Neudecker, D. Weiss, C. H. Back, and G. Schütz. Nature, **444**:461–464 (2006).

[31] J. Shibata, Y. Nakatani, G. Tatara, H. Kohno, and Y. Otani. Physical Review B, **73**:020403 (2006).

[32] R. Antos, Y. Otani, and J. Shibata. Journal of the Physical Society of Japan, **77**:031004 (2008).

[33] D.-S. Han, A. Vogel, H. Jung, K.-S. Lee, M. Weigand, H. Stoll, G. Schütz, P. Fischer, G. Meier, and S.-K. Kim. Scientific Reports, **3**:2262 (2013).

[34] M. Asmat-Uceda, X. Cheng, X. Wang, D. J. Clarke, O. Tchernyshyov, and K. S. Buchanan. Journal of Applied Physics, **117**:123916–142506 (2015).

[35] H. Jung, Y.-S. Choi, K.-S. Lee, D.-S. Han, Y.-S. Yu, M.-Y. Im, P. Fischer, and S.-K. Kim. ACS Nano, **6**:3712–3717 (2012).

[36] D. Kumar, S. Barman, and A. Barman. Scientific Reports, **4**:4108 (2015).

[37] T. Okuno, K. Shigeto, T. Ono, K. Mibu, and T. Shinjo. Journal of Magnetism and Magnetic Materials, **240**:1–6 (2002).

[38] Y. Huai. AAPPS Bulletin, Spin-Transfer Torque MRAM (STT-MRAM): Challenges and Prospects, **18** (2008).

[39] L. Berger. Phys. Rev. B, **54**:9353–9358 (1996).

[40] S. Zhang and Z. Li. Physical Review Letters, **93** (2004).

[41] S. D. Brechet and J.-P. Ansermet. physica status solidi (RRL) – Rapid Research Letters, **5**:423–425 (2011).

[42] A. Slachter, F. L. Bakker, J.-P. Adam, and B. J. VanWees. Nature Physics, **6**:879–882 (2010).

[43] L. Gravier, S. Serrano-Guisan, F. Reuse, and J.-P. Ansermet. Phys. Rev. B, **73**:24419 (2006).

[44] T. Valet and A. Fert. Phys. Rev. B, **48**:7099–7113 (1993).

[45] A. A. Kovalev and Y. Tserkovnyak. Phys. Rev. B, **80**:100408 (2009).

[46] K. M. Hals, A. Brataas, and G. E. Bauer. Solid State Communications, **150**:461–465 (2010).

[47] M. Najafi, B. Krueger, S. Bohlens, M. Franchin, H. Fangohr, A. Vanhaverbeke, R. Allenspach, M. Bolte, U. Merkt, D. Pfannkuche, D. P. F. Mooeller, and G. Meier. Journal of Applied Physics, **105**:113914 (2009).

[48] A. Hubert and R. Schaefer. *Magnetic Domains: The Analysis of Magnetic Microstructures*. Springer-Verlag, Berlin, Heidelberg (1998). ISBN 978-3-540-64108-7.

[49] C. Mewes and T. Mewes. http://magneticslab.ua.edu/micromagnetics-code.html.

[50] F. K. Dejene, J. Flipse, and B. J. van Wees. Phys. Rev. B, **86**:24436 (2012).

[51] B. Krueger, A. Drews, M. Bolte, U. Merkt, D. Pfannkuche, and G. Meier. Phys. Rev. B, **76**:224426 (2007).

[52] A. Thiaville, Y. Nakatani, J. Miltat, and Y. Suzuki. EPL (Europhysics Letters), **69**:990 (2005).

[53] J. Shibata and Y. Otani. Phys. Rev. B, **70**:12404 (2004).

[54] W. Jiang, P. Upadhyaya, Y. Fan, J. Zhao, M. Wang, L.-T. Chang, M. Lang, K. L. Wong, M. Lewis, Y.-T. Lin, J. Tang, S. Cherepov, X. Zhou, Y. Tserkovnyak, R. N. Schwartz, and K. L. Wang. Phys. Rev. Lett., **110**:177202 (2013).

[55] S. Seki, X. Z. Yu, S. Ishiwata, and Y. Tokura. Science, **336**:198–201 (2012).

[56] X. Yu, M. Mostovoy, Y. Tokunaga, W. Zhang, K. Kimoto, Y. Matsui, Y. Kaneko, N. Nagaosa, and Y. Tokura. Proceedings of the National Academy of Sciences, **109**:8856–8860 (2012).

[57] S. Bhagat, H. Lessoff, C. Vittoria, and C. Guenzer. physica status solidi (a), **20**:731–738 (1973).

[58] X. S. Wang and X. R. Wang. Phys. Rev. B, **90**:14414 (2014).

[59] G. Tatara. Phys. Rev. B, **92**:64405 (2015).

[60] M. Mochizuki, X. Y. Yu, S. Seki, N. Kanazawa, W. Koshibae, J. Zang, M. Mostovoy, Y. Tokura, and N. Nagaosa. Nature Materials, **13**:241–246 (2013).

[61] A. A. Kovalev and Y. Tserkovnyak. Solid State Communications, **150**:500–504 (2010).

[62] J. M. Luttinger. Phys. Rev., **135**:A1505—-A1514 (1964).

[63] P. Yan, Y. Cao, and J. Sinova. Phys. Rev. B, **92**:100408 (2015).

[64] H. Oji and P. Streda. Phys. Rev. B, **31**:7291–7295 (1985).

[65] H. Kohno, Y. Hiraoka, M. Hatami, and G. E. W. Bauer. Phys. Rev. B, **94**:104417 (2016).

[66] R. Matsumoto, R. Shindou, and S. Murakami. Phys. Rev. B, **89**:54420 (2014).

[67] P. N. Butcher. Journal of Physics: Condensed Matter, **2**:4869 (1990).

[68] N. W. Ashcroft and N. D. Mermin. *Solid state physics*. Holt, Rinehart and Winston (1976). ISBN 0030839939.

[69] K. D. Belashchenko, O. Tchernyshyov, A. A. Kovalev, and O. A. Tretiakov. Applied Physics Letters, **108**:132403 (2016).

[70] T. S. Machado, T. G. Rappoport, and L. C. Sampaio. Applied Physics Letters, **100**:112404 (2012).

[71] G. M. Wysin and W. Figueiredo. Phys. Rev. B, **86**:104421 (2012).

[72] W. F. J. Brown. IEEE Transactions on magnetics, **15**:1196–1208 (1979).

[73] K. Kobayashi, N. Inaba, N. Fujita, Y. Sudo, T. Tanaka, M. Ohtake, M. Futamoto, and F. Kirino. IEEE Transactions on Magnetics, **45**:2541–2544 (2009).

[74] K.-S. Lee, H. Jung, D.-S. Han, and S.-K. Kim. Journal of Applied Physics, **110**:113903 (2011).

[75] A. Vogel, A. Drews, T. Kamionka, M. Bolte, and G. Meier. Phys. Rev. Lett., **105**:37201 (2010).

[76] A. Barman, S. Barman, T. Kimura, Y. Fukuma, and Y. Otani. Journal of Physics D: Applied Physics, **43**:422001 (2010).

[77] A. A. Awad, G. R. Aranda, D. Dieleman, K. Y. Guslienko, G. N. Kakazei, B. A. Ivanov, and F. G. Aliev. Applied Physics Letters, **97**:132501 (2010).

[78] Hopster H. and H. Oepen. *Magnetic Microscopy of Nanostructures*. Springer-Verlag, Berlin/Heidelberg, 1st edition (2006). ISBN 3-540-40186-5.

[79] R. Grechishkin, S. Chigirinsky, M. Gusev, O. Cugat, and N. M. Dempsey. In *Magnetic Nanostructures in Modern Technology*, pages 195–224. Springer Netherlands, Dordrecht (2008). ISBN 1402063377.

[80] M. R. Freeman and B. C. Choi. Science, **3**:1484–1488 (2001).

[81] H. Kronmüller and S. S. P. Parkin. *Handbook of magnetism and advanced magnetic materials*. John Wiley & Sons (2007). ISBN 0470022175.

[82] L. v. Hámos and P. A. Thiessen. Zeitschrift für Physik, **71**:442–444 (1931).

[83] F. Bitter. Physical Review, **38**:1903–1905 (1931).

[84] F. Bitter. Physical Review, **41**:507–515 (1932).

[85] P. Rice and J. Moreland. Review of Scientific Instruments, **62**:844–845 (1991).

[86] U. Hartmann and H. Mende. Journal of Magnetism and Magnetic Materials, **41**:244–246 (1984).

[87] G. A. Jones and I. B. Puchalska. Philosophical Magazine Part B, **40**:89–96 (1979).

[88] G. A. Jones and I. B. Puchalska. Physica Status Solidi (a), **51**:549–558 (1979).

[89] I. B. Puchalska, G. A. Jones, and H. Jouve. Journal of Physics D: Applied Physics, **11**:L175–L178 (1978).

[90] L. R. Rayleigh. Philosophical Magazine Series 5, **8**:261–274 (1879).

[91] G. B. Airy and G. B. Transactions of the Cambridge Philosophical Society, Vol. 5, p.283, **5**:283 (1835).

[92] J. Stigloher, M. Decker, H. S. Koerner, K. Tanabe, T. Moriyama, T. Taniguchi, H. Hata, M. Madami, G. Gubbiotti, K. Kobayashi, T. Ono, and C. H. Back. Physical Review Letters, **117**:037204 (2016).

[93] J. Kerr. Philosophical Magazine Series 5, **3**:321–343 (1877).

[94] E. Ruska. Zeitschrift fuer Physik, **87**:580–602 (1934).

[95] H. Boersch, H. Raith, and D. Wohlleben. Zeitschrift fuer Physik, **159**:388–396 (1960).

[96] H. Boersch and H. Raith. Die Naturwissenschaften, **46**:574–574 (1959).

[97] M. E. Hale, H. W. Fuller, and H. Rubinstein. Journal of Applied Physics, **30**:789–791 (1959).

[98] J. Zweck and T. Uhlig. In *Handbook of Magnetism and Advanced Magnetic Materials*. John Wiley & Sons, Ltd (2007). ISBN 9780470022184.

[99] J. N. Chapman. Journal of Physics D: Applied Physics, **17**:623–647 (1984).

[100] D. Eyidi, C. Hébert, and P. Schattschneider. Ultramicroscopy, **106**:1144–1149 (2006).

[101] A. Petford-Long and J. Chapman. In *Magnetic Microscopy of Nanostructures*, pages 67–86. Springer, Berlin, Heidelberg, Berlin, Heidelberg (2005).

[102] J. Chapman, I. McFadyen, and S. McVitie. IEEE Transactions on Magnetics, **26**:1506–1511 (1990).

[103] J. P. Guigay and R. H. Wade. Physica Status Solidi (b), **29**:799–805 (1968).

[104] O. Scherzer. Zeitschrift fuer Physik, **101**:593–603 (1936).

[105] K. Tillmann, J. Barthel, and L. Houben. Journal of large-scale research facilities JLSRF, **1**:A34 (2015).

[106] J. M. Cowley. *Diffraction physics*. Elsevier Science B.V (1995). ISBN 9780080530390.

[107] V. V. Volkov and Y. Zhu. Ultramicroscopy, **98**:271–281 (2004).

[108] J. Wild, M. Vogel, M. Mueller, C. Back, and J. Zweck. In *DPG Fühjahrstagung (Talk)*, page MA 46.4 (2016).

[109] J. Wild, M. Vogel, F. Schwarzhuber, C. Back, and J. Zweck. In *European Microscopy Congress*, pages MS02–647 (2016).

[110] J. Wild. *Lorentz- Transmissionselektronenmikroskopie und Differentielle Phasenkontrastmikroskopie an magnetischen Skyrmionen*. Ph.D. thesis, Regensburg (2017).

[111] L. Waller, L. Tian, and G. Barbastathis. Optics Express, **18**:12552 (2010).

[112] N. R. da Silva, M. Möller, A. Feist, H. Ulrichs, C. Ropers, and S. Schäfer. arXiv:1710.03307 (2017).

[113] U. Wiesemann. *The transmission X-ray microscope at BESSY II*. Ph.D. thesis, Göttingen (2003).

[114] G. Schütz, E. Goering, H. Stoll, G. Schütz, E. Goering, and H. Stoll. In *Handbook of Magnetism and Advanced Magnetic Materials*. John Wiley & Sons, Ltd, Chichester, UK (2007). ISBN 9780470022184.

[115] H. Wende and C. Antoniak. In *Magnetism and Synchrotron Radiation*, pages 145–167. Springer, Berlin, Heidelberg (2010). ISBN 0075-8450.

[116] C. Cohen-Tannoudji, B. Diu, and F. Laloë. *Quantum mechanics*. Wiley (2005). ISBN 0471569526.

[117] W. Weber. *Magnetism and Synchrotron Radiation*, volume 133 of *Springer Proceedings in Physics*. Springer Berlin Heidelberg, Berlin, Heidelberg (2010). ISBN 978-3-642-04497-7.

[118] C. T. Chen, F. Sette, Y. Ma, and S. Modesti. Physical Review B, **42**:7262–7265 (1990).

[119] P. Yu, X. F. Jin, J. Kudrnovský, D. S. Wang, and P. Bruno. Physical Review B, **77**:054431 (2008).

[120] Maximilian Schmid. *Magneto-thermoelectric effects in NiFe thin films*. Ph.D. thesis, University Regensburg (2015).

[121] J. Holanda, O. Alves Santos, R. O. Cunha, J. B. S. Mendes, R. L. Rodríguez-Suárez, A. Azevedo, and S. M. Rezende. Physical Review B, **95**:214421 (2017).

[122] M. Schmid, S. Srichandan, D. Meier, T. Kuschel, J.-M. Schmalhorst, M. Vogel, G. Reiss, C. Strunk, and C. H. Back. Physical Review Letters, **111**:187201 (2013).

[123] R. Hertel. Zeitschrift für Metallkunde, **93**:957–962. (2002).

[124] S. S. P. Parkin, M. Hayashi, and L. Thomas. Science, **320**:190–194 (2008).

[125] M. Najafi, B. Krüger, S. Bohlens, M. Franchin, H. Fangohr, A. Vanhaverbeke, R. Allenspach, M. Bolte, U. Merkt, D. Pfannkuche, D. P. F. Möller, and G. Meier. Journal of Applied Physics, **105**:113914 (2009).

[126] P. J. Brown, K. U. Neumann, P. J. Webster, and K. R. A. Ziebeck. Journal of Physics: Condensed Matter, **12**:1827–1835 (2000).

[127] M. P. Raphael, B. Ravel, M. A. Willard, S. F. Cheng, B. N. Das, R. M. Stroud, K. M. Bussmann, J. H. Claassen, and V. G. Harris. Applied Physics Letters, **79**:4396–4398 (2001).

[128] S. Srichandan. *Electrical and thermal transport coefficients of CoFe thin films deposited on a microcalorimeter*. Ph.D. thesis, University of Regensburg (2017).

[129] H. Ftouni, D. Tainoff, J. Richard, K. Lulla, J. Guidi, E. Collin, and O. Bourgeois. Review of Scientific Instruments, **84**:094902 (2013).

[130] V. R. Manfrinato, L. Zhang, D. Su, H. Duan, R. G. Hobbs, E. A. Stach, and K. K. Berggren. Nano Letters, **13**:1555–1558 (2013).

[131] C. Vieu, F. Carcenac, A. Pépin, Y. Chen, M. Mejias, A. Lebib, L. Manin-Ferlazzo, L. Couraud, and H. Launois. Applied Surface Science, **164**:111–117 (2000).

[132] M. Stepanova and S. Dew. *Nanofabrication: Techniques and principles*, volume 9783709104 (2014). ISBN 9783709104248.

[133] R. J. Hawryluk. Journal of Vacuum Science and Technology, **19**:1–17 (1981).

[134] M. Stepanova, T. Fito, Z. Szabó, K. Alti, A. P. Adeyenuwo, K. Koshelev, M. Aktary, and S. K. Dew. Journal of Vacuum Science & Technology B, Nanotechnology and Microelectronics: Materials, Processing, Measurement, and Phenomena, **28**:C6C48–C6C57 (2010).

[135] M. Mohammad, T. Fito, J. Chen, S. Buswell, M. Aktary, M. Stepanova, and S. Dew. Microelectronic Engineering, **87**:1104–1107 (2010).

[136] H. Elsner, H.-G. Meyer, A. Voigt, and G. Grützner. Microelectronic Engineering, **46**:389–392 (1999).

[137] B. Zimmermann. *FMR of dynamically coupled magnetic multilayer influenced by a thermal gradient*. Ph.D. thesis, University Regensburg (2017).

[138] A. Gangwar. *Electrical Determination of Vortex State in Submicron Magnetic Elements*. Ph.D. thesis, University of Regensburg (2015).

[139] B. Zimmermann. *Bestimmung von Temperaturgradienten in magnetischen Nanostrukturen*. Ph.D. thesis, University of Regensburg (2014).

[140] L. Bretzner and T. Lindeberg. Computer Vision and Image Understanding, **71**:385–392 (1998).

[141] A. A. Sharma, K. Neelathalli, D. Marculescu, and E. Nurvitadhi. In *2013 IEEE International Conference on Acoustics, Speech and Signal Processing*, pages 2693–2696. IEEE (2013). ISBN 978-1-4799-0356-6.

[142] G. Robert Kozma, Robinson E. Pino. *Advances in Neuromorphic Memristor Science and Applications vol. 4.* Springer-Verlag, New York, NY, USA (2012).

[143] E. Marder and D. Bucher. Current Biology, **11**:R986–R996 (2001).

[144] H.-T. Kim, B.-J. Kim, S. Choi, B.-G. Chae, Y. W. Lee, T. Driscoll, M. M. Qazilbash, and D. N. Basov. Journal of Applied Physics, **107**:023702 (2010).

[145] N. Shukla, A. Parihar, E. Freeman, H. Paik, G. Stone, V. Narayanan, H. Wen, Z. Cai, V. Gopalan, R. Engel-Herbert, D. G. Schlom, A. Raychowdhury, and S. Datta. Scientific Reports, **4**:4964 (2015).

[146] A. A. Sharma, J. A. Bain, and J. A. Weldon. IEEE Journal on Exploratory Solid-State Computational Devices and Circuits, **1**:58–66 (2015).

[147] K.-S. Lee, H. Jung, D.-S. Han, and S.-K. Kim. Journal of Applied Physics, **110**:113903 (2011).

[148] A. V. Chumak, A. A. Serga, and B. Hillebrands. Journal of Physics D: Applied Physics, **50**:244001 (2017).

[149] H. Kubota, A. Fukushima, Y. Ootani, S. Yuasa, K. Ando, H. Maehara, K. Tsunekawa, D. D. Djayaprawira, N. Watanabe, and Y. Suzuki. Applied Physics Letters, **89**:032505 (2006).

[150] Z. Diao, D. Apalkov, M. Pakala, Y. Ding, A. Panchula, and Y. Huai. Applied Physics Letters, **87**:232502 (2005).

[151] C. Y. Ho, M. W. Ackerman, K. Y. Wu, T. N. Havill, R. H. Bogaard, R. A. Matula, S. G. Oh, and H. M. James. Journal of Physical and Chemical Reference Data, **12**:183–322 (1983).